

# **Dust-related ice formation in the troposphere**

## **A statistical analysis based on 11 years of lidar observations of aerosols and clouds over Leipzig**

Der Fakultät für Physik und Geowissenschaften  
der Universität Leipzig  
eingereichte

D I S S E R T A T I O N

zur Erlangung des akademischen Grades

DOCTOR RERUM NATURALIUM  
Dr. rer. nat.

vorgelegt

von Diplom-Meteorologe Patric Seifert  
geboren am 20. Januar 1981 in Riesa

Leipzig, 30. September 2010



## **Bibliographische Beschreibung:**

Seifert, Patric

Dust-related ice formation in the troposphere: A statistical analysis based on 11 years of lidar observations of aerosols and clouds over Leipzig

Universität Leipzig, Dissertation

131 S., 191 Lit., 57 Abb., 11 Tab.

### Referat:

Im Rahmen der vorliegenden Arbeit wurde der Zusammenhang zwischen heterogener Eisbildung und Temperatur auf Basis eines 11-Jahres Lidardatensatzes untersucht, wobei besonders der potenzielle Einfluss von Wüstenstaubaerosol auf die heterogene Gefriertemperatur von unterkühlten Wasserwolken überprüft wurde. Der zugrundeliegende Lidardatensatz entstand im Rahmen von zwischen 1997 und 2008 am Leibniz-Institut für Troposphärenforschung (IfT) in Leipzig durchgeführten Lidarmessungen. Mehr als 2300 zeitlich und räumlich definierte Wolkenschichten wurden anhand des gemessenen linearen Depolarisationsverhältnisses als Flüssigwasserwolken oder als eisbeinhaltende Wolken klassifiziert. Dazu war es nötig, den störenden Einfluss von spiegelnden Reflektionen horizontal ausgerichteter Eiskristalle auf das gemessene Depolarisationsverhältnis zu charakterisieren. Die für die Auswertung benötigten Wolktoberkantentemperaturen wurden aus Modelldaten oder, falls zeitnah verfügbar, aus Radiosondenprofilen ermittelt.

Die statistische Auswertung des Wolkendatensatzes ergab, dass der Anteil an eisbeinhaltenden Wolken mit abnehmender Temperatur stark zunimmt. Wurde in Wolken mit Oberkantentemperaturen zwischen 0 und  $-5\text{ °C}$  in nur 1% aller Fälle Eis detektiert, enthielten zwischen  $-10$  und  $-15\text{ °C}$  bereits 40% der in dem Temperaturbereich beobachteten Wolken Eis. Bei Wolktoberkantentemperaturen unterhalb von  $-25\text{ °C}$  wurde in nahezu 100% aller Fälle Eis in den Wolken beobachtet. Ein ähnlicher Zusammenhang zwischen Temperatur und dem Anteil an eisbeinhaltenden Wolken wurde bereits in zahlreichen auf Flugzeugmessungen basierenden Studien gefunden.

In einem weiteren Schritt wurde der Wolkendatensatz mittels drei verschiedener Ansätze in einen staubbelasteten sowie einen staubfreien Teil getrennt. Dies geschah Anhand einer Trajektorien-Clusteranalyse sowie der Trennung bezüglich der von einem Mineralstaubvorhersagemodell berechneten Mineralstaubbelastung in Wolkenhöhe beziehungsweise in der gesamten Luftsäule über Leipzig. Die Trennung ergab, dass staubbelastete Wolken im Temperaturbereich zwischen  $-5$  und  $-25\text{ °C}$  10–30% mehr Eis beinhalten als staubfreie Wolken. Die Ergebnisse dieser Untersuchung legen deshalb nahe, dass Mineralstaub Eisbildung in unterkühlten Wolken maßgeblich fördert.

Der Vergleich des Leipziger Wolkendatensatzes mit einem auf den Kapverden gesammelten Datensatz tropischer Wolken zeigte, dass trotz vergleichbarem Einfluss von Mineralstaubaerosol Eisbildung in den Tropen erst bei um 10 K tieferen Temperaturen einsetzt. Als mögliche Einflussfaktoren wurden Unterschiede in der atmosphärischen Dynamik und die Wirkung effektiverer Eiskeime über Mitteleuropa diskutiert.



---

# Table of Contents

<b>1</b>	<b>Introduction</b>	<b>1</b>
<b>2</b>	<b>Ice formation</b>	<b>7</b>
2.1	Homogeneous nucleation . . . . .	7
2.2	Heterogeneous nucleation . . . . .	9
2.2.1	Heterogeneous nucleation processes . . . . .	10
2.2.2	Studies of heterogeneous nucleation . . . . .	11
2.3	Dynamical processes and ice multiplication . . . . .	15
<b>3</b>	<b>Motivating questions for the present study</b>	<b>19</b>
<b>4</b>	<b>IfT Earlinet lidar MARTHA</b>	<b>23</b>
4.1	IfT lidar system MARTHA . . . . .	23
4.2	Lidar equation . . . . .	25
4.3	Particle backscatter coefficient . . . . .	27
4.3.1	Klett–Fernald method . . . . .	27
4.3.2	Raman method . . . . .	28
4.4	Particle extinction coefficient . . . . .	28
4.5	Depolarization ratio . . . . .	29
4.5.1	Depolarization ratio for idealized systems . . . . .	30
4.5.2	Depolarization ratio for non-idealized systems . . . . .	30
<b>5</b>	<b>Cloud detection with MARTHA</b>	<b>33</b>
5.1	Cloud geometrical properties . . . . .	33
5.2	Meteorological data . . . . .	35
5.3	Aerosol information . . . . .	39
5.4	Cloud phase determination . . . . .	42
5.5	Multiple scattering . . . . .	44
5.6	Specular reflection . . . . .	48
5.6.1	Instrumentation . . . . .	50
5.6.2	WiLi and MARTHA observations . . . . .	52
5.6.3	Polly <sup>XT</sup> and MARTHA observations . . . . .	57

---

5.7	Liquid/Ice-containing layer discrimination scheme for MARTHA . . . . .	63
<b>6</b>	<b>Observations</b>	<b>67</b>
6.1	20 June 2007: Cloud development in Saharan dust . . . . .	67
6.2	3 November 2003 and 24 November 2006: Cloud development at aerosol back-ground conditions . . . . .	71
6.3	26 May 2008 and 26 December 2008: Indications for deposition nucleation . .	74
<b>7</b>	<b>The MARTHA 1997 – 2008 cloud data set</b>	<b>79</b>
7.1	Statistical basis . . . . .	79
7.2	Geometrical cloud properties . . . . .	83
7.3	Relationship between heterogeneous ice formation and temperature . . . . .	88
7.4	Impact of Saharan dust on heterogeneous ice nucleation . . . . .	91
7.4.1	Trajectory cluster analysis . . . . .	92
7.4.2	Dust-model-based investigations . . . . .	93
7.5	Discussion . . . . .	100
<b>8</b>	<b>Summary, conclusions, and outlook</b>	<b>107</b>
8.1	Summary and conclusions . . . . .	107
8.2	Outlook . . . . .	111
	<b>Bibliography</b>	<b>113</b>
	<b>List of abbreviations</b>	<b>131</b>

---

# Chapter 1

## Introduction

Aerosols, clouds, and their interaction play a key role in balancing the global climate [Heintzenberg and Charlson, 2009]. This relationship is most insistently shown in the estimation of the response of the climate on aerosol effects as presented in the last two reports of the Intergovernmental Panel on Climate Change (IPCC) [IPCC, 2001, 2007]. In addition, the large error bars that are attached to the estimated values of cloud and aerosol radiative forcing emphasize the poor scientific knowledge of the underlying processes.

It is well known that the radiation budget of the atmosphere is directly affected by aerosols because they scatter and absorb incoming solar and outgoing terrestrial radiation. Whereas the direct radiative effect of aerosol particles can be assessed rather straight forward by direct measurements [Holben *et al.*, 2001], observations and quantifications of indirect effects on the atmospheric environment are difficult to achieve. Aerosol indirect effects are manifold [Heintzenberg and Charlson, 2009]. They can modify the state of the atmosphere by fertilizing the biosphere [Jickells *et al.*, 2005] or by darkening the cryosphere which leads to enhanced melting rates and decreased ground albedo [Flanner *et al.*, 2007; Ramanathan and Carmichael, 2008]. Most discussed and, according to the IPCC reports, most relevant indirect aerosol effects are related to modifications of cloud radiative and microphysical properties [Lohmann and Feichter, 2005; Lohmann and Hoose, 2009]. These properties and consequently cloud life time are affected by aerosols that can change the vertical stability of the atmosphere due to radiative effects [Koren *et al.*, 2004; Lohmann and Feichter, 2005; Levin and Brenguier, 2008]. In addition, aerosol particles act as seeds that are needed to initiate the formation of cloud droplets and ice crystals.

In the case of liquid water clouds the availability of a high number of nuclei favors the formation of more but smaller droplets compared to an environment with less nuclei available. This change in the microphysical cloud properties results in reduced precipitation rates, in an increased life time of the cloud [Albrecht, 1989], and in the so-called Twomey effect [Twomey, 2007] which describes the increase in cloud albedo with decreasing cloud droplet size. The Twomey effect can be clearly observed with satellite-based remote sensing when anthropogenic aerosol emissions alongside ship tracks produce stratus clouds that are much brighter than clouds in surrounding less-polluted air masses [Radke *et al.*, 1989].

---

Going a step further, the influence of aerosols on ice crystal formation complicates the situation dramatically. A multitude of pathways can lead to ice formation. These processes can again be influenced by indirect aerosol effects similar to the ones affecting liquid water droplet formation [Lohmann and Hoose, 2009; Muhlbauer and Lohmann, 2009]. The present state of knowledge concerning ice formation processes in general and of the nature and abundance of aerosol particles acting as ice nuclei (IN) in ambient clouds is extremely poor [Cantrell and Heymsfield, 2005; Lohmann and Feichter, 2005]. Strong indication for an influence of aerosol particles on cloud freezing is given by numerous weather modification experiments which had their period of prosperity around the middle of the 20th century [Howell, 1977]. The injection of anthropogenic aerosols like silver iodide into convective clouds was found to change the cloud microphysical properties significantly. There are also some observations suggesting an influence of ambient aerosols on ice formation processes [Sassen, 2002; Sassen et al., 2003; Ansmann et al., 2005; Sassen, 2005a] but a clear observational link between meteorological conditions and aerosol properties, IN concentration, ice crystal concentration, and growth of crystals to sizes suitable for precipitation has not been established yet.

Tropospheric aerosol concentrations can vary over several orders of magnitude from background conditions to strongly polluted scenarios that are connected to industrial activities, regions with biomass burning, and mineral dust outbreaks. The question of how suitable different atmospheric aerosol types are regarding their role to serve as IN has been subject of various laboratory studies. It is known that the temperature at which ice nucleation is triggered in a supercooled droplet can range from  $-38$  to  $0$  °C. Under well-defined thermodynamic conditions in cloud chambers the exact level of freezing has been found to be determined by the chemical and morphological properties of the insoluble IN, the properties of potential coatings of the IN [Wurzler et al., 2000; Möhler et al., 2008; Cziczo et al., 2009a; Niedermeier et al., 2010], and the way in which the IN is brought into contact with the supercooled droplet whose properties need to be known as well [Pruppacher, 1995, chap. 9]. Nowadays, it is widely accepted that ice nucleation at high temperatures is preferably initiated by a collision of a dry IN with a supercooled droplet. Much lower temperatures are needed to trigger the formation of a crystal through deposition of water vapor on an IN. Also, aerosols can meanwhile be separated into more effective IN species like mineral dust [Field et al., 2006; Connolly et al., 2009], metals [Richardson et al., 2007; Kamphus et al., 2009], and biological particles [Diehl et al., 2006; Pratt et al., 2009] and into less effective IN species like sulfates [Richardson et al., 2007; Kamphus et al., 2009].

The observation of ice nucleation processes in clouds in the ambient environment is generally difficult. From *in situ* aircraft studies valuable information about microphysical properties of cloud particles can be obtained [McFarquhar and Heymsfield, 1996; Hogan et al., 2003; Ehrlich et al., 2009]. The snapshots provided by the airborne measurements are however difficult to be brought into context with the overall cloud structure. Even though cloud top temperature is a controlling parameter in ice formation processes [Rauber and Tokay, 1991; Harrington et al., 1999; Lebo et al., 2008], aircraft observations are often related to the temperature at flight level, disregarding that the observed cloud particles may

---

---

have formed at higher, colder altitudes. Airborne *in situ* studies of the cloud evolution are also difficult to perform. Aircraft measure at high ground speeds and influence the cloud evolution itself because of turbulence and mixing produced in the rear of the aircraft which prohibits multiple observations of the same cloud parcels.

An integral picture of the vertical cloud structure, including multiple-layered clouds, can be obtained with active remote sensing instruments as lidar and radar. The contact-free measurement technique allows for the observation of the same cloud system and thus of the cloud evolution over a longer time period. However, active remote sensing only detects the scattering properties of the probed particles. From these information the microphysical properties must then be inferred. The applicability of the different active remote sensing techniques is in addition limited by the number and size of the scattering particles. The short wavelengths used by lidar are suitable for the detection of small particles like aerosols whereas high numbers of large particles as liquid-water drops and ice crystals quickly attenuate the signal. Radar, in turn, is very sensitive to large scattering particles but aerosols are usually not detected because of the long radar wavelength.

The situation therefore further complicates when aerosol layers and embedded cloud layers need to be observed simultaneously, e.g., to study the influence of aerosol particles on the formation and the development of a cloud. In recent studies and field campaigns it is thus aspired to use synergies between different observational systems in order to derive a complementary picture of the complicated nature of the observed scenarios [*Jenson et al.*, 2004; *Wulfmeyer et al.*, 2008; *Zipser et al.*, 2009]. However, field campaigns with combined *in situ* and active-remote-sensing measurements are usually restricted to a short time period which limits the statistical value of the assembled data sets. Still, detailed case studies may be obtained describing single observations of cloud-aerosol interactions.

It is aspired to overcome the lack of observational evidence of the indirect aerosol effect on ice formation in clouds by laboratory measurements and accompanying modeling studies [*Levin et al.*, 2005; *Lohmann and Feichter*, 2005; *Diehl et al.*, 2006; *Fridlind et al.*, 2007]. However, without observational prove – or discard – the laboratory and numerically based knowledge remains speculative and the error bars at the respective positions in the IPCC reports will remain large.

This work uses a novel approach to study the influence of mineral dust on ice formation. For the first time a long-term lidar data set is exploited to study the relation between aerosol properties and the occurrence of ice in free-tropospheric clouds. Such a study can be regarded as a complementary activity to aircraft observations and field campaigns. More than 2000 measurement hours from 11 years of lidar observations are available. The study is concentrated on the investigation of the freezing efficiency of Saharan dust that is currently recognized as the most important IN species [*Richardson et al.*, 2007; *Kamphus et al.*, 2009].

Since the start of lidar measurements in 1997 the work of the optical remote measurements group at the Leibniz Institute for Tropospheric Research (IfT) Leipzig has been dedicated to the assessment of the vertical and temporal distribution of the tropospheric aerosol and its optical and microphysical properties. Various case studies documented the occurrence and

---

the vertical extent of aerosol layers that were advected towards Leipzig over large distances and from different sources. Prominent examples for such studies are the observation of Arctic haze [Müller *et al.*, 2004], Siberian and Canadian forest fire smoke [Müller *et al.*, 2005], and of Saharan dust [Mattis *et al.*, 2002; Ansmann *et al.*, 2003; Müller *et al.*, 2003].

Measurements were coordinated and scheduled regularly within networks, i. e., the German Lidar Network (1997–2000) and the European Aerosol Research Lidar Network (Earlinet, since 2000) which ensured the evolution of a consistent data set whose relevance grew with an increasing number of available measurements. The long-term data set was analyzed according to air masses in order to determine the average vertical distribution and mean optical aerosol properties over Leipzig with respect to their origin [Mattis *et al.*, 2004; Wandinger *et al.*, 2004] or their type [Müller *et al.*, 2007]. The most recent study that used the IfT lidar data set is based on 10 years of regular lidar measurements and documents the vertical distribution, occurrence frequency, and seasonal dependence of aerosol layers in the free troposphere over Leipzig for different source regions [Mattis *et al.*, 2008].

With ongoing lidar observations of the tropospheric aerosol at Leipzig, cloud observations accumulated in the data set. From the observations of mixed-phase clouds that were embedded in layers of Saharan dust, Ansmann *et al.* [2005] compiled an impressive overview of how lidar can be assessed to document and study ice formation under ambient conditions in tropospheric clouds. They documented at which temperatures ice formation started and which role tropospheric waves and high concentrations of Saharan dust can play in the ice formation process.

While case studies are a powerful approach to investigate specific processes like ice formation in clouds in detail, statistics that are based on large data sets allow us to gather information about the climate relevance of these processes. The location of Leipzig in central Europe provides the unique opportunity to study clouds under diverse aerosol conditions. Depending on the synoptic state, air masses are advected towards Leipzig from the northern Atlantic Ocean, from polluted eastern Europe, from highly populated and industrialized western Europe, or from southern Europe and the Saharan desert. By contrasting observations of clouds which are not influenced by mineral dust with cloud measurements performed during Saharan dust outbreaks, the impact of dust on ice formation should become visible. The study of the specific influence of desert dust on ice formation in clouds is the central goal of this work. In this manner all lidar measurements performed at Leipzig between 1997 and 2008 were screened for the occurrence of cloud layers which were then characterized in terms of their thermodynamic state, i.e., cloud phase, and, in part by means of model data, the origin and meteorological properties of the air masses in which the clouds formed. In 2006, 2007, and 2008 numerous additional measurements were performed in the frame of this Ph.D. work when the meteorological conditions were favorable for the formation of mid-tropospheric clouds to increase the statistical basis of the cloud data set.

The work was done in the framework of the project DRIFT — Dust Related Ice Formation In the Troposphere. After the introduction a review of the current understanding of freezing processes is given in Chapter 2. The various pathways that can lead to the transformation

---

of a liquid water drop to an ice crystal are described and the roles that different aerosol types, including mineral dust, play for these processes are discussed. Chapter 3 lists the motivating questions for this work. In Chapter 4, the theoretical background concerning the lidar data analysis is given. Approaches for the determination of the depolarization ratio and the scattering properties of the observed clouds and aerosol layers are explained. Chapter 5 describes the steps that were taken to identify, classify, and categorize the observed cloud layers. One of the central tasks was to develop a robust analysis scheme that allows us to unambiguously identify ice in mid-level and low clouds. In this context the effects of multiple scattering and specular reflection were investigated. The first effect may lead to the misinterpretation of liquid water clouds as ice clouds whereas the latter one can produce false liquid-water-like signatures in ice layers. In Chapter 6, case studies of cloud observations are presented. The measurements are discussed in detail with emphasis put on the determination of the relevant ice formation processes and their interaction with the ambient aerosol properties. The statistical evaluation of the 11-year DRIFT cloud data set is presented in Chapter 7. Results concerning the distribution of ice and water clouds as a function of temperature are discussed with respect to existing similar data sets. The largest part of Chapter 7 deals with the main goal of this thesis which is the understanding of the potential role of dust on ice formation in the troposphere. Chapter 8 summarizes and concludes this study and gives motivations for further investigations based on the presented findings.

---



## Chapter 2

# Ice formation

Since the formulation of the Bergeron–Findeisen process [Findeisen, 1938] it is accepted that the formation of significant amounts of precipitation depends on the availability of ice crystals. The difference in saturation water vapor pressure over a liquid water surface in comparison to the one over an ice surface leads to preferred growth of the crystals. Only in this way the hydrometeors can reach sizes that are large enough to initiate precipitation.

Even though the basics for understanding precipitation formation were set by Findeisen [1938] the formation of ice crystals, which also determines cloud radiative properties, is still poorly understood [Cantrell and Heymsfield, 2005; Yoshida and Asano, 2005; Korolev, 2007; Korolev and Field, 2008].

In principle, tropospheric ice formation can occur in two ways. At temperatures below approximately  $-36$  to  $-40$  °C the phase transfer from liquid to solid can occur homogeneously without the support of a catalytic substance. At temperatures above  $-36$  °C, ice nucleation must be initiated heterogeneously by aerosol particles that act as ice nuclei (IN). Both freezing processes are described below (Sections 2.1 and 2.2). In the third part of this chapter (Section 2.3), the impact of cloud dynamics on heterogeneous nucleation is discussed and ice multiplication processes, which play a role only after an ice crystal was formed either homogeneously or heterogeneously, are introduced.

### 2.1 Homogeneous nucleation

From theoretical considerations it is known that water can exist in the supercooled liquid phase down to temperatures of below  $-40$  °C [Pruppacher, 1995]. The temperature level that is necessary to keep an embryonic crystallized cluster of water molecules in a stable state decreases dramatically with its decreasing size. The formation of these embryonic ice clusters depends on statistical thermodynamic processes. The probability for the formation of small clusters is much higher than for the formation of large clusters. As in the case of liquid water droplets [Mason, 1971] an energy barrier, known as the free energy  $\Delta G$ , has to be exceeded in order to allow for a phase transition from liquid to solid.  $\Delta G$  is the sum of two energies involved in the process of phase transfer. On the one hand there is the so-called

---

energy of the bulk or activation energy  $\Delta F_{\text{act}}$  that is released when water molecules arrange in the more stable ice phase. On the other hand, there is the interface energy  $\Delta F_{\text{g}}$  that is needed to keep the interface surface between the crystallized volume and the surrounding liquid layer in a stable state. For small ice clusters in a liquid water droplet the interface energy exceeds the energy released by the bulk. Hence, growth of the ice cluster is suppressed. While  $F_{\text{g}}$  does not significantly depend on temperature,  $F_{\text{act}}$  depends on temperature and the logarithm of the supersaturation. With decreasing temperature supersaturation over ice increases considerably. This, in turn, increases the bulk energy  $F_{\text{act}}$  and consequently improves the conditions for the formation of a stable ice cluster.

The parameter describing the effect of the temperature dependence of a freezing process is the nucleation rate  $J$  given in  $\text{cm}^{-3} \text{s}^{-1}$  [DeMott, 2002] as

$$J = C \exp\left(-\frac{\Delta G}{kT}\right) \quad (2.1)$$

with

$$\Delta G = \Delta F_{\text{act}} - \Delta F_{\text{g}} \quad (2.2)$$

and

$$C = N_c \left(\frac{\rho_w}{h\rho_i}\right) (\sigma_{i/s}kT)^{1/2} \quad (2.3)$$

where  $T$  is the temperature (in K),  $k$  is the Boltzmann constant,  $N_c$  is the monomer concentration of water molecules,  $\rho_w$  is the density of liquid water,  $\rho_i$  is the density of ice,  $h$  is the Planck's constant and  $\sigma_{i/s}$ , is the interfacial energy between the ice and the solution.

For positive values of  $\Delta G$  (energy is needed to sustain the ice germ), nucleation is rather inefficient because the exponential function in Eq. (2.1) is negative in that case. When free energy  $\Delta G$  is released, the exponential term is positive and the nucleation rate  $J$  increases exponentially. Only at temperatures below approximately  $-38$  °C  $\Delta G$  is large enough to allow for a significant homogeneous nucleation rate.

Because the formation of free energy is a statistical process, it is also dependent on time [DeMott, 2002]:

$$F_{\text{hf}} = 1 - \exp(-J_{\text{hf}}V_{\text{d}}\Delta t). \quad (2.4)$$

Here, the fraction  $F_{\text{hf}}$  of droplets with volume  $V_{\text{d}}$  that freeze homogeneously depends on the nucleation rate  $J_{\text{hf}}$  and on the small time interval  $\Delta t$ . Therefore, if constant conditions which may not allow ice nucleation are present for a longer period of time, freezing is still possible due to the probabilistic nature of the process.

In laboratory studies liquid water droplets have been observed down to temperatures of  $-41$  °C [Anderson *et al.*, 1980]. Pruppacher [1995] also documented a strong correlation between drop size and supercooling temperature. Whereas a supercooling of  $-36$  °C can be reached for droplets up to sizes of  $100$   $\mu\text{m}$ , droplets must be smaller than  $1$   $\mu\text{m}$  in order to allow for supercooling of more than  $-40$  °C. The results shown in Pruppacher [1995] also indicate that the onset temperature of ice formation increases for decreasing cooling rates of the probed cloud droplets. This may be attributed to the statistical process of ice germ

formation. The more time is available for the statistically less likely formation of large ice germs the higher the temperature for the onset of ice formation can be.

The temperatures of homogeneous nucleation listed above are based on laboratory studies performed with extra pure water. Measurements with aircraft or active remote sensing in the natural atmospheric environment yield varying onset temperatures of homogeneous nucleation. Field observations are performed for populations of cloud droplets with varying size distributions and lack precise information about cooling rates of the observed cloud parcels. Therefore, the lowest temperatures at which natural supercooled liquid water was found so far range from  $-36\text{ }^{\circ}\text{C}$  for an altocumulus cloud over Cape Verde [Ansmann *et al.*, 2009] to  $-40.7\text{ }^{\circ}\text{C}$  in wave clouds over the Rocky Mountains [Heymsfield and Sabin, 1989].

Even though no natural cloud droplets colder than  $-40.7\text{ }^{\circ}\text{C}$  were reported in literature, it is known that substances that are dissolved in a droplet decrease the freezing temperature of supercooled droplets [Hoffer, 1961; Koop *et al.*, 2000]. This freezing point depression is in general regarded to depend only on the volume fraction of the solute whereas it is independent of the type of solute [DeMott, 2002]. However, recently indications were found that freezing point depressions caused by organic compounds are stronger than respective depressions caused by sulfates and salts [Cziczo *et al.*, 2004a]. Cziczo *et al.* [2004a] reported observations of an unequal distribution of organic solutes in liquid water droplets and ice crystals within the same cloud. In contrast to this finding, other chemical species like sulfates and salts were found to be equally distributed in the aqueous and in the ice phase.

An effect that may not only prevent a supercooled droplet from freezing but also inhibit chemical processes inside of a droplet was recently reported by Zobrist *et al.* [2008]. Their laboratory studies revealed that high concentrations of dissolved organic substances can change the viscous state of a supercooled droplet to a state similar to glass. Formation of crystals as well as chemical reactions are suppressed in this case. However, the relevance of such processes in nature and in which way they may affect cloud microphysical and radiative properties has not been investigated yet.

## 2.2 Heterogeneous nucleation

At atmospheric temperatures above approximately  $-35\text{ }^{\circ}\text{C}$  which, according to the U.S. standard atmosphere of 1976, corresponds to altitudes of below 8000 m, ice nucleation in supercooled droplets cannot be triggered homogeneously. Heterogeneous ice nucleation that is initiated by insoluble aerosol particles must take place. The surface characteristics of these particles, i.e., size and morphology, solubility, epitaxial and active site distribution [Kulkarni and Dobbie, 2010] provide suitable conditions for the crystallization of water molecules which would not be able to form stable ice clusters homogeneously at such high temperatures. According to Eq. (2.2), the presence of an insoluble ice nucleus decreases the amount of interface energy  $\Delta F_g$  needed to keep the ice cluster stable. Thus it can be formed at either higher temperatures or lower supersaturation or both.

### 2.2.1 Heterogeneous nucleation processes

If the primary condition of the presence of insoluble aerosol particles is given, heterogeneous freezing can occur in various ways. In Fig. 2.1 the main, well-accepted processes are listed and their dependence on relative humidity and temperature is schematically shown. They are described in the following paragraphs.

All of the heterogeneous ice nucleation processes have in common that they need supersaturated conditions with respect to ice, such that  $RH_{ice} > 100\%$ . The only process that allows the direct formation of an ice crystal on the surface of an ice nucleus is the *deposition nucleation* mechanism. As soon as the relative humidity with respect to ice  $RH_{ice}$  exceeds 100%, water molecules may deposit directly on a suitable IN. Fig. 2.2 shows the temperature dependence of the water-vapor mixing ratio over ice surfaces (blue) and liquid-water surfaces (red) at standard-atmospheric conditions. The gray pattern indicates conditions at which only water vapor can exist. The blue-striped pattern denotes the range in which only deposition nucleation is possible. At mixing ratios exceeding ice supersaturation (blue graph) deposition nucleation can occur. At conditions exceeding water saturation (red graph), deposition freezing as well as the formation of liquid water droplets are possible and additional ice nucleation processes have to be considered.

One option is the so-called process of *condensation nucleation*. Here, a supercooled cloud droplet grows from a cloud condensation nucleus (CCN) or a haze particle. In the moment of drop formation an insoluble fraction of the haze particle or the CCN triggers ice nucleation in the newly formed droplet.

If the conditions for ice nucleation are not yet given at the level of water saturation more time or further cooling and thereby an increase of supersaturation with respect to ice may be necessary until freezing is triggered by the IN that is then immersed in the droplet. This process is referred to as *immersion nucleation*.

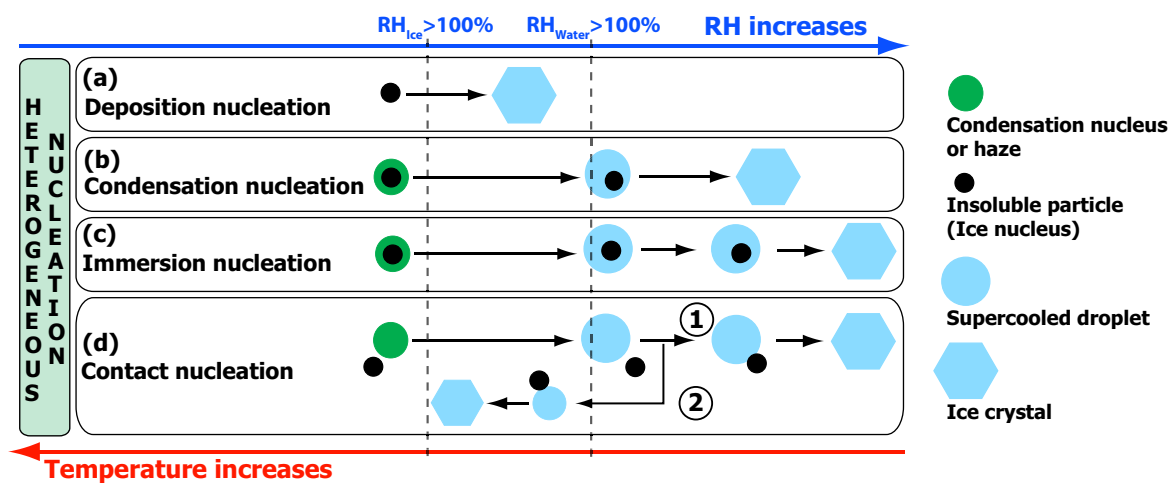


**Figure 2.1:** Illustration of the basic pathways leading to heterogeneous ice nucleation: deposition nucleation, condensation nucleation, immersion nucleation, and contact nucleation. The ice-formation processes are described in the text.

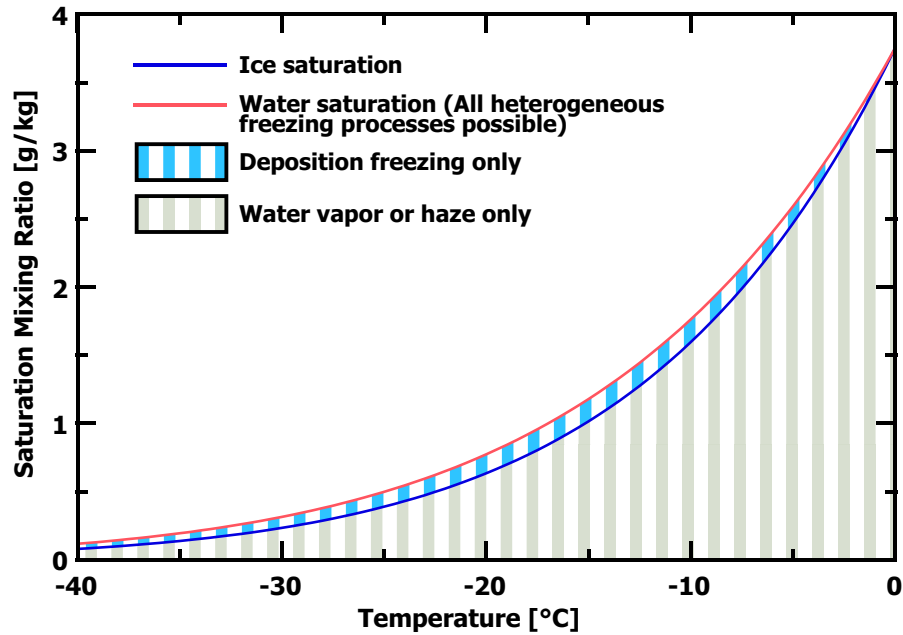


**Figure 2.2:** Saturation mixing ratio of ice (blue graph) and water (red graph) for temperatures between  $-40$  and  $0$  °C. The patterns indicate domains of deposition freezing (blue) and of no ice formation (gray). Only at humidity conditions that reach or exceed water saturation (red graph) all heterogeneous freezing processes (see Fig. 2.1) as well as the formation of supercooled liquid water can occur.

Ice nucleation in a supercooled droplet can also be caused from outside triggered by a collision of the droplet with a dry IN. This process, denoted *contact nucleation*, is effective when the condensation nucleus of the droplet consists only of soluble material or if the insoluble particle that is immersed in the droplet is a less effective IN compared to the one that triggered contact freezing. Contact freezing nucleation can occur either at  $\text{RH}_{\text{water}} > 100\%$  or at  $\text{RH}_{\text{water}} < 100\%$  during drop evaporation.

### 2.2.2 Studies of heterogeneous nucleation

From the processes listed in Fig. 2.1 it can be seen that heterogeneous freezing can occur in different ways. Parameters that determine the type of freezing are:

- temperature,
- hygroscopicity of the cloud condensation nuclei,
- supersaturation with respect to ice and water,
- freezing efficiency of the insoluble ice nuclei (aerosol type), and
- lifetime of the supercooled droplet.

The investigation of the relevance of these parameters for the ice nucleation rate in supercooled droplets has been subject of numerous studies. A favored approach are laboratory studies which enable to investigate ice formation under specified conditions. Hereby, experiments are focused on aerosol types that are frequent in the troposphere and contain at least a fraction of insoluble material. Common aerosol types from natural sources are mineral dust, soot, and biological particles [Pruppacher and Klett, 1997; Cantrell and Heymsfield, 2005]. Freezing temperatures found for these main substances vary strongly. Biological particles, including bacteria but also organic substances, were found to be very efficient ice nuclei. For bacteria, pollen, and leaf litter initial freezing temperatures varied from  $-7$  to  $-14$  °C [von Blohn et al., 2005; Levin and Yankofsky, 1983; Diehl et al., 2006]. In a study on the freezing efficiency of bacteria all observed droplets were frozen at  $-9$  °C already [Levin and Yankofsky, 1983].

Soot, which is generated during incomplete combustion of hydrocarbons, including sub-species as black carbon and organic carbon, is an aerosol species that is released into the atmosphere by various natural (forest fires and volcanic eruptions) and anthropogenic sources (fuel combustion and biomass-burning activities). The range of initial freezing temperatures of different types of soot was found to be between  $-18$  and  $-28$  °C [Diehl et al., 2006; Gorbunov et al., 2001]. The freezing efficiency strongly depends on the generating process that determines the shape and hygroscopicity of the produced soot particles.

Compared to the average yearly emission rates of 60 Tg for organic material [Penner, 1995] and of 50 Tg for soot [IPCC, 2001] mineral dust is by far the most abundant insoluble aerosol in the troposphere [Duce, 1995; IPCC, 2001]. The total amount of yearly mineral dust emissions is estimated to be 1000–3000 Tg. Higher emissions are only estimated for sea salt aerosol which according to IPCC [2001] contributes approximately 1000–6000 Tg per year. However, sea salt is strongly hygroscopic and therefore does not play a direct role in heterogeneous nucleation.

Beside their abundance in the troposphere [Tegen and Schepanski, 2009] dust particles are known to be effective IN. In early studies, clay material was found to trigger condensation nucleation at temperatures as high as  $-10$  °C and deposition nucleation at  $-19$  °C [Schaller and Fukuta, 1979]. The reason for the temperature difference between the two nucleation modes is the fraction of soluble, hygroscopic material in the clay. It supports droplet growth followed by initiation of ice nucleation due to the insoluble aerosol fraction that is immersed in the droplet [DeMott, 2002; Herich et al., 2009].

In recent experiments with different types of pure, uncoated dust in the 84-m<sup>3</sup> AIDA (Aerosol Interactions and Dynamics in the Atmosphere) cloud chamber [Möhler et al., 2001] no ice formation was initiated at temperatures above  $-20$  °C [Field et al., 2006; Connolly et al., 2009]. Additionally, deposition nucleation was found to be inactive down to  $-40$  °C [Field et al., 2006; Knopf and Koop, 2006] or of minor relevance [Connolly et al., 2009]. Instead, the formation of a droplet was usually observed before the onset of ice nucleation. These findings were supported by recent field observations reported by Ansmann et al. [2008, 2009]. Both studies describe observations of clouds with polarization lidar during the Saharan

---

Mineral Dust Experiment (SAMUM) at the subtropical site of Ouarzazate, southern Morocco (SAMUM-1) [Heintzenberg, 2009] and at the tropical site of Praia, Cape Verde Islands (SAMUM-2). During both campaigns more than 250 cloud layers were observed (31 over Morocco, 227 over Cape Verde) of which the majority were thin altocumulus clouds. They were generally embedded in stable layers in the mid troposphere. Since convection was absent, the clouds predominantly developed in air masses which did undergo slow large-scale lifting. During SAMUM-1 at Ouarzazate most clouds formed between 4 and 6 km height at the top of the omnipresent pure Saharan dust layer. Even under these conditions, which are highly preferable for heterogeneous nucleation by dust, ice formation was, after correction for secondary freezing effects (see Section 2.3), rarely observed at temperatures above  $-20$  °C. Additionally, liquid water was always observed before ice nucleation started. Hence, in agreement to the recent AIDA experiments, deposition and condensation nucleation were found to be of negligible relevance for the formation of ice in the observed thin altocumulus layers.

A contradictory notion of the role of Saharan dust as ice nuclei at temperatures above  $-20$  °C is given by Sassen *et al.* [2003]. They report the observation of a glaciated altocumulus cloud over the subtropical Caribbean Sea during CRYSTAL-FACE<sup>1</sup>. The altocumulus cloud occurred at temperatures between  $-5$  and  $-8$  °C and was embedded in an aerosol layer containing high concentrations of Saharan dust. Connolly *et al.* [2009] spent large portions of their discussion to interpret the discrepancies found between the studies of Ansmann *et al.* [2009] and the aforementioned publication of Sassen *et al.* [2003]. They argue that aging or coating of the Saharan dust during long-range transport may have led to the differences in the freezing temperatures between the clouds observed at Cape Verde and in the Caribbean.

Interestingly, a study of Roberts and Hallett [1968] also presented indications that dust particles initiated ice nucleation already at temperatures as high as  $-10$  °C after they were preactivated during a first freezing process at around  $-20$  °C. This effect is caused by the formation of a stable, thin ice-like film of water molecules on the preactivated particles [Roberts and Hallett, 1968; Cantrell and Heymsfield, 2005]. There are indications that the effect of preactivation may be relevant for tropospheric processes when dust particles undergo several freezing cycles during long-range transport.

Studies concerning the role of contact nucleation are scarce. Some information is compiled in Diehl *et al.* [2006]. A primary condition that is needed for contact nucleation to be efficient is the presence of both large ice nuclei and large droplets which increases the probability for a collision. Collision efficiency is usually derived from a collision kernel which describes the probability of a collision for variable sizes of the aerosol particles and cloud droplets [Kerkweg *et al.*, 2003]. In a wind tunnel study, Pitter and Pruppacher [1973] investigated the efficiency of contact, immersion, and condensation nucleation for mineral dust particles. They found initial freezing temperatures for contact nucleation of up to  $-3$  °C whereas immersion and condensation nucleation lead to the detection of first crystals only at temperatures below  $-12$

---

<sup>1</sup>CRYSTAL-FACE: Cirrus Regional Study of Tropical Anvils and Cirrus Layers – Florida Area Cirrus Experiment. Performed in July 2002.

---

to  $-14\text{ }^{\circ}\text{C}$  for the same particle type. Experiments of *Levin and Yankofsky* [1983] performed with bacteria also showed an increased fraction of ice in the contact mode compared to the immersion mode. Even though initial temperatures are high for both nucleation processes, the fraction of frozen drops was larger in the contact mode for the same temperature range. Soot that was found to be a less effective ice nuclei than mineral dust or biological particles [*Diehl and Mitra*, 1998] also shows increased contact nucleation efficiency. The fraction of frozen droplets at  $-18\text{ }^{\circ}\text{C}$  was considerably higher if contact freezing was allowed in addition to immersion and condensation freezing [*Gorbunov et al.*, 2001]. It should be noted that the initial or activation freezing temperature denotes the temperature at which a first single ice crystal is observed in the sampled volume. Temperatures that are not referred to be the initial values are typically median freezing temperatures that denote the temperature at which 50% of the observed droplets are frozen [*Diehl et al.*, 2006].

The general idea that mineral dust is the dominant IN in most regions of the globe is meanwhile widely accepted. IN measurements during field experiments revealed that the number fraction of mineral dust particles in residual aerosols of evaporated ice crystals is much higher than the corresponding dust–particle number fraction in ambient air [*Chen et al.*, 1998; *DeMott et al.*, 2003a; *Richardson et al.*, 2007; *Stith et al.*, 2009; *Kamphus et al.*, 2009]. During the second Ice Nuclei Spectroscopy (INSPECT II) campaign at the Storm Peak Laboratory (SPL, 3210 m above sea level) [*Borys and Wetzel*, 1997] in northwestern Colorado, USA, a number fraction of dust particles in ambient air of only a few percent was found [*Richardson et al.*, 2007]. In contrast, the number fraction of dust particles in the residual aerosols of the ice crystals was almost 40%. In turn, sulfate and organic aerosols which made up a fraction of 75% of the ambient aerosol particle population contributed less than 20% to the ice–crystal residuals. *Richardson et al.* [2007] also confirmed the hypothesis that metallic aerosols are very efficient IN. Whereas they contributed only approximately 3% to the total number of ambient aerosol particles, metallic particles made up more than 40% of the ice–crystal residuals. Comparable differences in the number fraction of mineral dust and metallic aerosol particles in the ambient air and in ice residuals were reported by *Kamphus et al.* [2009] who analyzed measurements performed at the mountain research station of Jungfrauoch mountain in Switzerland. More than 70% of the ice–crystal residual aerosol particles were classified as minerals (31%) or coated minerals (47%). Also metallic particles, with a total aerosol fraction of less than one percent, were found to make up 14% of the residual aerosol particles of ice crystals. Again, sulfates and organic particles were not found in the ice–crystal residuals whereas they made up a number fraction of 15% of the ambient aerosol.

Even though organic particles like bacteria, pollen, and leaf litter were reported to be very effective IN in the laboratory, field studies could not confirm these findings yet [*Kamphus et al.*, 2009; *Kulkarni and Dobbie*, 2010]. Instead, there are indications that freezing is suppressed by organic compounds dissolved in supercooled droplets. *Cziczo et al.* [2004b] and *Cozic et al.* [2008] compared the number fraction of residual particles from evaporated supercooled droplets with those of ice crystals probed within the same cloud. Besides the

---

finding that mineral dust was again the dominating IN, organic substances were found in a much lower fraction in ice crystals compared to supercooled droplets. In addition, very little is known about the vertical distribution of biological particles [Burrows *et al.*, 2009].

Measurements of the relation between ice nuclei concentration (INC) and large-aerosol particle concentration (APC) of particles with diameters larger than 250 nm were published by DeMott *et al.* [2003b], Richardson *et al.* [2007], and Stith *et al.* [2009]. Measured values of APC/INC ratios vary strongly and can take values from 20 to 2000. A range of APC/INC ratios from 50 to 1500 was found for mixed continental aerosols originating from the western United States. Their variation decreases remarkably if they are constraint to known types of aerosols. From measurements in aged Saharan dust during CRYSTAL-FACE APC/INC ratios of 20–130 were found [Stith *et al.*, 2009; DeMott *et al.*, 2009]. These values repeatedly demonstrate the high freezing efficiency of mineral dust in comparison to other aerosol species.

As a last point, particle size should be mentioned as a factor controlling the IN efficiency of aerosols. Already in the 1950's it was found that the size distribution of crystal residual aerosols is shifted to larger values compared to the aerosol size distribution in ambient air [Georgii, 1959; Mason, 1950]. Explicit values are given by Richardson *et al.* [2007] who found that 90% of the ambient particles are smaller than 0.5  $\mu\text{m}$  whereas ice crystal residuals were in 90% of the cases larger than 0.5  $\mu\text{m}$ . Consequently, measured onset temperatures of heterogeneous ice nucleation in laboratory studies vary significantly with the size of the selected mineral dust IN. Only for IN size distributions with mode diameters above 0.5  $\mu\text{m}$  onset temperatures of up to  $-10$  °C were found [Pitter and Pruppacher, 1973; Kanji and Abbatt, 2006; Knopf and Koop, 2006; Zimmermann *et al.*, 2008; Vali, 2008]. For mode diameters smaller than 0.5  $\mu\text{m}$  onset temperatures were below  $-20$  °C [Field *et al.*, 2006; Connolly *et al.*, 2009; Welti *et al.*, 2009].

## 2.3 Dynamical processes and ice multiplication

A more complicated scenario concerning heterogeneous ice nucleation emerges when atmospheric dynamics is involved in the formation of a cloud. Aircraft measurements are suitable to study the relation between cloud-droplet properties, ice-crystal properties, and cloud dynamics. From flights through 90 cumuliform and 72 stratiform clouds Hobbs and Rangno [1985] found that even under clean maritime conditions ice nucleation already occurs at temperatures between  $-4$  and  $-7$  °C. They found a strong correlation between the initial temperature of ice formation and the broadness of the drop size spectrum. Only for clouds that showed a significant number of droplets with diameters larger than 20  $\mu\text{m}$  ice was observed at temperatures above  $-10$  °C.

The findings of Hobbs and Rangno [1985] also indicated that ice-crystal concentrations may be up to several orders of magnitude higher than the number of IN. This is in agreement with other studies [Hobbs, 1969; Huffman, 1973; Meyers *et al.*, 1992; Fridlind *et al.*, 2007; Gayet *et al.*, 2009]. As a consequence, the classical ice nucleation mechanisms that are pre-

---

sented in Section 2.2 can be studied under laboratory conditions [Fletcher, 1962] but cannot satisfactorily describe natural ice crystal concentration [Meyers *et al.*, 1992]. New processes were hypothesized to explain the discrepancies. They can be separated into modifications of the primary ice nucleation mechanisms and into ice multiplication processes:

1. Under conditions when large supercooled droplets ( $d > 23 \mu\text{m}$ ) coexist with ice crystals the *Hallett–Mossop process* can lead to the production of ice crystals. Hallett and Mossop [1974] described the effect of ice crystal splintering during riming that is caused by the strong surface tensions which occur after the droplet freezes on the ice crystal. The Hallett–Mossop process was found to be only effective at temperatures between  $-3$  and  $-8 \text{ }^\circ\text{C}$  and during convective conditions with vertical velocities of at least  $1.4 \text{ m s}^{-1}$ . It is illustrated in Fig. 2.3.
2. Based on numerous observations of irregular crystals beneath convective clouds Vardi-man [1978] proposed the mechanism of production of secondary ice crystals by *crystal–crystal collisions*. Preferable conditions for mechanical fracturing are given again in strongly riming clouds with sufficiently strong turbulence to create the momentum that is necessary for the fragmentation. In convective clouds crystal fragmentation by collision was calculated to increase the number of ice crystals by a factor of 10–100. In stratiform clouds with weak turbulence and smaller volumes available for collision fragmentation the maximum factor of crystal increase was found to be less than 10.
3. In the case of vertical layering of clouds the nucleation of ice crystals in a higher, colder cloud layer can lead to the formation of ice virgae. If these virgae precipitate into a lower cloud layer that only contains supercooled droplets, further production of ice is triggered by the so-called *seeder–feeder mechanism* [Rutledge and Hobbs, 1983; Fleishauer *et al.*, 2002; Ansmann *et al.*, 2009]. The existing falling ice crystals grow by the Bergeron–Findeisen process that causes the supercooled droplets to shrink. From

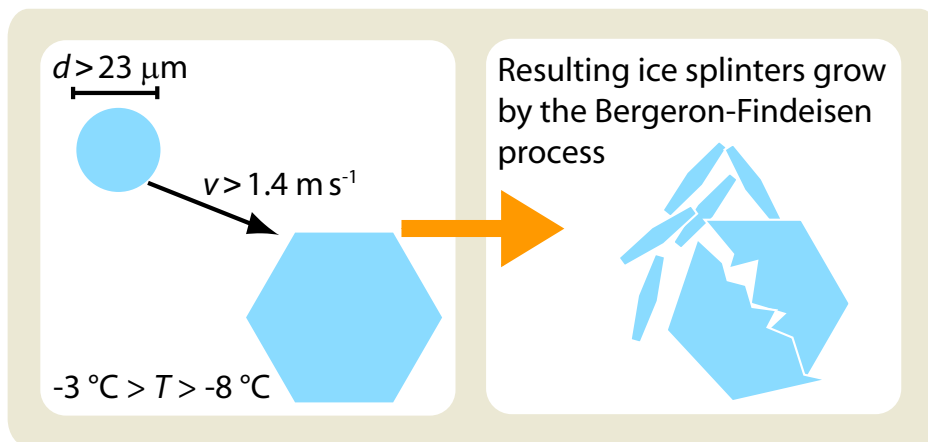


**Figure 2.3:** Scheme of the Hallett–Mossop ice-splintering process. Preferable temperatures for the process are in the range between  $-3$  and  $-8 \text{ }^\circ\text{C}$ . Updraft velocities of  $v > 1.4 \text{ m s}^{-1}$  are needed and the colliding drop must have a minimum diameter  $d$  of  $23 \mu\text{m}$ .

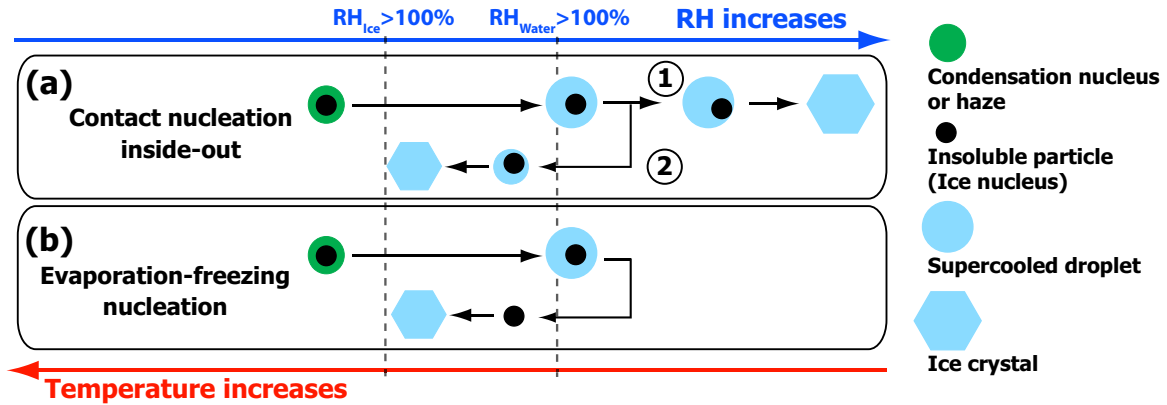


**Figure 2.4:** Illustration of further ice formation mechanisms. (a) Contact nucleation inside-out [Durant and Shaw, 2005]. (b) Production of evaporation IN [Rosinski and Morgan, 1991] from evaporating cloud drops and subsequent deposition nucleation denoted as evaporation-freezing nucleation. Contact nucleation inside-out and evaporation-freezing nucleation extend the pathways of contact nucleation and deposition freezing, respectively, which are presented in Fig. 2.1.

the cloud observations at Cape Verde Ansmann *et al.* [2009] found that the onset of ice formation is reduced by 5 K ( $-20\text{ }^{\circ}\text{C}$  instead of  $-15\text{ }^{\circ}\text{C}$ ) if the data set was corrected for the seeder-feeder mechanism.

4. *Contact nucleation inside-out*, a nucleation process that extends the relevance of the contact nucleation mechanism, was brought into consideration by studies of Durant and Shaw [2005]. From investigations of the heterogeneous nucleation efficiency of soot particles, they found that ice formation was initiated at 5 K higher temperatures ( $-15\text{ }^{\circ}\text{C}$  instead of  $-20\text{ }^{\circ}\text{C}$ ) if the soot particles had contact with the surface of the droplet instead of just being immersed in the droplet. Contact nucleation inside-out is illustrated in Fig. 2.4 (a).
5. Studies in the early 1990's gave indication that a fraction of the cloud-droplet residual particles after droplet evaporation can be effective IN [Rosinski and Morgan, 1991; Beard, 1992; Rosinski, 1995]. Rosinski and Morgan [1991] reported that one out of  $10^4$ – $10^5$  evaporated cloud droplets releases an IN that triggers deposition nucleation at temperatures as high as  $-4\text{ }^{\circ}\text{C}$ . Chemical reactions in the liquid phase may have altered the ice-nucleation efficiency of the aerosol particles that served before as CCN. The process of the production of IN by evaporation of cloud droplets is denoted *evaporation-freezing nucleation* [see Fig. 2.4 (b)]. It was the only plausible mechanism to match modeled ice crystal concentrations with measured ones [Fridlind *et al.*, 2007].

From the information given above it is obvious that the efficiency of three of the five mentioned processes depends strongly on cloud dynamics (turbulence). Only cloud seeding and contact nucleation inside-out can also occur in the case of weak vertical motions. This conclusion is in agreement with Hobbs and Rangno [1985] who found that the observation of

ice particles at high temperatures is strongly correlated to the turbulence in the cloud. Mixing and entrainment of air in the cloud provide favorable conditions for both evaporation and growth of large droplets. Consequently, the efficiency of most of the five above-mentioned processes for secondary ice nucleation and ice multiplication increases.

A publication of *Korolev et al.* [2003] provides a review of mid-latitude studies of the fraction of ice and water clouds as a function of temperature. All curves show a steady increase in ice cloud fraction from 0% at 0 °C to almost 100% at -20 °C. Taken the freezing efficiencies of the four main ice formation processes into account (see Fig. 2.1), such a strong increase in the ice fraction between 0 and -20 °C should not be expected. Hence, *Korolev et al.* [2003] concluded in agreement with *Hobbs and Rangno* [1985] and *Cotton and Field* [2002] that turbulent motions in connection with evaporation processes must be responsible for the high ice particle concentrations at temperatures above -20 °C. This hypothesis is indirectly corroborated by the studies of *Ansmann et al.* [2009]. The altocumulus clouds observed at Cape Verde showed very low geometrical and optical depths and simultaneously measured vertical motion within the clouds was weak. Slow large-scale lifting appeared to be mainly responsible for the formation of the clouds. Under such atmospheric conditions significant amounts of ice were almost never observed at temperatures above -20 °C, even though many of the observed clouds developed within aerosol layers containing high concentrations of Saharan dust and biomass-burning aerosol.

---

## Chapter 3

# Motivating questions for the present study

In order to facilitate the analysis of the 11-year cloud–aerosol data set consisting of a huge number of lidar profiles (vertical resolution of 60 m, temporal resolution of 10–60 s) and also the subsequent discussion of the results this work is concentrated on five questions listed below. These questions arise from the literature that was reviewed in Chapter 2.

### 1. Is there a clear dependence of the formation and presence of ice on cloud top temperature?

From aircraft studies only weak indications for a temperature dependence of heterogeneous ice nucleation were found. Mid-latitude cloud statistics from aircraft observations show the onset of ice formation already at about  $-5\text{ }^{\circ}\text{C}$  [Pruppacher, 1995 (Chapter 2), Korolev *et al.*, 2003]. Almost no liquid water has been observed at temperatures below  $-25$  to  $-30\text{ }^{\circ}\text{C}$ . Virtually no temperature relation was reported by Hobbs and Rangno [1985]. However, these aircraft studies lack reliable information on cloud top temperatures or of temperatures at which ice formation started. Lidar allows the height and time-resolved observation of cloud layers. Cloud top heights can be determined and associated to corresponding atmospheric temperatures. Cloud regions containing supercooled water or ice crystals can be discriminated. With this information, the lidar-based studies of Ansmann *et al.* [2009] revealed an onset of ice formation in shallow tropical clouds at temperatures below  $-20$  to  $-25\text{ }^{\circ}\text{C}$  only. However, lidar is known to be restricted to non-precipitating conditions and clouds can only be penetrated up to optical depths of approximately 3. Does this limitation have an impact on the observed relation between the presence of ice and ambient temperature in comparison to already existing cloud studies? Does the mid-latitude cloud data set that is analyzed in the scope of this study show similarities to the tropical lidar study? Or is this mid-latitude data set comparable to the already existing cloud studies that are based on aircraft measurements at comparable latitudes?

---

2. **Do the observations corroborate the hypothesis that freezing by deposition nucleation and condensation nucleation are of minor importance for the heterogeneous nucleation of ice?**

Recent laboratory studies of *Field et al.* [2006] and *Connolly et al.* [2009] give strong indication that heterogeneous ice nucleation at temperatures above  $-30$  to  $-25$  °C requires the presence of supercooled droplets before nucleation is initiated. Consequently, ice formation would be dominated by immersion and contact nucleation which both need the presence of supercooled liquid water droplets in order to be effective. Also, the altocumulus clouds observed by *Ansmann et al.* [2008, 2009] in general showed layers of supercooled liquid water at their tops which already implies an increased relevance of immersion and contact nucleation for ice formation in ambient clouds.

3. **Is it possible to clearly identify the influence of Saharan dust on ice formation in ambient clouds on the basis of the long-term lidar data set of IFT?**

From measurements of ice crystal residuals it is known that mineral dust is the major IN [*Richardson et al.*, 2007; *Kamphus et al.*, 2009]. However, is the atmospheric background concentration of mineral dust already sufficiently high, so that an increased dust concentration does not necessarily improve conditions for ice nucleation at a given temperature? This study is the first one that correlates the presence of ice with temperature and considers in addition ambient aerosol properties. There is no literature to compare with. However, the large amount of cloud cases contained in the long-term height-resolved lidar data set of IFT in association with the unique location of Leipzig with its frequent changes of the dominating air mass at least allows for a separation of dust-laden clouds from dust-free clouds. Thus the investigation of the impact of air masses containing a considerable amount of dust on ice formation is possible.

4. **Provided a clear effect of Saharan dust on ice formation is observed, is it possible to separate and quantify the aerosol-related and the meteorological (dynamical and thermodynamical) influence on heterogeneous ice nucleation in tropospheric stratiform clouds?**

The observations of *Ansmann et al.* [2009] in the tropics revealed that even clouds that are embedded in dense layers of Saharan dust and biomass-burning smoke are not likely to glaciate at temperatures above  $-20$  °C. However, the meteorological conditions in the tropical troposphere were characterized by weak dynamics during SAMUM-2. The meteorological situation is likely to be different at the central-European site of Leipzig with its strong frontal activity. By comparing our cloud observations in the tropics and in mid latitudes an estimation of the impact of atmospheric dynamics on ice formation may be possible.

5. **One question arises from the technical point of view: Is it possible to unambiguously separate ice-containing from pure liquid-water clouds based**
-

**on data of a zenith–pointing lidar as it was used for this study?**

When the laser beam of a lidar is pointed to the zenith, specular reflection by aligned falling ice crystals completely masks the detection of ice crystals as explained below. Because this question is of fundamental importance for the entire study, an extended section is devoted to this problem (Section 5.6). Extensive measurements with three lidars were performed to investigate specular reflection in ice–containing clouds.

---



## Chapter 4

# IfT Earlinet lidar MARTHA

### 4.1 IfT lidar system MARTHA

The Multiwavelength Atmospheric Raman lidar for Temperature, Humidity, and Aerosol profiling (MARTHA) is installed in the upper floor of the Leibniz Institute for Tropospheric Research (IfT) in Leipzig, Germany (51.1° N, 12.5° E, 125 m above sea level). The system is described in detail in *Mattis [2002]* and *Mattis [2002]*. A scheme of the setup is shown in Fig. 4.1.

The light source of MARTHA is a Nd:YAG laser that emits pulses at a wavelength of 1064 nm with a pulse length of 8–9 ns and a repetition rate of 30 Hz. Non-linear crystals shift a fraction of the emitted energy to frequencies of 532 and 355 nm. The polarization of the emitted light is elliptical at 1064 nm and linear at 355 and 532 nm. A beam expander increases the width of the overlaid beams from 10 mm to 150 mm. The expanded has a divergence of below 0.1 mrad and is transmitted into the atmosphere via an elliptical folding mirror.

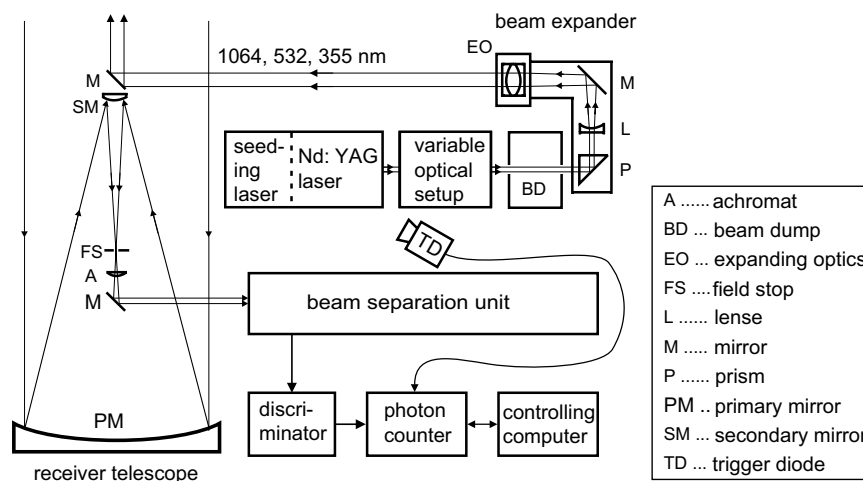
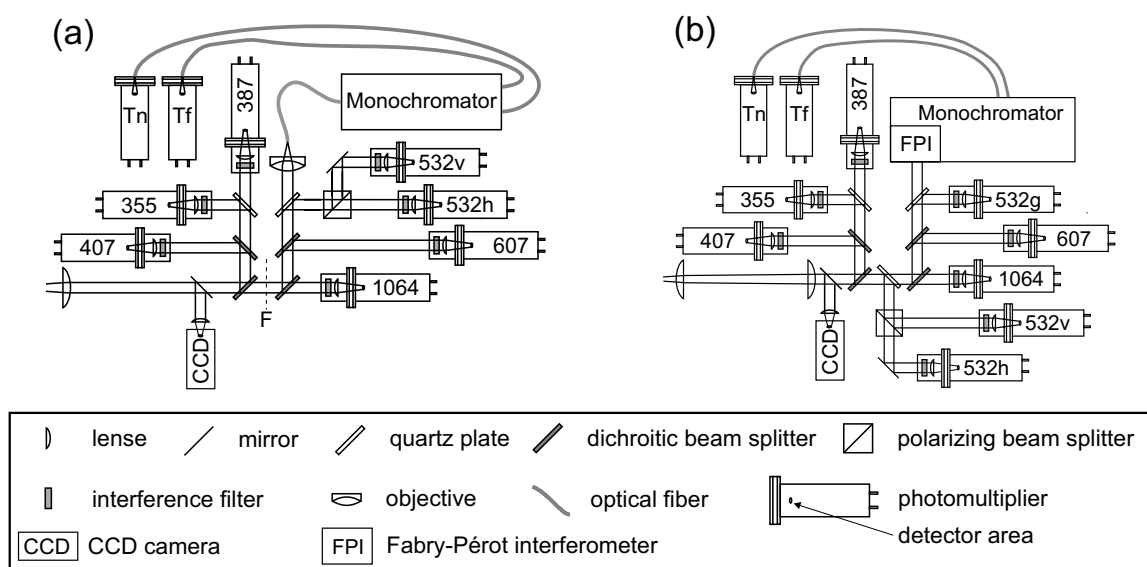


Figure 4.1: Sketch of the aerosol Raman lidar MARTHA.

The light that is backscattered from atmospheric constituents to the lidar is collected with a 1-m Cassegrain telescope which consists of a parabolic primary mirror and a hyperbolic secondary mirror. A system of achromatic lenses collimates the received light to a beam with a diameter of 30 mm that is directed to the beam separation unit. There, the signals of interest are separated by means of mirrors, quartz plates, dichroic beam splitters, interference filters, and a Fabry-Pérot interferometer (FPI).

The beam-separation unit was upgraded in March 2001. The old and the new layout of the beam-separation unit are shown in Fig. 4.2. Both setups have measurement channels for the detection of elastically scattered signals at the emission wavelengths of 355, 532, and 1064 nm and the Raman-scattered signals of nitrogen at 387 and 607 nm as well as of water vapor at 407 nm. Additionally, two pure rotational Raman lines (Tn and Tf in Fig. 4.2) were separated at 532 nm for the detection of atmospheric temperature. In the first configuration, light at 532 nm was detected separately in cross- (532h) and co-polarized (532v) direction with respect to the polarization direction of the laser. No total signal was measured at 532 nm.

During the upgrade, the optical path of the returned light was optimized. A new optical branch was installed to separate the polarization components at 532 nm, and a new detector was installed to measure the total signal at 532 nm (532g). The upgrade brought additional



**Figure 4.2:** Old and new layout of the beam-separation unit of MARTHA. (a) 1997 – February 2001. (b) March 2001 – June 2008. The labels of the photomultiplier tubes denote the detected wavelength. In addition, g, v, and h denote the total signal and the vertical and horizontal polarization components, respectively. Tn and Tf are the channels for temperature detection for the near and far rotational Raman lines, respectively [Mattis, 2002]. The dashed line marked with an F denotes the focal plane of the lense at the entrance point of the beam. The mirror in front of the CCD camera is movable. It is only put into the optical path for alignment of the transmitter-receiver configuration with the CCD camera.

improvements to the detection accuracy of the rotational Raman lines for the temperature measurement by means of the installation of a FPI. Detailed descriptions of the optical components in the beam–separation unit can be found in *Mattis* [2002] and *Grein* [2006].

## 4.2 Lidar equation

Following the notation of *Mattis* [2002] the detected signal strength  ${}^pP(R, \lambda)$  at a specific wavelength  $\lambda$  and state of polarization  $p$  that is received from the distance  $R$  of the lidar can be described by the lidar equation:

$${}^pP(R, \lambda) = P_0(\lambda) \underbrace{\frac{{}^p\eta(\lambda)t(\lambda)cA_{\text{Tel}}}{2}}_I \underbrace{\frac{O(R)}{R^2}}_{II} \underbrace{{}^p\beta(R, \lambda)}_{III} \underbrace{\exp\left[-2\int_0^R \alpha(r, \lambda)dr\right]}_{IV}. \quad (4.1)$$

The parameters in Eq. (4.1) denote:

Index $p$	the considered state of polarization,
$\lambda$	the wavelength of detection,
$R$	the range from the lidar receiver,
${}^pP(R, \lambda)$	the received power,
$P_0(\lambda)$	the emitted pulse power,
${}^p\eta(\lambda)$	the transmission efficiency of the lidar receiver for light of polarization $p$ ,
$t(\lambda)$	the temporal pulse length,
$c$	the speed of light,
$A_{\text{Tel}}$	the area of the receiver telescope,
$O(R)$	the overlap function,
${}^p\beta(R, \lambda)$	the backscatter coefficient, and
$\alpha(R, \lambda)$	the extinction coefficient.

According to Eq. (4.1) the received lidar signal  ${}^pP(R, \lambda)$  depends on four terms that alter the power  $P_0(\lambda)$  of the emitted laser pulse [*Wandinger*, 2005].

Term I includes the range–independent parameters of the lidar system, which are the laser pulse length  $t(\lambda)$ , the transmissivity of the optical components  ${}^p\eta(\lambda)$ , the telescope area  $A_{\text{Tel}}$ , and the speed of light  $c$ . They are usually combined into the system–efficiency term

$$E(\lambda) = \frac{ct(\lambda){}^p\eta(\lambda)A_{\text{Tel}}}{2}. \quad (4.2)$$

Term II accounts for geometrical effects which determine the range dependence of the received signal. The power received by the telescope from the scattering volume that encloses the propagating laser pulse decreases proportional to  $R^{-2}$ . The overlap function  $O(R)$  describes the fraction of laser light that is within the field of view of the receiving telescope and imaged onto the photodetector.  $O(R)$  increases with range and equals 1 in the case of complete overlap. The range at which  $O(R) = 1$  depends on the geometrical properties of the receiver telescope and usually varies between a few hundred meters and several kilometers.

Term III contains the backscatter coefficient  ${}^p\beta(R)$  that describes the fraction of light that is scattered back at  $180^\circ$  from the range  $R$  to the receiver telescope and at state of polarization  $p$ .

Term IV, the transmission, describes the attenuation of light along its path through the atmosphere. According to Lambert–Beer’s law the intensity of light that passes a scattering medium with the extinction coefficient  $\alpha(R)$  depends exponentially on the optical depth  $\tau$  of the medium with  $\tau = -2 \int_0^R \alpha(r, \lambda) dr$ . The factor of 2 arises from the fact that backscattered light has to pass the distance from the lidar to the range  $R$  twice.

With the backscatter coefficient  $\beta$  and the extinction coefficient  $\alpha$ , Eq. (4.1) contains two parameters that describe the optical properties of the probed atmosphere. The extinction coefficient is the sum of the absorption coefficient  $\alpha_a$  and the scattering coefficient  $\alpha_s$ . Both, the extinction and backscatter coefficient, contain a fraction that is attributed to scattering by air molecules (mol) and a fraction from scattering by particles (par). Therefore,  $\beta$  and  $\alpha$  can be written as:

$$\begin{aligned}\alpha(\lambda) &= \alpha^{\text{mol}}(\lambda) + \alpha^{\text{par}}(\lambda) \\ &= \alpha_a^{\text{mol}}(\lambda) + \alpha_s^{\text{mol}}(\lambda) + \alpha_a^{\text{par}}(\lambda) + \alpha_s^{\text{par}}(\lambda)\end{aligned}\quad (4.3)$$

and

$${}^p\beta(\lambda) = {}^p\beta^{\text{mol}}(\lambda) + {}^p\beta^{\text{par}}(\lambda).\quad (4.4)$$

The backscatter coefficient  ${}^p\beta$  depends on the number concentration of scatterers  $N$ , the scattering cross section  ${}^p\sigma(\lambda)$ , and the scattering phase function  ${}^p\Phi(\lambda, \pi)$  of the scattering matter at the scattering angle  $\pi$  ( $180^\circ$  backscattering). It can be written as

$${}^p\beta(\lambda) = N {}^p\sigma(\lambda) {}^p\Phi(\lambda, \pi).\quad (4.5)$$

Because these parameters are known for air molecules,  $\alpha^{\text{mol}}$  and  $\beta^{\text{mol}}$  can be calculated for known profiles of temperature and pressure [Bucholtz, 1995] which can be derived from radiosonde data or a standard–atmosphere model.

Depending on the applied lidar system and the ambient measurement conditions different methods are available to derive  $\alpha^{\text{par}}$  and  $\beta^{\text{par}}$ . If only an elastic lidar signal is available, both coefficients have to be determined from this one measurement quantity. To solve this problem, a relation between  $\alpha^{\text{par}}$  and  $\beta^{\text{par}}$  has to be assumed. The technique that describes the retrieval of both values from only one available lidar signal is referred to as the Klett–Fernald method. In the case of a combined Raman elastic–backscatter lidar an elastically backscattered signal as well as an independently measured inelastically backscattered Raman signal are available. In that case  $\alpha^{\text{par}}$  and  $\beta^{\text{par}}$  can be unambiguously determined from the two measured signals. A review of both techniques can be found in Ansmann and Müller [2005]. A brief description is presented in the following two sections.

### 4.3 Particle backscatter coefficient

In order to obtain the bulk optical properties of scattering particles, the particle backscatter coefficient  $\beta^{\text{par}}$  is in general determined independently of the state of polarization from the total backscattered light. The parameter  $p$  is therefore neglected in the following section.

#### 4.3.1 Klett–Fernald method

For laser light of a specific wavelength and the simplifying assumptions of  $E = 1$  [see Eq. (4.2)] and a full overlap of  $O(R) = 1$  — both values are either known or vanish in the following derivations — and by using Eq. (4.3) and (4.4), Eq. (4.1) becomes

$$P(R) = \frac{P_0}{R^2} [\beta^{\text{mol}}(R) + \beta^{\text{par}}(R)] \exp \left\{ -2 \int_0^R [\alpha^{\text{mol}}(r) + \alpha^{\text{par}}(r)] dr \right\}. \quad (4.6)$$

To solve this equation for one of the two unknown variables  $\alpha$  or  $\beta$  a relation has to be assumed which connects both parameters. This is the extinction–to–backscatter or lidar ratio  $S^{\text{par}}$  of the scattering particles with

$$S^{\text{par}} = \frac{\alpha^{\text{par}}(R)}{\beta^{\text{par}}(R)}. \quad (4.7)$$

$S^{\text{par}}$  is assumed to be constant in the height range of interest, e.g., a cloud or aerosol layer. Equation (4.6) can be solved for  $\beta^{\text{par}}(R)$  after *Klett* [1981] and *Fernald* [1984]:

$$\beta^{\text{par}}(R) = -\beta^{\text{mol}}(R) + \frac{A(R_0, R)}{B(R_0) - 2S^{\text{par}} \int_{R_0}^R A(R_0, r) dr}, \quad (4.8)$$

with

$$A(R_0, x) = P(x)x^2 \exp \left[ -2(S^{\text{par}} - S^{\text{mol}}) \int_{R_0}^x \beta^{\text{mol}}(\xi) d\xi \right] \quad (4.9)$$

and

$$B(R_0) = \frac{P(R_0)R_0^2}{\beta^{\text{par}}(R_0) + \beta^{\text{mol}}(R_0)}. \quad (4.10)$$

The extinction–to–backscatter ratio of air  $S^{\text{mol}}$  is given by  $S^{\text{mol}} = \frac{8\pi}{3}K$  [*Collis and Russell*, 1976] with  $K$  being the King factor.

In order to determine  $\beta^{\text{par}}(R)$  from Eq. (4.8) the parameter  $\beta^{\text{par}}(R_0)$  in Eq. (4.10) has to be estimated at a specific reference height  $R_0$ . In the case of free–tropospheric clouds which are of main interest here, the calibration can be done below and above the cloud without causing large errors because usually the air is very clean at these heights. Below and above clouds one can therefore assume that  $\beta^{\text{par}}(R_0) \ll \beta^{\text{mol}}(R)$  for wavelengths  $\lambda \leq 532$  nm [*Ansmann*, 2002].

### 4.3.2 Raman method

MARTHA detects the inelastically scattered Raman signals of nitrogen at the wavelengths of 387 and 607 nm, with 355 and 532 nm being the primary emitted and elastically scattered wavelengths, respectively. The lidar equation for return signals from Raman scattering at the wavelength  $\lambda_{\text{Ra}}$  becomes

$$P(R, \lambda_{\text{Ra}}) = \frac{P_0}{R^2} \beta_{\text{Ra}}(R, \lambda_0) \times \exp \left\{ -2 \int_0^R \left[ \alpha^{\text{par}}(r, \lambda_0) + \alpha^{\text{mol}}(r, \lambda_0) + \alpha^{\text{par}}(r, \lambda_{\text{Ra}}) + \alpha^{\text{mol}}(r, \lambda_{\text{Ra}}) \right] dr \right\}. \quad (4.11)$$

with  $\beta_{\text{Ra}} = N_{\text{Ra}} \sigma_{\text{Ra}} \Phi_{\text{Ra}}$  which can, as mentioned in the description of Eq. (4.5), be calculated from the number concentration of the Raman-scattering molecules  $N_{\text{Ra}}$  and their backscattering cross section  $\sigma_{\text{Ra}} \Phi_{\text{Ra}}$  when pressure and temperature are known.

The particle backscatter coefficient  $\beta^{\text{par}}(R, \lambda_0)$  at the emitted wavelength  $\lambda_0$  can now be obtained from the ratio of the received elastically backscattered signal  $P(R, \lambda_0)$  [Eq. (4.6)] and the Raman signal  $P(R, \lambda_{\text{Ra}})$  [Eq. (4.11)] after *Ansmann et al.* [1992]:

$$\begin{aligned} \beta^{\text{par}}(R, \lambda_0) &= -\beta^{\text{mol}}(R, \lambda_0) + [\beta^{\text{par}}(R_0, \lambda_0) + \beta^{\text{mol}}(R_0, \lambda_0)] \\ &\quad \times \frac{P(R_0, \lambda_{\text{Ra}}) P(R, \lambda_0) N_{\text{Ra}}(R)}{P(R_0, \lambda_0) P(R, \lambda_{\text{Ra}}) N_{\text{Ra}}(R_0)} \\ &\quad \times \frac{\exp \left\{ -\int_{R_0}^R [\alpha^{\text{par}}(r, \lambda_{\text{Ra}}) + \alpha^{\text{mol}}(r, \lambda_{\text{Ra}})] dr \right\}}{\exp \left\{ -\int_{R_0}^R [\alpha^{\text{par}}(r, \lambda_0) + \alpha^{\text{mol}}(r, \lambda_0)] dr \right\}}. \end{aligned} \quad (4.12)$$

As for the Klett method, a reference value  $\beta^{\text{par}}(R_0, \lambda_0)$  is needed in order to solve Eq. (4.12). The reference height  $R_0$  is again set in a region with clear air or at a height where  $\beta^{\text{par}}(R_0, \lambda_0)$  is known.

## 4.4 Particle extinction coefficient

The particle extinction coefficient can be directly determined from the Raman lidar signal  $P(R, \lambda_{\text{Ra}})$  [*Ansmann et al.*, 1990]:

$$\alpha^{\text{par}}(R, \lambda_0) = \frac{1}{2} \frac{d}{dR} \ln \frac{N_{\text{Ra}}(R)}{P(R, \lambda_{\text{Ra}}) R^2} - \alpha^{\text{mol}}(R, \lambda_0) - \alpha^{\text{mol}}(R, \lambda_{\text{Ra}}). \quad (4.13)$$

Equation (4.13) is valid for wavelength-independent extinction, as it is the case for cirrus and water clouds in the visible wavelength range [*Ansmann*, 2002]. The values of  $N_{\text{Ra}}$  and  $\alpha^{\text{mol}}$  can be calculated from radiosonde temperature and pressure data or they can be estimated from standard-atmosphere conditions.

## 4.5 Depolarization ratio

The linear depolarization ratio is measured by utilizing a laser that emits linearly polarized radiation. Measurement channels are setup to measure light that is polarized parallel (co-polarized,  $\parallel$ ) to the plane of polarization of the emitted light or that is polarized perpendicular to the plane of polarization of the emitted laser light. The latter is denoted the cross-polarized component ( $\perp$ ). Writing Eq. (4.1) for the parallel and the perpendicular polarized components yields the powers  $\parallel P_{\text{Tel}}(R, \lambda)$  and  $\perp P_{\text{Tel}}(R, \lambda)$  that arrive at the telescope (Tel) of the lidar:

$$\parallel P_{\text{Tel}}(R, \lambda) = \parallel P_0(R) \frac{t(\lambda)cA_{\text{Tel}}}{2} \frac{O(R)}{R^2} \parallel \beta(R) \exp(-2\parallel\tau) \quad (4.14)$$

$$\perp P_{\text{Tel}}(R, \lambda) = \parallel P_0(R) \frac{t(\lambda)cA_{\text{Tel}}}{2} \frac{O(R)}{R^2} \perp \beta(R) \exp[-(\parallel\tau + \perp\tau)]. \quad (4.15)$$

The linear volume depolarization ratio  $\delta(R, \lambda)$  is now defined as the ratio of  $\perp P_{\text{Tel}}(R, \lambda)$  to  $\parallel P_{\text{Tel}}(R, \lambda)$ , resulting in [Schotland *et al.*, 1971]:

$$\delta(R, \lambda) = \frac{\perp P_{\text{Tel}}(R, \lambda)}{\parallel P_{\text{Tel}}(R, \lambda)} = \frac{\perp \beta(R, \lambda)}{\parallel \beta(R, \lambda)} \exp(\parallel\tau - \perp\tau). \quad (4.16)$$

The optical depths  $\perp\tau$  and  $\parallel\tau$  for the two polarization components are assumed to be equal so that the transmission term in Eq. (4.16) can be set to one [Schotland *et al.*, 1971; Sassen, 2005b; Grein, 2006]. A lidar system is usually set up in a way that the overlap function  $O(R)$  and all parts of the system–efficiency term  $E(R)$  [see Eq. (4.2)] are equal for both polarization components and thus cancel out in Eq. (4.16). The efficiency parameter  ${}^{\text{p}}\eta(\lambda)$  from Eq. (4.2) is not included in Eq. (4.14) and (4.15) because it is only used to describe the transmission efficiency of the received light between the telescope and the detector.

The depolarization ratio defined in Eq. (4.16) is in general referred to as linear volume depolarization  $\delta^{\text{vol}}$  because it is based on the ratio of the total backscatter coefficients  $\beta = \beta^{\text{par}} + \beta^{\text{mol}}$ . Whereas  $\delta^{\text{vol}}$  can be calculated directly from the detected signals the particle depolarization ratio  $\delta^{\text{par}}$  requires knowledge of the total particle backscatter coefficient  ${}^{\text{p}}\beta^{\text{par}}$  [Mattis, 2002]. In the case of strong backscattering by clouds  $\beta^{\text{par}} \gg \beta^{\text{mol}}$  so that  $\delta^{\text{vol}} \approx \delta^{\text{par}}$ . In the following, all occurrences of  $\delta$  refer to the volume depolarization ratio.

Because of instrumental and optical effects which occur within the beam–separation unit between the telescope and the detector (Det) the power  $P_{\text{Det}}(R, \lambda)$  received at the detector (see Section 4.1) contains contributions of both, the co-polarized and cross-polarized components of the received light. The extent to which each polarization component contributes to the detected signal is described by the efficiency parameter  ${}^{\text{p}}\eta_{\text{Det}}$  [Grein, 2006] introduced in Eq. (4.1):

$$P_{\text{Det}}(R, \lambda) = \parallel \eta_{\text{Det}} \parallel P_{\text{Tel}}(R, \lambda) + \perp \eta_{\text{Det}} \perp P_{\text{Tel}}(R, \lambda) = \parallel P_{\text{Det}}(R, \lambda) + \perp P_{\text{Det}}(R, \lambda). \quad (4.17)$$

In order to determine the depolarization ratio from the signal  $P_{\text{Det}}(R, \lambda)$  that is received by the detectors,  $\perp P_{\text{Tel}}(R, \lambda)$  and  $\parallel P_{\text{Tel}}(R, \lambda)$  from Eq. (4.17) need to be inserted into Eq. (4.16).

The calculation can be performed either in an exact way or in an idealized way. Both techniques are described below.

#### 4.5.1 Depolarization ratio for idealized systems

Usually, the co-polarized and cross-polarized components of the received lidar signal are detected separately with two different detectors. In the case of MARTHA these are the detection channels 532h for the cross-polarized component (subscripted with ‘cross’) and 532v for the co-polarized component (subscripted with ‘co’) that were introduced in Section 4.1. When both detectors are assumed to be ideal, the respective other polarization component of each channel does not contribute to the detected signal so that  ${}^{\perp}P_{\text{co}}(R, \lambda) \ll {}^{\parallel}P_{\text{co}}(R, \lambda)$  and  ${}^{\parallel}P_{\text{cross}}(R, \lambda) \ll {}^{\perp}P_{\text{cross}}(R, \lambda)$ . Simplifying Eq. (4.17) with this assumption and applying it to Eq. (4.16) yields:

$$\delta(R, \lambda) = \frac{{}^{\parallel}\eta_{\text{co}}P_{\text{cross}}(R, \lambda)}{{}^{\perp}\eta_{\text{cross}}P_{\text{co}}(R, \lambda)} = C \frac{P_{\text{cross}}(R, \lambda)}{P_{\text{co}}(R, \lambda)}. \quad (4.18)$$

Because the determination of the efficiency parameters  ${}^{\parallel}\eta_{\text{co}}$  and  ${}^{\perp}\eta_{\text{cross}}$  is difficult the resulting calibration factor  $C = \frac{{}^{\parallel}\eta_{\text{co}}}{{}^{\perp}\eta_{\text{cross}}}$  needs to be calculated at a range  $R_0$  where  $\delta(R_0, \lambda)$  is known. This is usually done in a particle-free region of the atmosphere where depolarization is only caused by scattering from air molecules. This type of depolarization, denoted Rayleigh depolarization  $\delta^{\text{Ray}}$ , can be calculated [Cairo *et al.*, 1999]. For MARTHA  $\delta^{\text{Ray}} = 0.0142$  [Mattis, 2002]. Because  $\delta^{\text{Ray}}$  depends especially on the bandwidth of the interference filters of each detection channel its value can vary for different lidar systems.

#### 4.5.2 Depolarization ratio for non-idealized systems

In order to obtain the best accuracy in the retrieved values of the depolarization ratio one must take into account that the retrieved signal of each polarization component always contains a fraction of the respective unwanted polarization component. This process is referred to as cross-talk. Even with a correct optical setup a complete attenuation of the unwanted polarization component cannot be achieved [Grein, 2006]. Therefore, Eq. (4.17) in reality always has full validity. Inserting Eq. (4.16) into Eq. (4.17) yields

$$P_{\text{Det}}(R, \lambda) = {}^{\parallel}\eta_{\text{Det}}P_{\text{Tel}}(R, \lambda) \left( \frac{1 + D_{\text{Det}}\delta(R, \lambda)}{1 + \delta(R, \lambda)} \right), \quad (4.19)$$

with

$$D_{\text{Det}}(\lambda) = \frac{{}^{\perp}\eta_{\text{Det}}}{{}^{\parallel}\eta_{\text{Det}}}. \quad (4.20)$$

$D_{\text{Det}}$  is the transmission ratio of the optical elements between telescope and detector. It describes the ratio of the transmission efficiencies  ${}^{\text{p}}\eta_{\text{Det}}$  of each polarization component.

When signals of a specific wavelength are detected with two detectors  $k$  and  $l$  and two different transmission ratios  $D_k$  and  $D_l$ , the depolarization ratio can be determined from

the ratio of the respective versions of Eq. (4.19) for  $P_k(R, \lambda)$  and  $P_l(R, \lambda)$ , yielding [Grein, 2006]:

$$\delta_{kl}(R, \lambda) = \frac{C_{kl} - v_{kl}(R, \lambda)}{D_l} v_{kl}(R, \lambda) - D_k C_{kl}, \quad (4.21)$$

with

$$v_{kl}(R, \lambda) = \frac{P_k(R, \lambda)}{P_l(R, \lambda)} \quad \text{and} \quad C_{kl} = \frac{\|\eta_k\|}{\|\eta_l\|}.$$

$D_k$  and  $D_l$  have to be determined from the manufacturer information for the optical components or from measurements.  $C_{kl}$  can be calculated in a particle-free region  $R_0$  of the atmosphere, where  $\delta_{kl}(R_0, \lambda) = \delta^{\text{Ray}} = 0.0142$ . Theoretically, any signal combination  $k, l$  can be used to determine the depolarization ratio with Eq. (4.21) as long as both channels have different transmission ratios  $D_k$  and  $D_l$ . In the case of MARTHA the following detector combinations are available for application:

- $k = 532\text{h}, l = 532\text{v}$  with  $D_{532\text{h}}$  and  $D_{532\text{v}}$  needed to be known.
- $k = 532\text{g}, l = 532\text{h}$  with  $D_{532\text{g}}$  and  $D_{532\text{h}}$  needed to be known.

Due to the large temporal extent of the analyzed data set in this study, different approaches had to be applied in order to calculate depolarization-ratio profiles for the full time period from 1997 to 2008. As described in Section 4.1, the beam separation unit of MARTHA experienced a major upgrade in March 2001. Before March 2001, only a co-polarized (532v) and a cross-polarized channel (532h) were available whereas afterwards an additional channel for the detection of the total signal (532g) was installed and the arrangement of the detectors 532v and 532h was optimized. Unfortunately, the transmission ratios  $D_{\text{Det}}$  of the detectors 532v and 532h that are needed to solve Eq. (4.21) were not determined for the old setup of the beam-separation unit. The experimental determination of the transmission ratios of the new setup was performed in the scope of a diploma thesis [Grein, 2006]. Because the setup was not modified between March 2001 and 2006, the transmission ratios published in Grein [2006] are assumed to be valid for the entire time period since March 2001. Table 4.1 lists the detectors that were available for the two setups of the beam-separation unit. Corresponding transmission ratios (if available) are given, and the equations that were used to analyze data from the respective time periods are specified.

**Table 4.1:** Parameters and equations used for the calculation of the linear volume depolarization ratio  $\delta^{\text{vol}}$  for the two different setups of the beam separation unit of MARTHA.

Time Period	$D_{532\text{v}}$	$D_{532\text{h}}$	$D_{532\text{g}}$	$\delta^{\text{vol}}$ calculated with
01/1997 – 03/2001	unknown	unknown	—	Eq. 4.18
03/2001 – 06/2008	$6.81 \cdot 10^{-3}$	138.2	0.218	Eq. 4.21



## Chapter 5

# Cloud detection with MARTHA

In this chapter, the data analysis procedure is described. From the lidar observations, cloud occurrence time, top and base heights, and cloud phase are determined. Output data of a meteorological model are analyzed to obtain cloud temperature information and to calculate backward trajectories. The backward trajectory analysis as well as dust transport modeling are used to determine the origin of air masses (and aerosols) in which the observed clouds formed.

An overview of the entire data analysis procedure is given in Fig. 5.1. The retrieval of cloud geometrical properties is presented in Section 5.1. Section 5.2 deals with the determination of meteorological parameters. The Hybrid Single-Particle Lagrangian Integrated Trajectory model (HYSPLIT) and the Dust Regional Atmospheric Model (DREAM) are explained in Section 5.3. One of the most important parts of this study, namely the determination of cloud phase, including the efforts required to allow an unambiguous identification of the ice phase in mixed-phase clouds is described in Sections 5.4 to 5.6.

### 5.1 Cloud geometrical properties

All measurements were screened for clouds. For each detected cloud layer cloud base and top height were determined as described by *Seifert et al.* [2007]. Cloud layers within complex cloud fields were counted as isolated, different cloud events, when they were vertically and temporally separated by more than 500 m and 5 minutes, respectively.

The identification of cloud layers is illustrated in Fig. 5.2. Strong backscattering [here in terms of the range-corrected signal  $PR^2$ , see Eq. (4.1)] at 1064 nm wavelength occurs in two cloud layers at heights around 3.5 and 10 km. The temporal extent, i.e., time of occurrence, of a cloud layer is defined as the time from the first to the last signal profile that shows enhanced backscattering. All signal profiles that were recorded within the time of occurrence of the cloud were averaged to yield one single profile. From that profile the cloud base  $H_b$  and top height  $H_t$  are determined. The cloud base is defined as the height bin above which the signal starts to increase with height. The cloud top is the height at which the signal decreases to a value below the signal at cloud base.

---

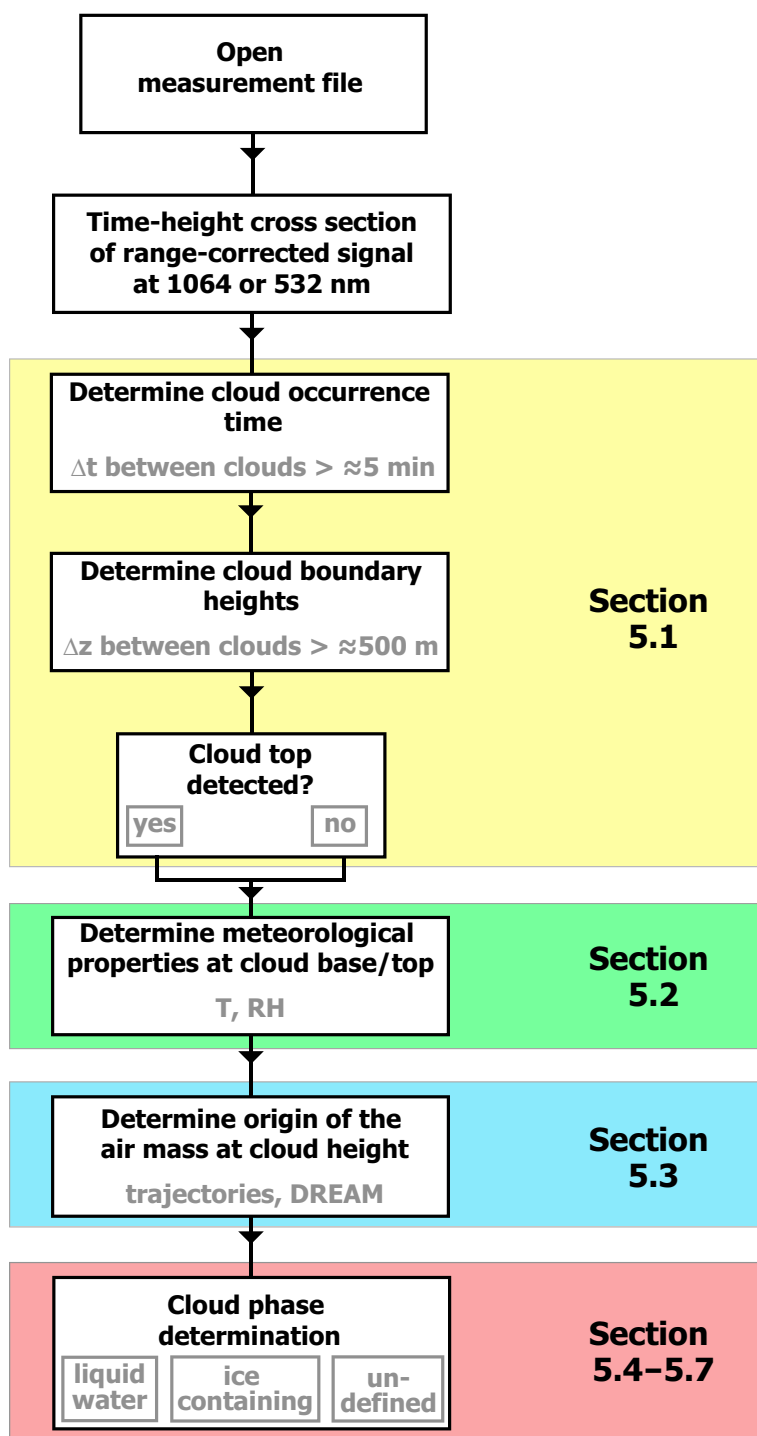


**Figure 5.1:** Overview of the data analysis steps required to analyze one cloud case. More than 2300 different cloud layers were identified during the 11-year observational period.

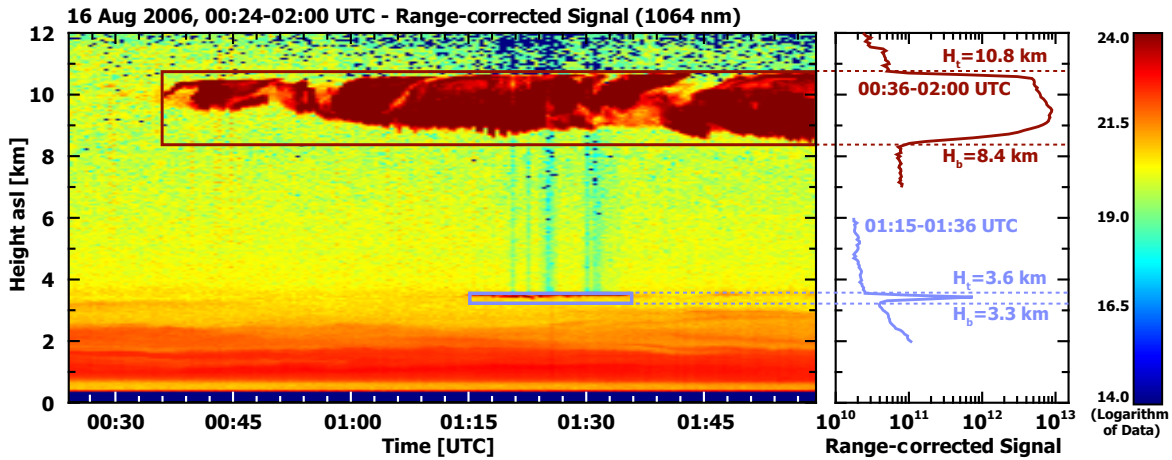


**Figure 5.2:** Example for the identification of geometrical cloud properties. Shown are the height–time cross section (left) and the average profile (right) of the 1064–nm range–corrected signal measured with MARTHA at Leipzig on 16 August 2006. Height above sea level (asl) is given. Two cloud layers were observed at around 3.5 km and 10 km, respectively. Colored frames denote the time of occurrence that is obtained from the cross section. The dashed lines show the cloud base and top heights  $H_b$  and  $H_t$ , respectively, that are obtained from the vertical signal profile.

Figure 5.3 shows an example of a cloud observation for which the cloud top identification is difficult. An extensive sensitivity study indicated that the cloud top  $H_t$  is detected as long as the ratio of the average signal  $P_{500}$  calculated between the apparent cloud top  $H_t$  and  $H_t + 500$  m (8.2–8.7 km in Fig. 5.3) and the background signal  $P_{BG}$  (from heights above 50 km) exceeds the value of 1.03. For signal ratios  $P_{500}/P_{BG} < 1.03$  the signals measured within 500 m above the apparent cloud top (where the signal dropped below the signal at cloud base) were already close to the background (caused by strong signal attenuation within the cloud), so that an unambiguous detection of the cloud top was no longer possible. For the example in Fig. 5.3, the noisy signal ratio ranged from 0.98–1.

## 5.2 Meteorological data

According to the flowchart in Fig. 5.1, information on cloud temperature and moisture conditions were determined next. To account for potential changes in the meteorological conditions with time, temperature and moisture profiles were determined for at least four times per day (00, 06, 12, and 18 UTC). Meteorological data from different sources were used for this study, including radiosondes and widely applied model data. Fig. 5.4 presents a timeline that shows which data sets were used as sources for vertical meteorological profiles. Radiosondes, which provide most accurate vertical meteorological profiles, were not regularly launched at Leipzig. The station closest to Leipzig that performed regular soundings for the German Meteorological Service (DWD) was Oppin (51.55° N, 12.07° E), located approximately 30 km northwest of Leipzig. However, radiosondes at Oppin were only launched

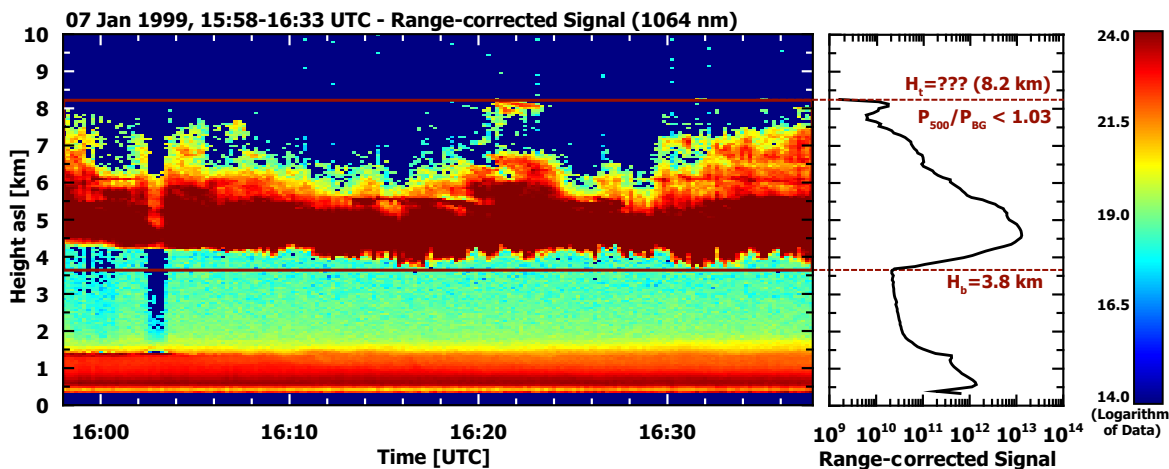


**Figure 5.3:** Example for the observation of a cloud layer with undefined cloud top. Shown are the height–time cross section (left) and the average profile (right) of the 1064–nm range–corrected signal measured with MARTHA at Leipzig on 7 January 1999. The calculated ratio  $P_{500}/P_{BG}$  of the signal 500 m above the apparent cloud–top level  $H_t$  (indicated by horizontal brown–colored lines at 8.2 km height) to the far–range background signal from above 50 km height was lower than 1.03.

between 12 September 2000 and 31 August 2006. Until 28 February 2006 soundings were performed every 12 hours. Between March and September 2006 only one sounding per day was performed at 00 UTC. To cover both the missing periods before and after the six–year Oppin sonde period as well as the time intervals between the soundings, data of the U.S. National Weather Service’s National Center for Environmental Prediction (NCEP) were used. NCEP maintains a data archive that contains the assimilated observational data used to initialize runs of weather forecast models. This archive is based on the global data assimilation system (GDAS, Kanamitsu [1989]) which stores the final assimilated data fields, including surface observations as well as radiosonde and satellite–based data. Between 1997 and November 2004 the assimilated data were archived in the FNL<sup>1</sup> database with a resolution of 5 hours, including all major meteorological parameters with a horizontal resolution of  $129 \times 129$  grid

<sup>1</sup>Assimilated data used to initialize the final (FNL) run of the global model of NCEP. Information and data available at: <http://www.arl.noaa.gov/fnl.php>

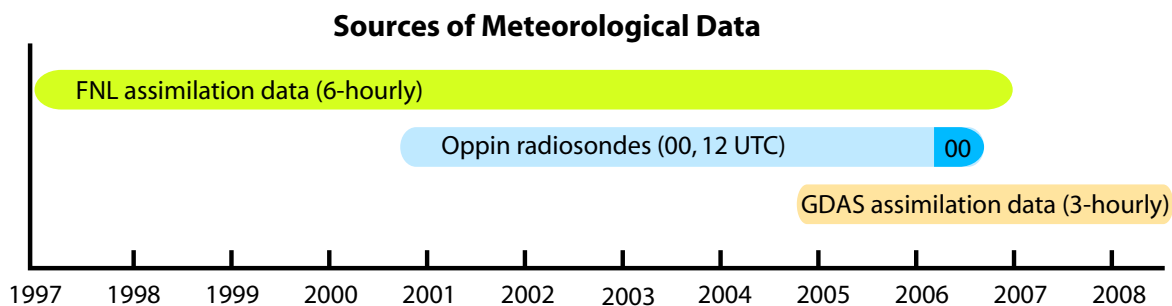


**Figure 5.4:** Scheme presenting the temporal availability of the three different sources of meteorological data.

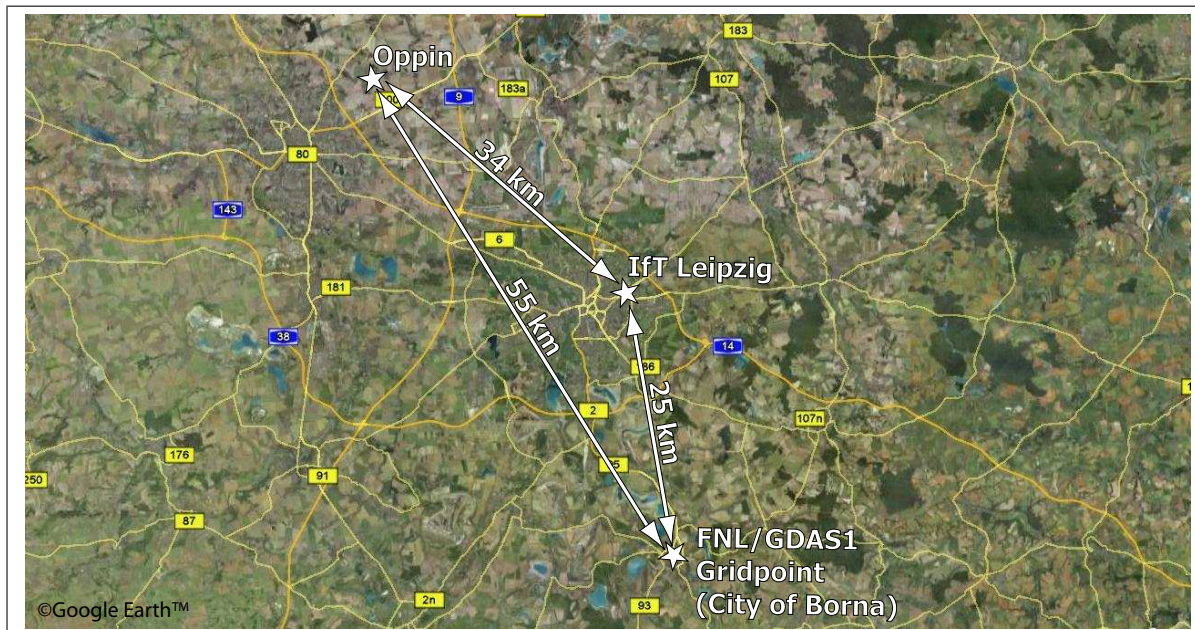


**Figure 5.5:** Map of the Leipzig area. Lidar observations are performed at IfT Leipzig. Radiosondes were launched by DWD at Oppin from 2000–2006. Model assimilation data (temperature and moisture profiles) were taken from the FNL/GDAS1 gridpoint close to the city of Borna.

points for each hemisphere and a vertical resolution of 13 layers. In December 2004 the archive was upgraded and renamed to GDAS1<sup>2</sup>. The temporal resolution was increased to 3 hours, the vertical resolution to 23 layers, and the horizontal resolution to  $1^\circ$ .

The grid point of both data archives that is closest to IfT is located at  $51.10^\circ$  N and  $12.50^\circ$  E. This location is close to the city of Borna south of Leipzig. In Fig. 5.5 the locations of IfT, the radiosonde station Oppin, and the model grid point, i. e., Borna, that was used for data analyses are shown. Both the model grid point as well as the Oppin radiosonde station are approximately 30 km away from IfT Leipzig and 55 km away from each other. For mid and upper tropospheric conditions the differences in the temperatures between both sounding locations should be small because they are generally driven by large-scale processes and not influenced by small-scale boundary-layer processes, especially over the flat terrain in the area around Leipzig.

In order to check for potential discrepancies between the archived assimilation data and temperature and humidity measured with the Oppin radiosondes, Fig. 5.6 shows the differences between radiosonde-derived temperature and relative humidity and model-based values. The levels of gray in the background illustrate the density of data points at the respective height. The solid lines are the mean differences with corresponding standard deviation shown as dashed lines. In the comparison of the temperature differences [Fig. 5.6 (a), (b)] remarkable differences for both archives are noticeable in the boundary layer up to

<sup>2</sup>Information and data of the GDAS1 archive available at: <http://www.arl.noaa.gov/gdas.php>

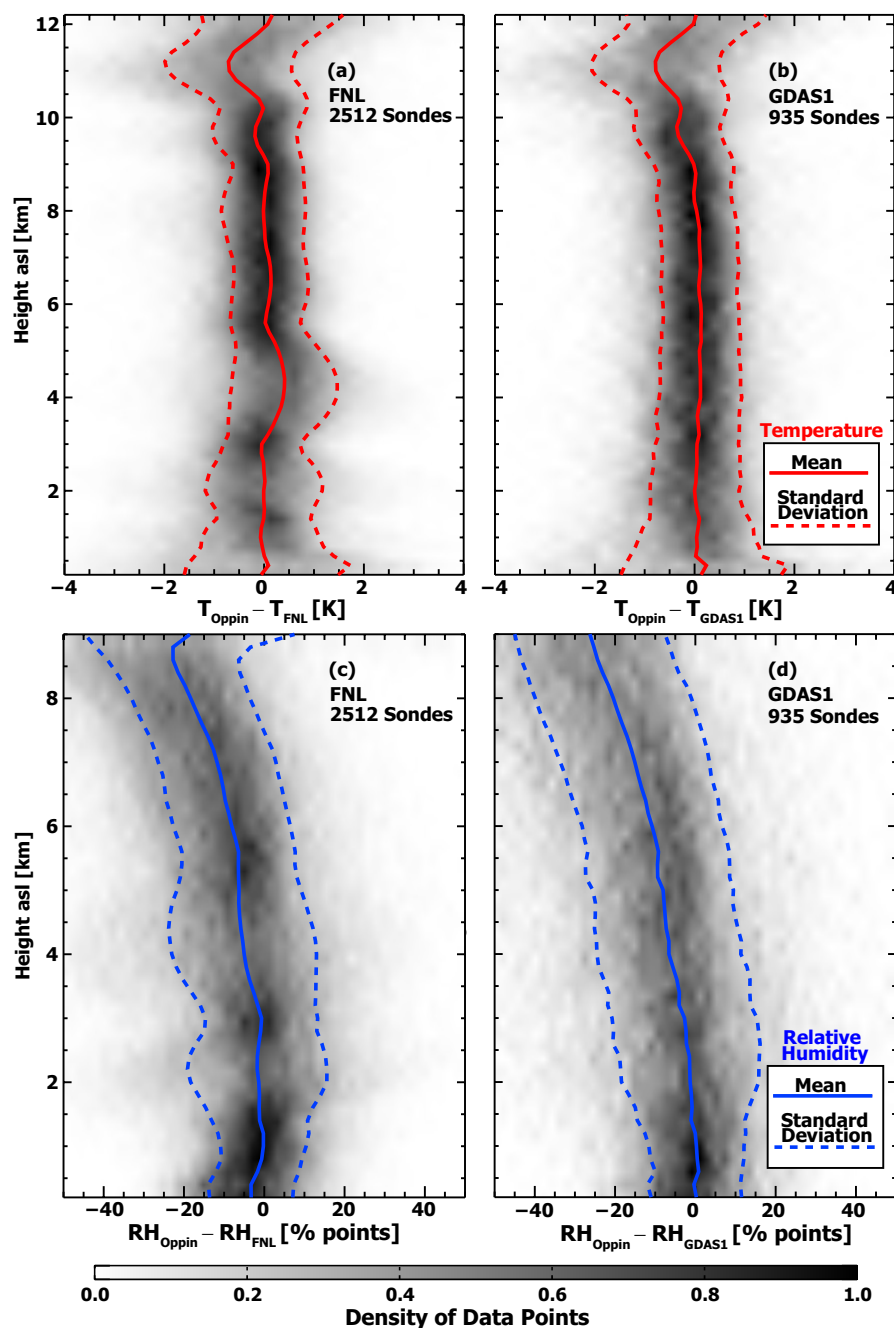


**Figure 5.6:** Difference between radiosonde-derived (Oppin) temperature (a, b, red lines) and relative humidity (c, d, blue lines) and the respective model values. Comparisons are shown separately for FNL data (a, c) and GDAS1 data (b, d). Levels of gray in the background indicate the density of data points. Solid lines indicate the mean difference and dashed lines denote the standard deviation. 2512 (a, c) and 935 (b, d) sonde profiles were compared with respective model-derived temperature and humidity profiles for the grid point Borna (see Fig. 5.5).

2 km height and in the tropopause region above 10 km height. The tropopause region is characterized by a cold bias of the archived data sets on the order of  $-0.7$  K whereas the boundary layer shows an increased variability, i.e. standard deviation, between the Oppin and model soundings. Between 2 and 10 km height the variability is small with standard deviations on the order of 0.7 K. However, the comparison between Oppin and the FNL data set shows another warm bias of the FNL data at heights between 3 and 5.5 km that is on the order of 0.4 K.

The comparison of the differences in relative humidity [Fig. 5.6 (c), (d)] revealed a standard deviation between the model data and the soundings on the order of  $\pm 20$  percentage points. Additionally, an increasing wet bias of the model data with increasing height is visible. At 8 km height, the wet bias reaches values of around 20 percentage points. This bias is in accordance with the well-known fact that the used sondes show a dry bias for temperatures below  $-20$  °C [Vömel *et al.*, 2007].

If the Oppin radiosonde profiles are taken as reference profiles, the error in the retrieval of temperatures from the FNL or GDAS1 data set is of the order of 1 K. Therefore, the archived temperature data provide a good representation of the cloud meteorological properties. The archived humidity data should be handled with care. In the following they will be used as a qualitative indicator for moist layers only.

### 5.3 Aerosol information

A primary goal of the presented study is the investigation of the impact of Saharan dust on cloud glaciation. Therefore, information on the origin of the air mass and the embedded aerosol is required. For this purpose HYSPLIT backward trajectories and DREAM outputs for each cloud case were analyzed [see Fig. 5.1 (blue area)].

#### HYSPLIT backward trajectories

The calculation of the backward trajectories was automatically performed for each cloud case with the offline version of HYSPLIT [Draxler and Hess, 1998; Draxler and Rolph, 2003]. As input meteorological fields for the trajectory calculation the archived model assimilation data sets FNL and GDAS1 were used. In Fig. 5.7 trajectories are shown for the two cloud cases presented in Fig. 5.2. The height of arrival of the trajectories was set to the respective cloud layer mean height.

The offline version of HYSPLIT 4.8 additionally allows one to perform trajectory cluster analyses. In the framework of this study clustering was used to separate trajectories coming from the Saharan region from trajectories of other origin. Clustering of trajectories is a widely used tool for the determination of the dominating source regions and tracks of air masses arriving at a measurement site. In contrast to the approach of associating clusters to seed trajectories [Dorling *et al.*, 1992] the HYSPLIT clustering algorithm is based on the comparison of the spatial variance (SPVAR) between the trajectories that are to be clustered [Draxler *et al.*, 2009].

---

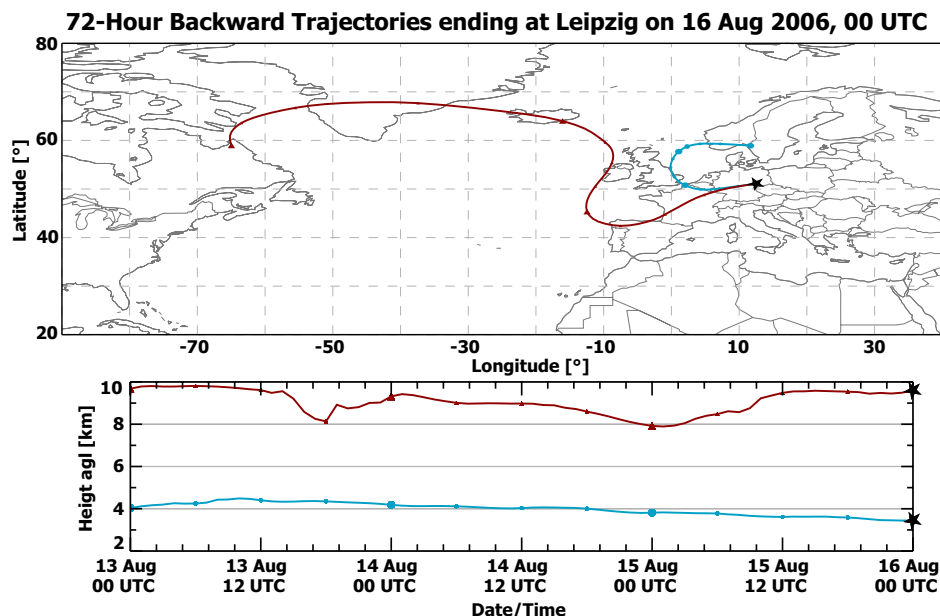


**Figure 5.7:** 72-hour HYSPLIT backward trajectories for the two cloud layers presented in Fig. 5.2. Ending time of the trajectories is 16 August 2006, 00 UTC.

At the beginning of the clustering process every trajectory is defined as a single cluster. In the first step, SPVAR is calculated as the sum of the squared distances between every cluster's endpoints and the according endpoint locations of every other cluster. Subsequently, those clusters are combined for which SPVAR is smallest. For the resulting new cluster the total spatial variance (TSV) is calculated which is the sum of the SPVARs of all trajectories contained in the cluster. During the next steps, those clusters are combined for which the increase in TSV is smallest. This process is repeated until only one cluster is left. With decreasing number of clusters TSV increases. The stronger the increase in TSV the larger is the difference between the trajectories contained in the cluster. Therefore, the minimum number of clusters is constrained by the demand of a linear increase in TSV. If TSV starts to increase non-linearly the difference between the trajectories is too large to allow for the incorporation into one cluster. Studies that are based on the HYSPLIT trajectory calculations are presented in Sections 7.4.1.

### Regional dust model DREAM

Data computed with DREAM [Nickovic *et al.*, 2001] were used to estimate the dust load above Leipzig. DREAM delivers operational dust forecasts for North Africa, the Middle East, and Europe which are verified with observational data on a daily base. It also delivered dust forecasts for the SAMUM field campaigns and has been intensively tested and validated using available observational data [Pérez *et al.*, 2006a,b; Haustein *et al.*, 2009]. The model version that was used for this study calculates dust concentration in  $\mu\text{g m}^{-3}$  at four size bins for diameters of 0.78  $\mu\text{m}$ , 6.1  $\mu\text{m}$ , 18  $\mu\text{m}$ , and 38  $\mu\text{m}$  together with column dust load, wet

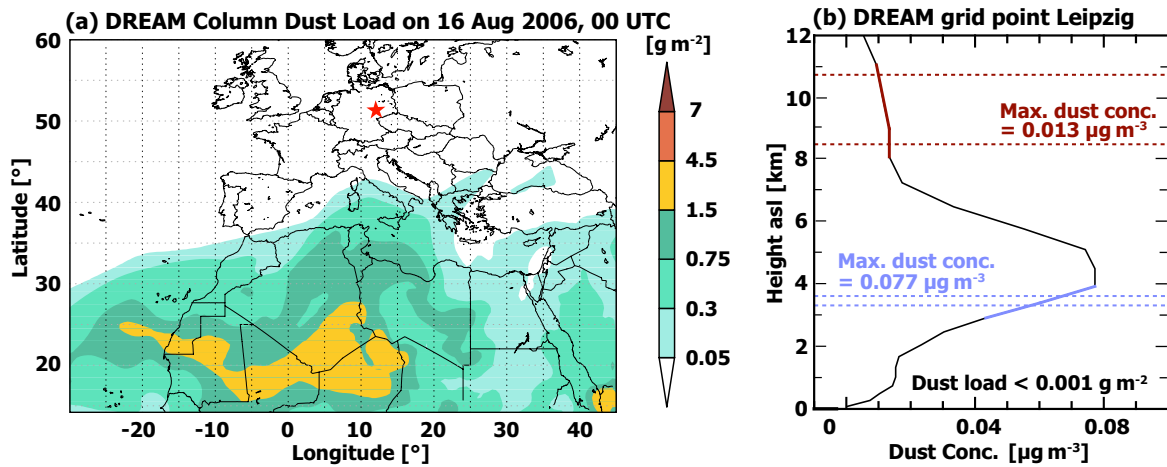


**Figure 5.8:** DREAM calculation of (a) column dust load and (b) dust concentration for grid point Leipzig [red star in (a)] on 16 August 2006, 00 UTC. Elevated dust concentrations occur over the northern Sahara and the Mediterranean. For Leipzig a column dust load of below  $0.001 \text{ g m}^{-2}$  is given and maximum dust concentrations within 500 m of the lower and upper cloud layers identified in Fig. 5.2 are  $0.077 \mu\text{g m}^{-3}$  and  $0.013 \mu\text{g m}^{-3}$ , respectively.

deposition, dry deposition, and surface concentration for 24 height levels between 86 m and 15000 m.

Model results are available for the grid point Leipzig with 12-hour resolution for the entire lidar observation period from 1997–2008. Data from 2007 to 2008 were obtained from the operational model output that is available online<sup>3</sup>. Before 2007, data were taken from a 48-year reanalysis (1958–2006) with  $0.3^{\circ} \times 0.3^{\circ}$  resolution [Pérez *et al.*, 2007]. In this simulation, meteorological fields were initialized every 24 hours and boundary conditions were updated every six hours with the NCEP/NCAR I global reanalysis<sup>4</sup> ( $2.5^{\circ} \times 2.5^{\circ}$  resolution).

The respective profile of dust concentration given in  $\mu\text{g m}^{-3}$  and of the column dust load in  $\text{g m}^{-2}$  obtained from DREAM calculations for grid point Leipzig was assigned to each cloud layer. In Section 7.4.2, values of the column dust load and of the maximum dust concentration within 500 m of the cloud boundaries are used to separate the DRIFT cloud statistics into dust-free and dust-laden cases. The lidar profiles outside the cloud layers were checked for enhanced aerosol backscatter levels as often as possible. The DREAM results were usually found to be in excellent agreement with the lidar observations. Examples are presented in Chapter 6.

Figure 5.8 presents the column dust load and the vertical profile of the dust concentration over Leipzig at 00 UTC on 16 August 2006 that corresponds to the measurement shown in Fig. 5.2 for which the determination of geometrical cloud properties was discussed. Elevated dust concentrations are only indicated for the northern Sahara and the Mediterranean. For the grid point of Leipzig a column dust load of below  $0.001 \text{ g m}^{-2}$  is given which is the lowest

<sup>3</sup>Output data products of operational runs of DREAM are available online at: <http://www.bsc.es/projects/earthscience/DREAM/>

<sup>4</sup>NCAR: National Center for Atmospheric Research; see <http://www.esrl.noaa.gov/psd/> for additional information regarding the data set

output level of DREAM. Maximum values of dust concentration within 500 m of the cloud boundaries found in Fig. 5.2 are  $0.077 \mu\text{g m}^{-3}$  for the lower cloud layer and  $0.013 \mu\text{g m}^{-3}$  for the upper one.

## 5.4 Cloud phase determination

Cloud phase discrimination is the last task of the data analysis procedure according to Fig. 5.1. It is also the most important one. The determination of the phase-state of an observed cloud is based on the depolarization ratio (see Section 4.5). *Liou and Lahore* [1974] found from lidar observations of different types of hydrometeors that backscattering at ice crystals alters the state of polarization of the incident laser light. Water droplets, in turn, were found to sustain the state of polarization when the light is scattered at exactly  $180^\circ$ . The strength of depolarization was found to depend primarily on the deviation of the shape of the scattering particle from a sphere. In general, randomly oriented ice crystals produce volume depolarization ratios on the order of 30–50% and spherical water droplets cause a depolarization of 0% [*Schotland et al.*, 1971; *Sassen*, 2005b]. These findings were generalized later to the application of depolarization measurements for the separation of spherical from non-spherical cloud hydrometeors and aerosol particles [*Sassen*, 2005b; *Freudenthaler et al.*, 2009; *Liu et al.*, 2009; *Tesche et al.*, 2009a].

For the determination of the cloud phase usually the volume depolarization ratio  $\delta^{\text{vol}}$ , introduced in Section 4.5, is calculated. In practice, the cloud phase was determined from the average vertical depolarization profile as well as from the time–height cross section of  $\delta^{\text{vol}}$  of every cloud layer. The mean profiles were determined in the same manner as the average range–corrected 1064-nm signal that was used to determine the cloud geometrical properties (see Section 5.1). When the layer-averaged depolarization ratio is zero, the respective cloud layer is defined as a pure water cloud. When high values of depolarization are determined the cloud layer is categorized as ice-containing. In some cases a more detailed investigation was necessary which is further discussed below.

Examples for the determination of cloud phase are presented in Fig. 5.9 and 5.10. Figure 5.9 shows the volume depolarization for the case study shown in Fig. 5.2 for which the geometrical cloud properties were determined in Section 5.1. The blue and brown frames again enclose the two cloud layers. It can be seen that the lower cloud layer (blue lines) appears dark blue in the height–time cross section of the volume depolarization ratio. In the profile of the average volume depolarization in the right panel the layer depolarization ratio drops to zero. Hence, this cloud layer is categorized as a pure water cloud. In contrast, the upper cloud layer (brown lines) produces strong depolarization. The average depolarization ratio reaches values of up to 0.3. Therefore, this cloud layer is categorized as ice-containing. Fig. 5.10 shows the height–time cross section and the average volume depolarization ratio for the cloud case with undefined cloud top (for which the geometrical cloud properties are shown in Fig. 5.3). Strong depolarization is found in most regions of the cloud. Accordingly, this cloud layer was categorized as ice-containing.

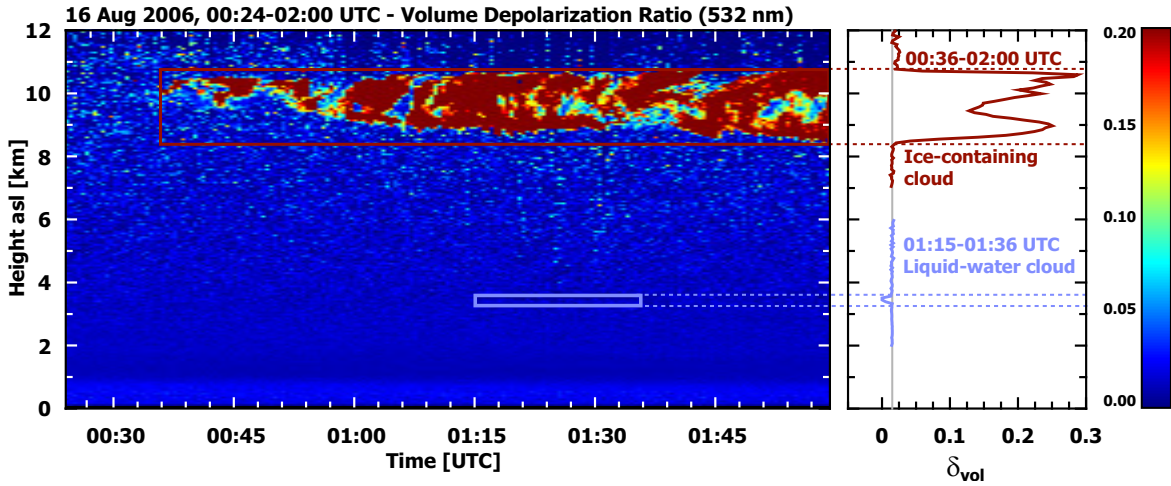


**Figure 5.9:** Example for the identification of cloud phase. Shown are the height–time cross section and the average profile of the 532–nm volume depolarization ratio measured at Leipzig on 16 August 2006. The geometrical cloud properties for the measurement are presented in Fig. 5.2. The lower cloud layer (blue lines) at 3.5 km shows zero depolarization and is therefore categorized as a water cloud. Strong depolarization is produced by the upper cloud (brown lines) at 10 km which thus is categorized as an ice-containing cloud.

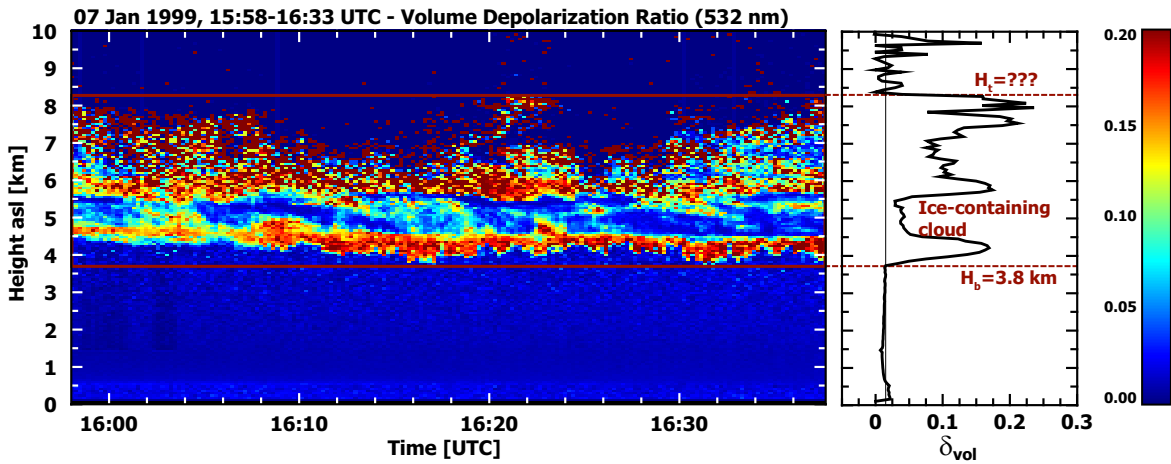


**Figure 5.10:** Example for the identification of the cloud phase of a cloud with undefined cloud top. Shown are the height–time cross section and the average profile of the 532–nm volume depolarization ratio measured at Leipzig on 7 January 1999. The geometrical cloud properties for the measurement are presented in Fig. 5.3. The cloud layer shows significant depolarization and is therefore categorized as an ice-containing cloud.

Besides particle shape two effects may have a significant influence on the determined depolarization:

1. Multiple scattering of light in optically thick water clouds causes additional depolarization that increases monotonically with increasing penetration of the laser pulse into the cloud. This effect is discussed in Section 5.5.
2. Specular reflection introduces a strong bias in the case of a zenith-pointing lidar. Horizontally oriented ice crystals produce strong lidar signals and rather low depolarization ratios which are close to those of water clouds. A detailed description of this effect is presented in Section 5.6.

## 5.5 Multiple scattering

In water clouds with high droplet number concentrations of the order of  $100 \text{ cm}^{-3}$  the probability of forward scattering of laser photons is high [Liou and Schotland, 1971; Wandinger, 1998]. A considerable amount of scattered laser light remains within the receiver field of view (RFOV) of the lidar receiver telescope [Jaquinta et al., 1995; Wandinger, 1998; Bissonnette, 2005] and is backscattered at angles deviating from  $180^\circ$ . The fundamental assumption of the lidar equation [see Eq. (4.1)] is the single-scattering approximation. Accordingly, every emitted photon does only undergo one scattering process which either leads to backscattering or to extinction of the photon. However, when a photon is scattered into the forward direction, which is equivalent to an extinction event, it may remain within the RFOV of the lidar and is still available for subsequent backscattering processes. This process is illustrated in Fig. 5.11. The consequences of multiple scattering for the observed optical cloud properties are twofold:

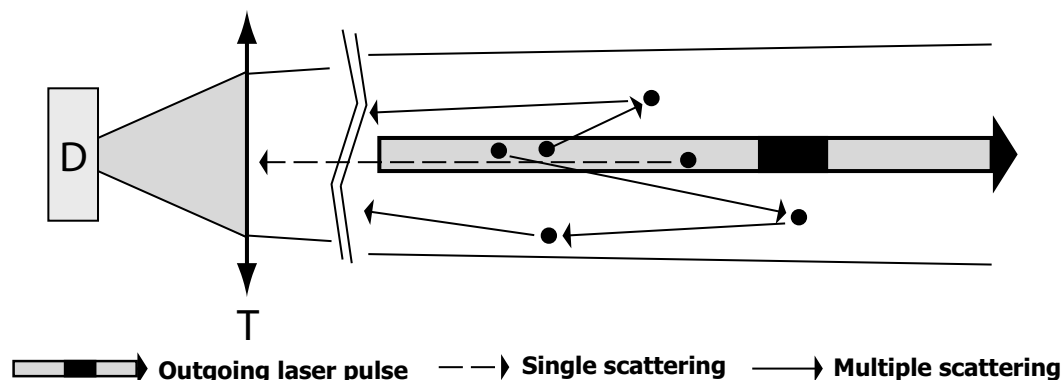


**Figure 5.11:** Illustration of multiple scattering of laser light (solid arrows) and single scattering (dashed arrow) on particles (solid circles). The outer tilted lines indicate the RFOV of the telescope (T). D is the detector. Complete overlap of laser beam and RFOV is assumed. Adapted from Bissonnette [2005]

1. The observed (attenuated) particle backscatter coefficient increases whereas the observed (effective) particle extinction coefficient decreases. Hence, the observed optical depth of the cloud is underestimated and the particle lidar ratio appears smaller than it actually is.
2. Because the lidar detects photons that were backscattered at angles deviating from  $180^\circ$  light is depolarized even in case of scattering from spherical cloud droplets.

The effect described in item 1 does not hinder cloud-phase retrieval. Because, in addition, cloud optical depth and particle lidar ratio are derived for qualitative purposes only in this work the influence of multiple scattering on these parameters is neglected here. Detailed information can be found in *Wandinger* [1998] and *Seifert et al.* [2007].

Item 2 however needs further discussion because multiple scattering affects the depolarization observation in water clouds which can complicate the determination of the cloud-phase. The assumption that scattering by spherical liquid water droplets does not produce depolarization at typical lidar wavelengths is only valid for scattering at  $180^\circ$ . Figure 5.12 presents scattering phase functions and corresponding depolarization ratios at  $\lambda = 532$  nm for two typical gamma distributions of liquid water droplets. Figure 5.12 (a) shows the size distribution of the two model clouds C1 (red curve, [*Deirmendian*, 1969]) and NS1 (black curve, [*Plass and Kattawar*, 1971]) which are representative for a typical cumulus cloud and a nimbostratus cloud, respectively. The corresponding scattering phase functions for the two droplet distributions are shown in Fig. 5.12 (b). The phase functions were calculated based on Mie scattering theory after *Bohren and Huffman* [1983] and *Wandinger* [1994]. Both curves in Fig. 5.12 (b) show the strong forward-scattering peak which increases with increasing droplet diameter and is about two to three orders of magnitude stronger than scattering at any other angle. The calculated relation between depolarization ratio and scattering angle is presented in Fig. 5.12 (c). Only at  $180^\circ$  backscattering the depolarization ratio is zero for both clouds. Within  $2^\circ$  from  $180^\circ$  the depolarization ratio increases up to 0.8. Photons that reach the lidar receiver after several forward scattering events and one non- $180^\circ$  scattering process increase the measured depolarization ratio. With increasing laser pulse penetration depth into the cloud, the number of forward scattering events increases and thus the distribution of backscatter angles of the received photons broadens. This leads to a monotonic increase of the depolarization ratio from cloud base towards cloud top.

Besides the microphysical properties of the scattering medium the magnitude of the increase of depolarization caused by multiple scattering depends on the RFOV of the lidar and the distance between the scattering medium and the lidar. Both parameters affect the volume that is available for multiple scattering to take place. The RFOV of MARTHA is 0.4 mrad. Compared to other systems described in literature, this is a rather narrow field of view. *Sassen and Petrilla* [1986] presented measurements of multiple-scattering-induced depolarization in low marine stratus clouds and found peak depolarization values between 0.05 and 0.1 for a RFOV of 1.0 mrad, increasing to 0.15–0.3 for a RFOV of 3.0 mrad. *Ansmann et al.* [2009] reported multiple-scattering-induced depolarization ratios in mid-tropospheric altocumulus clouds of up to 0.15–0.2 for a lidar system with a RFOV of 0.8 mrad.

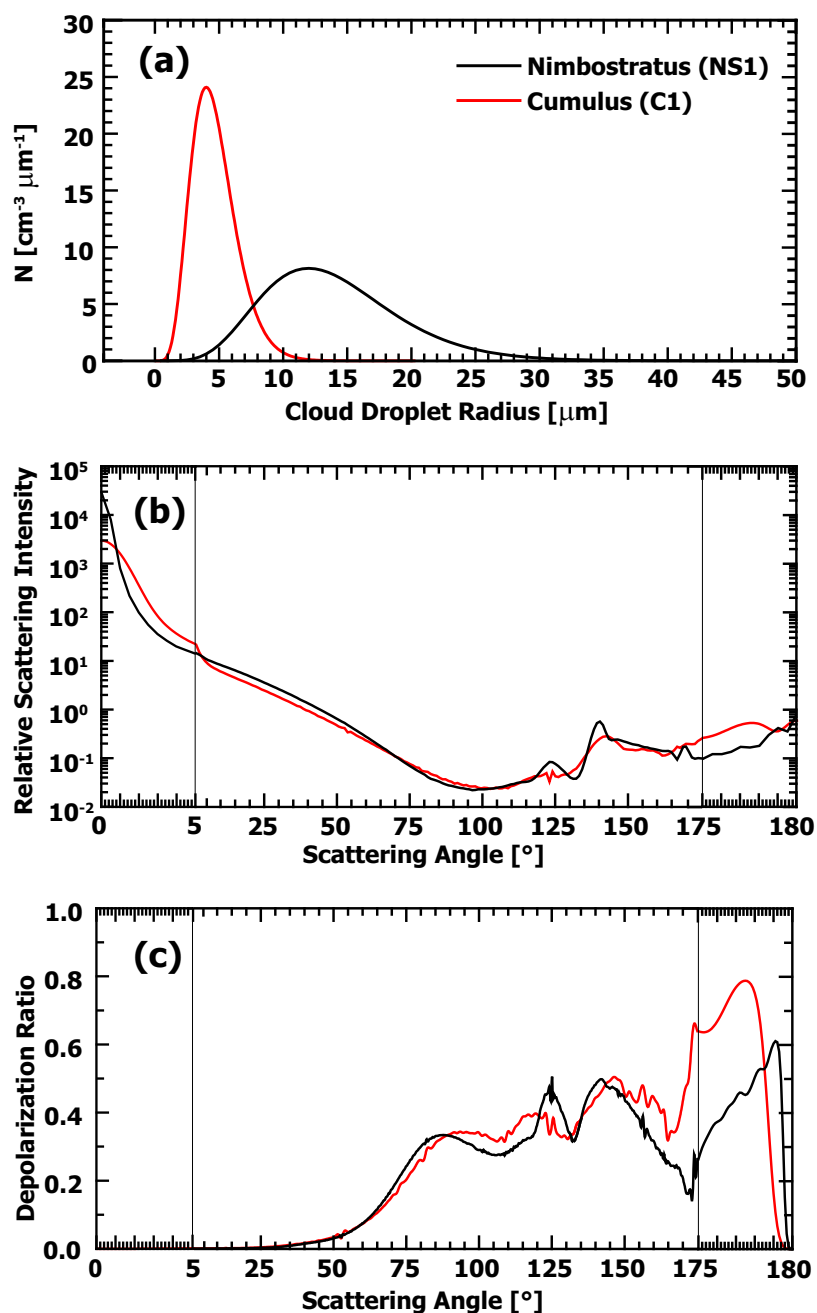


**Figure 5.12:** Effect of liquid–water droplets on the scattering phase function and the angular distribution of the depolarization ratio for two cloud droplet distributions. (a) cloud droplet distribution of a cumulus cloud (C1, red curve, [Deirmendian, 1969]) and a nimbostratus cloud (NS1, black curve, [Plass and Kattawar, 1971]), (b) scattering phase function, and (c) depolarization ratio. Only for  $180^\circ$  backscattering the depolarization ratio is zero. For small deviations of the scattering angle from  $180^\circ$ , as it is the case for multiple scattering, the depolarization ratio increases up to 0.8. The phase functions and the depolarization ratio were calculated after Bohren and Huffman [1983] and Wandinger [1998].

Hence, the magnitude of multiple-scattering-induced depolarization for measurements with MARTHA can be expected to be considerably lower than the 0.8-mrad and 1.0-mrad values presented in *Ansmann et al.* [2009] and *Sassen and Petrilla* [1986], respectively.

Figure 5.13 shows a measurement example from 18 July 2007, 00:54–02:10 UTC. Four water clouds can be identified from the panel of the range-corrected signal and the corresponding height-time cross section of the volume depolarization ratio. The cloud top temperature of the coldest cloud was  $-7^\circ\text{C}$  which is indicated by the horizontal line. Three of the clouds were optically and vertically thin and did not show any enhanced depolarization, even at cloud top. Multiple scattering therefore played only a minor role in these clouds. An apparently more dense water cloud that occurred towards the end of the measurement showed indications of the influence of multiple scattering. The cloud is enclosed by white rectangles in the height-time cross sections of the range-corrected signal and the volume depolarization ratio. From the average signals of this time period vertical profiles

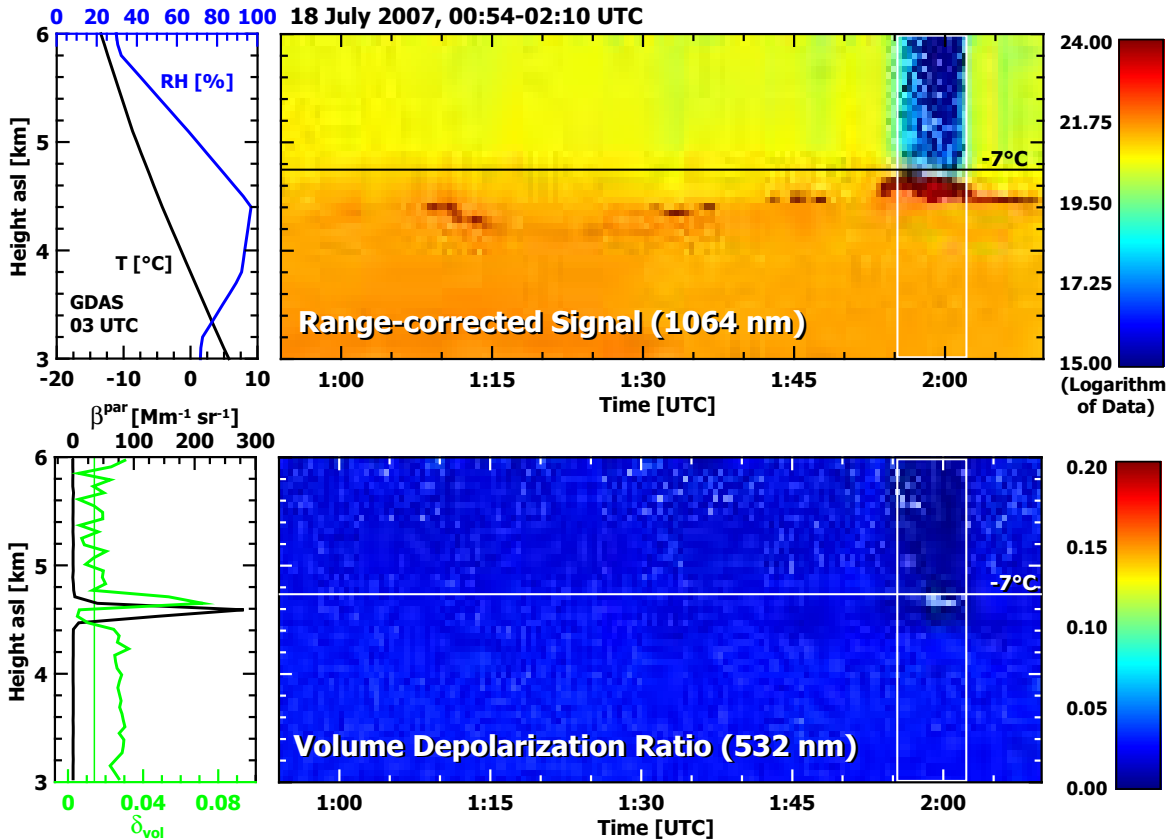


**Figure 5.13:** Observation of four water clouds between 4 and 5 km height on 18 July 2007. Range-corrected 1064-nm signal (top, arbitrary units) and volume depolarization ratio at 532 nm (bottom) are shown with vertical resolution of 60 m and temporal resolution of 30 s. Left panels show height profiles of the simulated GDAS temperature and humidity profiles for grid point Leipzig at 03 UTC (upper panel), particle backscatter coefficient  $\beta^{\text{par}}$  and volume depolarization ratio  $\delta_{\text{vol}}$  (lower panel, temporal average for the time period indicated by the white frame). Temperature levels (horizontal lines) are taken from the temperature profile.

of Raman particle backscatter coefficient and volume depolarization ratio were calculated which are shown in the lower left panel of Fig. 5.13. Because the average signal above the cloud was too noisy the calibration coefficients that are needed for the calculation of the particle backscatter coefficient (see Section 4.3.2) and the volume depolarization ratio (see Section 4.5.2) were determined from the average signal for the period from 01:00 to 01:45 before they were applied to the short period of cloud occurrence. The cloud base is indicated by a sudden increase of the particle backscatter coefficient at about 4.2 km height. Below that height, the volume depolarization ratio showed values that were slightly above the molecular depolarization ratio of 0.014. This region obviously contained some weakly depolarizing aerosol particles. At cloud base the depolarization ratio decreases towards zero. This indicates the presence of liquid water droplets. Caused by the strong extinction within the cloud the number of multiply-scattered photons increases with increasing cloud depth. As described above, multiple scattering is accompanied by scattering at angles unequal to  $180^\circ$ . These deviations from true backscattering introduce significant depolarization to the multiply-scattered photons. The increase in the number of multiply-scattered photons in conjunction with the decreasing amount of single-scattered photons cause the increase of the volume depolarization ratio at heights above 4.6 km. Above the cloud top at around 4.7 km the volume depolarization ratio decreases towards the molecular background value of 0.014.

Multiple-scattering-induced depolarization in water clouds was a rarely observed phenomenon during the analysis of the entire 11-year data set, even though it might be a severe problem for lidar systems with a larger RFOV. It occurred more frequently during measurements with the old setup of the beam separation unit of MARTHA that was applied between 1997 and March 2001. As a consequence of the study of multiple-scattering-induced depolarization a cloud was also classified as a water cloud if its profile of the depolarization ratio was zero at cloud base and increased monotonically towards a maximum value at cloud top.

## 5.6 Specular reflection

Specular reflection is a serious problem when studying mixed-phase clouds with a zenith-pointing lidar. Therefore, well-defined experiments were performed to study specular reflection in detail. The goal was to obtain a clear understanding of the influence of specular reflection on scattering properties of clouds and to be able to unambiguously identify clouds containing ice. The experiments are described in the following subsections.

When a zenith-pointing lidar is applied to studies of mixed-phase and ice clouds, light backscattering at the planar planes of horizontally oriented ice crystals can introduce a large bias in the depolarization measurement. In the case of so-called specular reflection the determined backscatter coefficients are rather high and the extinction-to-backscatter ratios (lidar ratios) and depolarization ratios are rather low. The depolarization ratio is close to the one of liquid water drops. Therefore, in cloud parcels that contain horizontally oriented ice crystals the measured depolarization ratio cannot be used to unambiguously discriminate between liquid water and ice.

---

The ability of ice crystals to align horizontally depends primarily on their shape and size. If crystals are small their movement is driven by Brownian turbulent motion [Hallett *et al.*, 2002], inhibiting any alignment. To determine the preferred size for an alignment, Sassen [1980] studied man-made light pillars<sup>5</sup> which are produced by horizontally aligned crystals. The investigation revealed that crystal diameters larger than 100–200  $\mu\text{m}$  are needed in the case of plate-like and dendritic crystals to align horizontally during falling.

The observation of specular reflection with lidar was first suspected by Platt [1977] who measured anomalous relations between depolarization ratio and backscatter intensity in some parts of a cloud layer. Experimental prove of the occurrence of specular reflection in ice and mixed-phase clouds in terms of a single-cloud case study was presented in Platt *et al.* [1978] who showed elevation scans of lidar backscatter and depolarization ratio for zenith angles between  $0^\circ$  and  $8.2^\circ$ . The decrease of the retrieved backscatter coefficient accompanied by an increase of the observed depolarization ratio with increasing zenith angle identified the regions in the observed cloud that contained horizontally oriented ice crystals. Because an organized alignment of crystals is only possible in the horizontal plane all other angles of orientation are distributed randomly. Therefore, populations of horizontally aligned ice crystals can be identified by a strong drop of the intensity of the lidar signal when the beam is tilted from the zenith to a sufficiently large zenith angle. Further studies gave indication that specular reflection is not an equally distributed phenomenon in mixed-phase and ice clouds. The occurrence of horizontally aligned crystals appears to be a function of temperature and probably of the location in the cloud. Based on three years of cirrus observations Thomas *et al.* [1990] reported in agreement with the above-mentioned studies of Platt that the preferred temperature range for the occurrence of specular reflection appears to be between  $-8$  and  $-25$   $^\circ\text{C}$ . At these temperatures, the formation of regular plate-like crystals, which provide most suitable conditions for horizontal orientation, dominates [Magono and Lee, 1966]. From these observations and the findings of Sassen [1980] it can be suspected that cloud-boundary regions should provide less preferable conditions for specular reflection. Usually crystals sublimate or melt near the cloud base because temperatures rise or humidity decreases. Sublimation causes the crystals to shrink until their size is too small to allow for horizontal alignment. If temperatures are close to the melting point the crystals either shrink or they form irregular agglomerates which also decreases the ability of the crystals to align horizontally. A similar notion was recently communicated in a study of Westbrook *et al.* [2009]. Therefore, it should be expected that the impact of specular reflection is low at cloud base. This effect should allow to identify an ice cloud even though all of its remaining parts show strong specular reflection.

Because a clear discrimination of water and ice-containing clouds is a fundamental requirement of this study the nature of specular reflection was investigated in detail by combined observations with a scanning lidar, an off-zenith pointing lidar, and the zenith-pointing lidar MARTHA. The goal was to prove the hypothesis that even in the case of strong

---

<sup>5</sup>Light pillars: Vertical columns of light above a light source resulting from specular reflection at horizontally aligned ice crystals during light snowfall or ice fog events.

---

specular–reflection effects there are always still regions in the cloud that produce sufficient depolarization to identify the cloud phase when using a zenith–pointing lidar.

The instruments that were used for the studies are introduced in Subsection 5.6.1. Subsection 5.6.2 presents results of the angular dependence of the strength of signals returned by specular reflection and the investigation of the connection between meteorological conditions and the intensity of specular reflection. Subsection 5.6.3 points out how horizontally oriented ice crystals can influence regular observations of optical properties and phase state of cirrus clouds and mixed–phase clouds. In Subsection 5.7 is discussed how ice–containing clouds can be distinguished from water clouds with MARTHA data only.

### 5.6.1 Instrumentation

The data products discussed in the following sections are based on dedicated observations performed with three different lidar instruments developed and maintained by IfT. Their properties are listed in Table 5.1. The zenith–pointing lidar MARTHA (see Section 4.1) measures signals with a vertical resolution of 60 m and a temporal resolution of 30 s. It provides profiles of volume depolarization ratio, particle backscatter coefficient, and particle extinction coefficient at 532 nm which are affected by specular reflection. The high–precision scanning ability of the 2.022– $\mu\text{m}$  Doppler Wind Lidar (WiLi) [Engelmann *et al.*, 2008; Engelmann, 2009] was used to perform elevation scans that yield return signals of clouds at distinct angular steps of 0.2° to 0.5° between the zenith and up to 5° off–zenith. WiLi signals have a range resolution of 75 m and a temporal resolution of at least 1 to 5 s. Data of volume depolarization ratio at 355 nm and particle backscatter coefficient and particle extinction coefficient at 532 nm at a fixed zenith angle of 5° with a primary range resolution of 30 m and a temporal resolution of 30 s are provided by the automatic, portable three–wavelength Raman polarization lidar Polly<sup>XT</sup> [Althausen *et al.*, 2009]. The arrangement of the three instruments on the area of IfT is illustrated in Fig. 5.14. Distances of less than 5 m between the individual instruments assured that all instruments probed nearly the same volume of air. However, due to the different pointing angles of the three instruments the horizontal distance between the probed volumes increased with increasing height. For a zenith angle of 5° and an altitude of 5000 m the horizontal distance between the probed volumes is approximately 440 m. Therefore, the scanning direction of WiLi was always adjusted in such

**Table 5.1:** Instruments used for the characterization of specular reflection. Listed are the wavelength of operation  $\lambda$  [nm], range resolution  $\Delta R$  [m], time resolution  $\Delta t$  [s] and pointing angle in degrees off the zenith. Depolarization ( $\delta$ ) and backscatter coefficient ( $\beta$ ) from Polly<sup>XT</sup> were measured at different wavelengths.

Instrument	$\lambda$ [nm]	$\Delta R$ [m]	$\Delta t$ [s]	Zenith Angle [°]
MARTHA	532	60	30	0
WiLi	2022	75	1 ... 5	–5 ... 5
Polly <sup>XT</sup>	355( $\delta$ ), 532( $\beta$ )	30	30	5



**Figure 5.14:** Position of the instruments that were used for the characterization of specular reflection (M: MARTHA, P: Polly<sup>XT</sup>, W: WiLi) on the area of IfT.

a way that it measured parallel to the wind direction in the altitude range of interest. This approach assured that the same cloud volume crossed MARTHA and WiLi.

To characterize the influence of specular reflection on the received lidar signal the Doppler lidar WiLi performed elevation–scan measurements. Table 5.2 lists all elevation–scan measurements that were performed at Leipzig together with information about the observed clouds. During 80% of the total measurement time of approximately 22 hours clouds were observed at heights between 3 and 11 km. That corresponds to a temperature range between  $-5$  and  $-58$  °C. The cloud types listed in Table 5.2 were determined from the observed features in the lidar signal as well as from observations made by eye during the measurements at IfT.

**Table 5.2:** Scan measurements performed with WiLi to study the angular dependence of specular reflection.

Date	Time (UTC)	Height Range (km)	Temperature Range (°C)	Angular Range (°)	Cloud Type
09 Oct 2006	1315 – 1853	5.0 ... 11.	$-56$ ... $-13$	$-5$ ... $5$	Ci, Cs, Ac vir
10 Oct 2006	1027 – 1816	6.5 ... 11.	$-58$ ... $-20$	$-2$ ... $2$	Ci, Cs
16 Jan 2007	1117 – 1300	3.0 ... 10.	$-55$ ... $-5$	$-3$ ... $3$	Ci, Cs, Ac vir, Sc
06 Feb 2007	1028 – 1408	5.5 ... 8.5	$-56$ ... $-35$	$-3$ ... $3$	Ci
21 Feb 2007	1224 – 1519	8.5 ... 9.0	$-50$ ... $-42$	$-3$ ... $3$	Ci

### 5.6.2 WiLi and MARTHA observations

Even though the impact of specular reflection is strongest for lidar measurements performed at zenith angles of exactly  $0^\circ$  it is also observed at small off-zenith angles. Lee-eddy effects produced during falling cause the horizontally oriented planar ice crystals to flutter like falling leaves [Platt *et al.*, 1978; Thomas *et al.*, 1990; Hallett *et al.*, 2002]. Hence, lidar measurements performed at zenith angles between  $0^\circ$  and slight deviations from this position can still suffer from the effect of specular reflection. The response of detected signal strength and depolarization ratio to different zenith angles is illustrated in Fig. 5.15 which shows an idealized cloud with three different layers A, B, and C. Whereas layers A and C contain randomly oriented ice crystals only, layer B also contains horizontally aligned planar crystals. This cloud is scanned with lidar at three different zenith angles deviating from  $0^\circ$  (red) [ $0.2^\circ$  (orange),  $1^\circ$  (green) and  $2^\circ$  (blue)]. Figure 5.15 (b) shows the signal strength for the different zenith angles. At  $0^\circ$  the signal reaches a peak value in the specular-reflecting layer. With increasing zenith angle the signal approaches values that are similar to those derived from the layers that contain the randomly oriented crystals only. The opposite is the case for the measured depolarization ratio which is shown in Fig. 5.15 (c). At  $0^\circ$  (zenith-pointing) the depolarization ratio is close to zero. With increasing pointing angle, the depolarization ratio increases and is finally similar to the ones for layers A and C.

When the scan sequence shown in Fig. 5.15 (a) is continuously performed over a long time period a picture similar to the one shown in Fig. 5.16 is observed. Following the scheme in Fig. 5.15, the illustration shows the temporal development of the detected signal in the case of randomly oriented crystals (black bars, layers A and C in Fig. 5.15) and of predominantly horizontally aligned crystals (red bars, layer B in Fig. 5.15). Thus, when specular reflection occurs, the time-height display of the detected signal of a scanning lidar

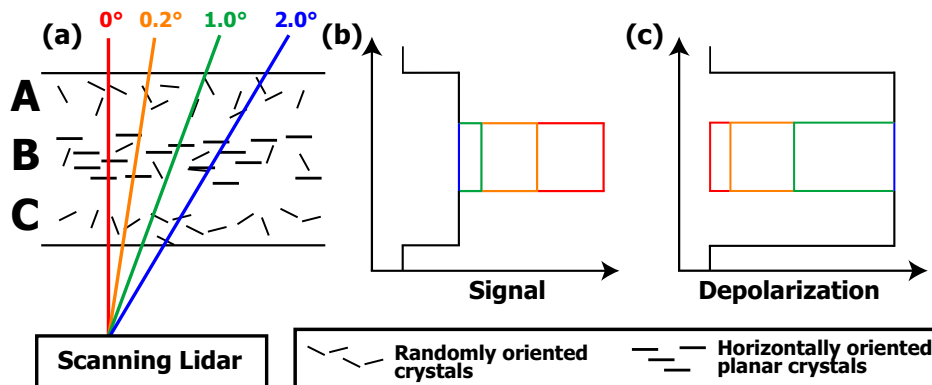


**Figure 5.15:** Sketch illustrating the impact of a cloud that contains layers of randomly oriented (A, C) and horizontally aligned, specular reflecting ice crystals (B) on observations with a scanning lidar pointing to zenith angles of  $0^\circ$  (red),  $0.2^\circ$  (orange),  $1^\circ$  (green) and  $2^\circ$  (blue) (a). (b) and (c) show measured signal strength and depolarization, respectively, for the four different zenith angles. With increasing zenith angle the observed signal decreases and the depolarization ratio increases. Finally both quantities reach the values for the layers A and C which contain randomly oriented crystals only.

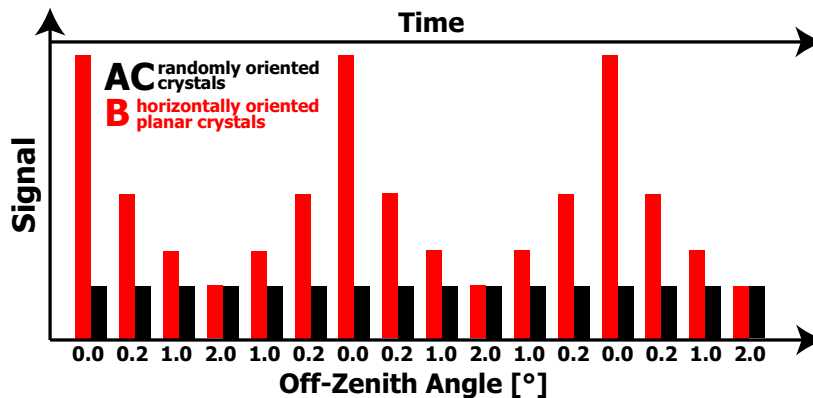


**Figure 5.16:** Signal time series obtained with a continuously scanning lidar (from  $0^\circ$  to  $2^\circ$  and back) in the case of horizontally aligned crystals (red, layer B in Fig. 5.15) and randomly oriented crystals (black, layers A and C in Fig. 5.15). An oscillation of signal strength with peaks at  $0^\circ$  is observed in the presence of aligned ice crystals while observations in layers with randomly oriented crystals show constant signal strength.

should show a striped pattern whereas it should be undisturbed in the case of randomly oriented scatterers.

Exactly the signal patterns described above are found in many of the WiLi observations. One case is presented in Fig. 5.17. Shown are the height–time cross sections of received range–corrected signal at 1064 nm (a) and volume depolarization ratio at 532 nm (b) derived from MARTHA observations as well as the detected signal–to–noise ratio (c) and line–of–sight (LOS) velocity (d) from the scanning WiLi measurements on 16 January 2007. The scan pattern of WiLi was set to measurements in 5–s intervals at zenith angles between  $-3$  and  $3^\circ$  in steps of  $0.5^\circ$ . The range–corrected signal panel (a) shows that numerous clouds were observed between heights of 1.6 and 8 km. Radiosonde data show that the levels of  $0^\circ\text{C}$  and  $-40^\circ\text{C}$  were reached at 1.9 km and 8 km height, respectively. Thus, the coexistence of ice and water layers was possible for all clouds observed during the measurement, except for the lowest ones. The low volume depolarization ratio [blue in Fig. 5.17 (b)] suggests that the clouds between 2 and 6 km height consisted in part of layers with liquid water droplets. These clouds would be classified as mixed–phase clouds. However, the scan measurement performed with WiLi shows strong scan–angle–dependent variations of the returned signal strength [Fig. 5.17 (c)] in almost all clouds between 2 and 6 km. The decrease of the received signal with increasing zenith angle is expressed by the striped pattern (zebra pattern) in the time–height cross section of the scan measurement. As illustrated in Fig. 5.16 this pattern is caused by strong specular reflection produced by horizontally oriented planar ice crystals. With increasing zenith angle the signal decreases rapidly. Thus, the low volume depolarization ratios observed with MARTHA were caused by specular reflection and not by backscattering from water droplets. On the other hand, high volume depolarization ratios were found where no zebra pattern was observed, as at the lower boundary of the cloud between 4 and 6 km height. Here, the falling crystals were obviously small and randomly oriented [Sassen, 1980; Hallett *et al.*, 2002]. This feature of weakly to strongly enhanced

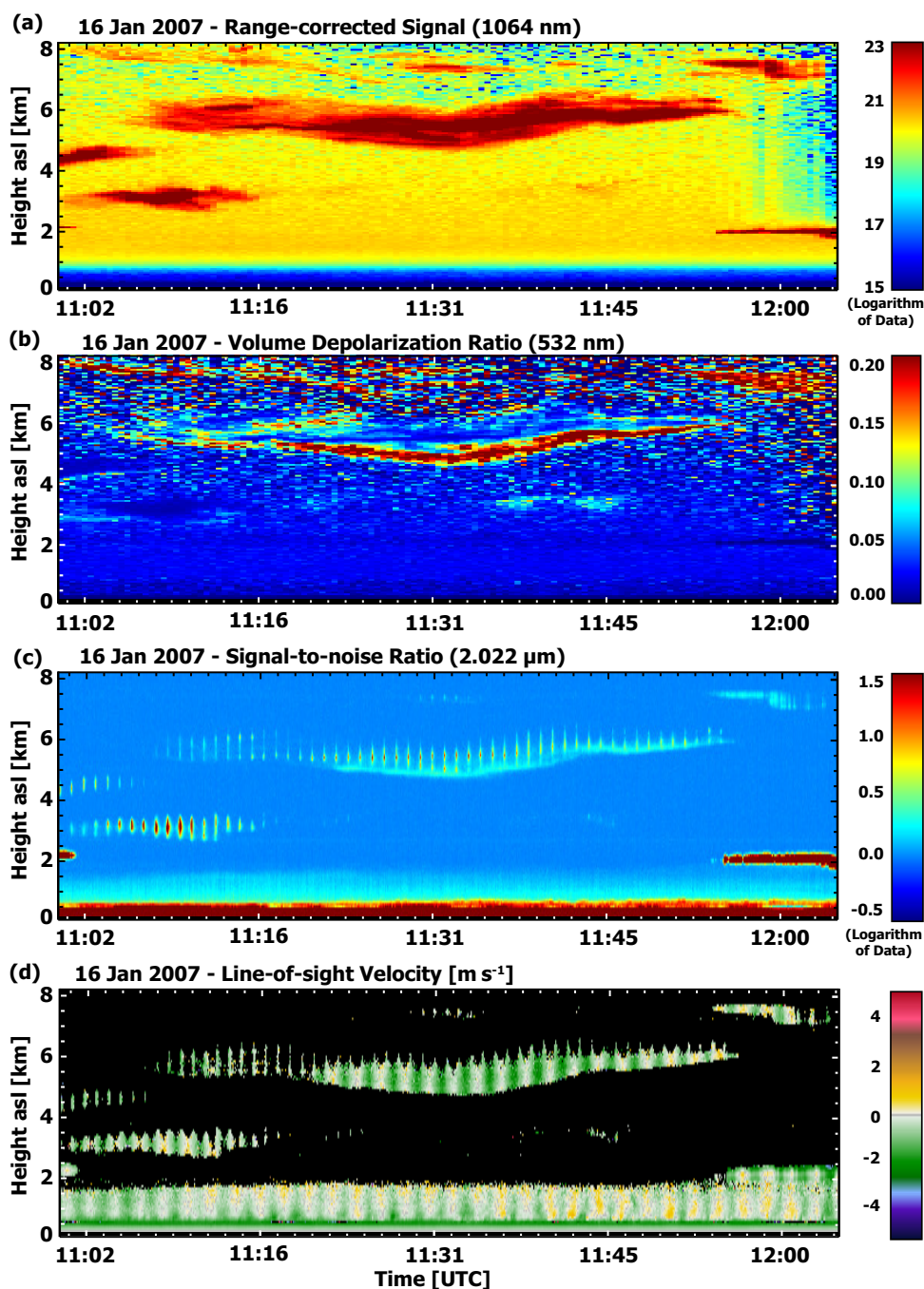


**Figure 5.17:** Height–time cross sections of range–corrected signal (a) and volume depolarization ratio (b) observed with MARTHA and signal–to–noise ratio (c) and line–of–sight (LOS) velocity (d) measured with WiLi scanning between zenith angles of  $-3^\circ$  and  $3^\circ$  at Leipzig on 16 January 2007. The zebra–striped pattern in (c) indicates regions with horizontally aligned crystals producing specular reflection. The measured LOS velocity (d) varies between about  $-2 \text{ m s}^{-1}$  (when the lidar is pointing upwind) and  $+2 \text{ m s}^{-1}$  (when the lidar is pointing downwind). At  $0^\circ$ , only the vertical wind component in combination with the fall speed of crystals is observed by WiLi.

depolarization at cloud base is observed in all clouds that show the zebra pattern. It may thus be used to identify ice-containing cloud layers.

The observation of pure water clouds is documented at 2 km height during the first two and last 10 minutes of the measurement. The water layers show low depolarization [Fig. 5.17 (b)], and indications for horizontally oriented crystals are not observed [see Fig. 5.17 (c)].

As an additional effort, the dependence of WiLi signal-to-noise strength on the scan angle was analyzed. In this task, the signal-to-noise ratio (in the following referred to as signal) for zenith angles of  $0^\circ$  was set to 1. Only in-cloud data were used for the study. Figure 5.18 shows the distribution of the normalized signal in dependence of the zenith angle for 2176 complete elevation scans of WiLi, i.e., high-quality signals were available for all scan angle positions. Data of the measurements listed in Table 5.2 were used.

In Fig. 5.18 (a) all analyzed scans are in the first signal interval (0.9–1) because signals were normalized to the  $0^\circ$ -measurement. Figures 5.18 (b–f) then show a decreasing normalized signal strength (compared to the  $0^\circ$ -signal) indicating a decreasing impact of specular reflection with increasing zenith angle. The distribution of signals flattens and in Fig. 5.18 (f) all normalized signals have almost the same frequency of occurrence. At a zenith angle of  $4^\circ$  the effect of specular reflection does no longer play a pronounced role as it is still the case for, e.g.,  $1^\circ$  and  $2^\circ$ . From the discussion of Fig. 5.18 it can be concluded that specular reflection affects a considerable amount of observed cloud layers. In 70% of all WiLi scans the normalized signal was below 0.8 at  $4^\circ$  zenith angle. A constant signal between  $0^\circ$  and  $4^\circ$  zenith angle (normalized signal larger than 0.9) was observed only in 10% of all scans [see Fig. 5.18 (f)].

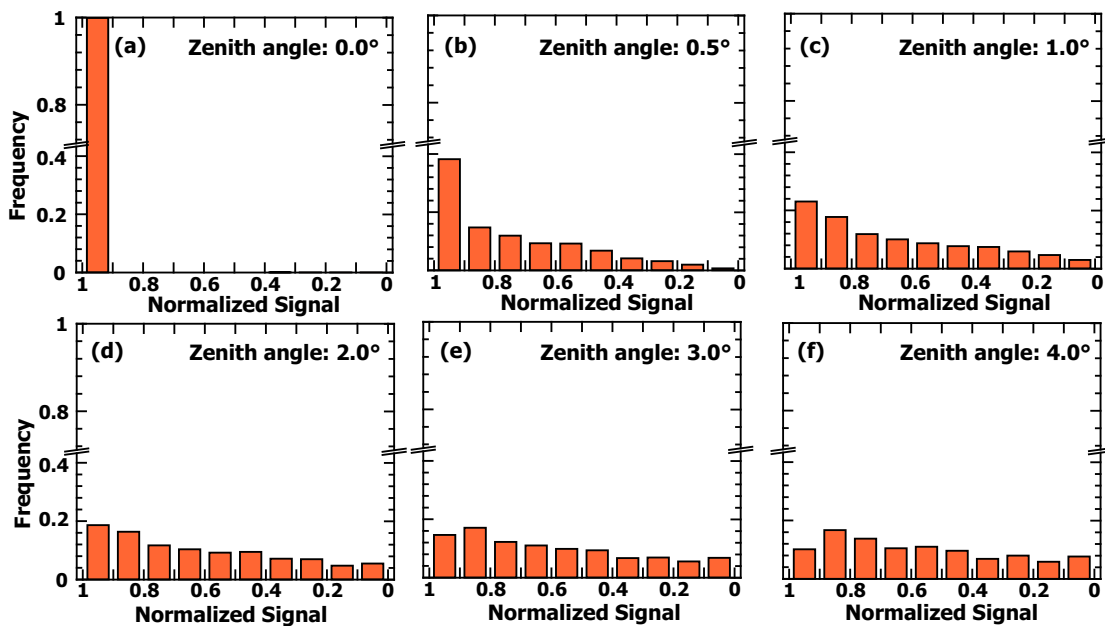


**Figure 5.18:** Frequency of normalized signal strengths for different zenith angles. Mean distributions of normalized signals are based on 2176 WiLi scans. Individual scans were normalized to the  $0^\circ$  measurement.

According to *in situ* observations of ice crystal microphysical properties [McFarquhar and Heymsfield, 1997] that showed correlations between temperature and crystal shape and size, it could be expected that also specular reflection is related to temperature and to the location of ice crystals within a cloud. Figure 5.19 corroborates this hypothesis. For this figure, 12655 pairs of signals measured at  $0^\circ$  and  $2^\circ$  were analyzed. The temperature for each signal pair was determined as described in Section 5.2. Again, signals for  $+2^\circ$  and  $-2^\circ$  were normalized to the  $0^\circ$ -measurement and thus assumed values from 0–1. A normalized mean signal close to 1 means that signals at  $0^\circ$  and at  $2^\circ$  barely deviate from each other. Specular reflection, which would cause strong backscatter at  $0^\circ$  zenith angle, is absent in that case. This behavior is illustrated by the black columns in Fig. 5.16. Figure 5.19 shows a weak influence of specular reflection for the temperature interval from  $-60$  to  $-70^\circ\text{C}$  where the normalized signal at  $2^\circ$  is 0.96. With increasing temperature the mean normalized signal decreases considerably to values of as low as 0.55 indicating an increasing influence of specular reflection to the measured signals. The effect of specular reflection seems to reach its maximum at temperatures between  $-10$  and  $-20^\circ\text{C}$ . As described in the introduction to this section, the same behavior was found in earlier studies of Platt [1977]; Platt *et al.* [1978], Thomas *et al.* [1990], and Westbrook *et al.* [2009]. Below  $-40^\circ\text{C}$  mean ice crystal size is small and the probability for horizontally aligned ensembles of ice crystals is low. However, for the temperature range of interest from 0 to  $-36^\circ\text{C}$  where heterogeneous ice nucleation occurs specular reflection may have a considerable impact.

As described above, the main motivation for the scan measurements with WiLi was to confirm the assumption that the effect of specular reflection decreases at cloud base. Indications which corroborate this assumption were already discussed in the case study presented in Fig. 5.17. In order to find statistical proof for this behavior the signal drop from  $0^\circ$  to  $2^\circ$  zenith angle was analyzed in dependence of cloud depth. Again, all measurements listed in Table 5.2 were used for this analysis. Table 5.3 lists the average normalized signal

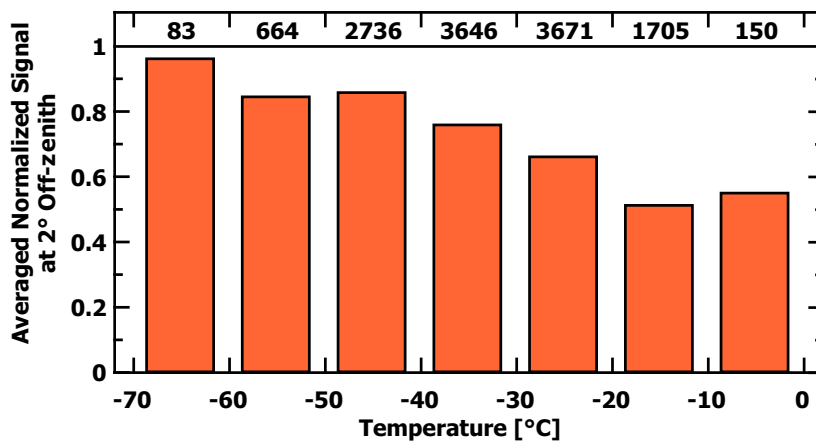


**Figure 5.19:** Mean value of the normalized signal for  $2^\circ$  zenith angle (normalized to the  $0^\circ$ -signal) for seven temperature intervals. The statistics is based on 12655 signal pairs measured at  $0^\circ$  and  $2^\circ$ . The numbers at the top of the graph denote the number of observations.

**Table 5.3:** Average normalized signal and standard deviation at  $2^\circ$  off-zenith for four intervals of cloud penetration depth.

Cloud Penetration Depth (m)	0 – 150	150 – 375	375 – 750	750 – 2250
Cloud Penetration Depth (Bins)	1 – 2	3 – 5	6 – 10	11 – 30
Number of Scans	1066	2058	3015	6071
Mean Normalized Signal at $2^\circ$	0.92	0.76	0.65	0.70
Standard Deviation	0.16	0.28	0.32	0.33

for four different vertical regions of the observed clouds. When only signal pairs from the lowermost 150 m of the cloud are considered, the mean normalized signal is  $0.92 \pm 0.16$ . This value is close to the signal strength of 1 found for the zenith-pointing direction. Therefore, in the cloud base region the effect of specular reflection and thus the occurrence of horizontally aligned crystals is rather small. With increasing penetration depth the  $2^\circ$ -signal decreases to values of around  $0.7 \pm 0.3$ , indicating the increasing impact of specular reflection on the detected signals.

### 5.6.3 Polly<sup>XT</sup> and MARTHA observations

Section 5.6.2 presented the results of an analysis of numerous WiLi elevation scan measurements. In this subsection examples are shown to illustrate how the optical cloud properties, i.e., volume depolarization ratio and particle backscatter coefficient, are affected by the presence of horizontally oriented ice crystals in the cloud layers. Two lidars, one pointing to the zenith (MARTHA) and another one pointing at  $5^\circ$  zenith angle (Polly<sup>XT</sup>) were run simultaneously during these experiments at IFT.

First, Fig. 5.20 schematically illustrates the expected response of particle backscatter

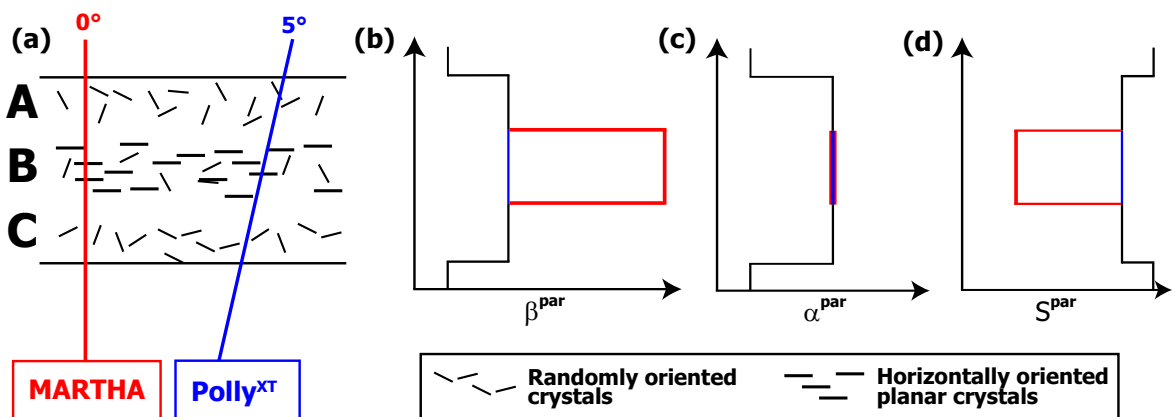


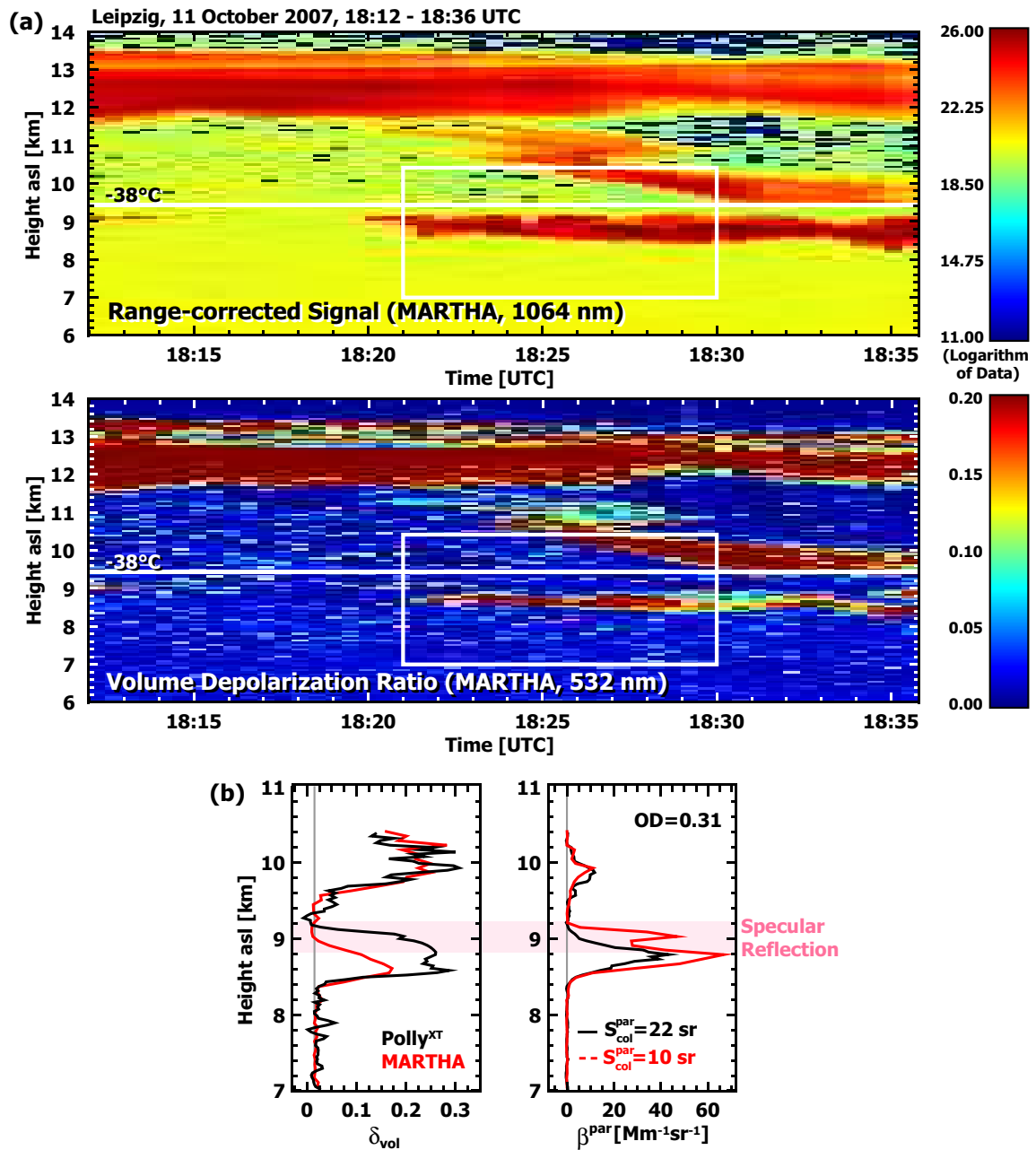
**Figure 5.20:** Illustration of the impact of a cloud containing layers of randomly oriented (A,C) and horizontally aligned, specular reflecting ice crystals (B) on observations with a zenith pointing lidar (MARTHA, red) and a  $5^\circ$  off-zenith pointing lidar (Polly<sup>XT</sup>, blue). Panels (b) to (d) depict measured particle backscatter coefficient  $\beta^{\text{par}}$ , extinction coefficient  $\alpha^{\text{par}}$ , and lidar ratio  $S^{\text{par}}$ , respectively.

coefficient  $\beta^{\text{par}}$  (b), extinction coefficient  $\alpha^{\text{par}}$  (c), and lidar ratio  $S^{\text{par}}$  (d) on layers in an idealized cloud (a) containing randomly oriented ice crystals only (layers A and C) and containing a fraction of horizontally aligned crystals (layer B). The red graph shows the respective values of the zenith-pointing lidar MARTHA whereas the blue one represents values of the  $5^\circ$  off-zenith pointing Polly<sup>XT</sup>. The parameters  $\beta^{\text{par}}$ ,  $\alpha^{\text{par}}$  and  $S^{\text{par}}$  measured with Polly<sup>XT</sup> do not show pronounced differences for the different layers A, B, and C. In turn, the curve for the idealized MARTHA observation of the horizontally aligned crystals in layer B shows rather high backscattering. The particle extinction coefficient is the same for both lidars, even in layer B. Hence, the particle lidar ratio observed in layer B is considerably lower for MARTHA in comparison to Polly<sup>XT</sup>.

A quantitative comparison between Polly<sup>XT</sup> and MARTHA measurements is presented in Fig. 5.21. Figure 5.21 (a) shows a measurement performed on 11 October 2007. A cloud layer was present between 8.4 and 9.2 km height. The temperature at cloud top was  $-38^\circ\text{C}$ . The occurrence of supercooled liquid water is still possible at these temperatures.

Mean profiles of volume depolarization ratio and particle backscatter coefficient determined with the Raman method [Mattis *et al.*, 2004] are presented in Fig. 5.21 (b) for the period indicated by a white frame in the color plots. The base and top height of the lower cloud layer at 8.4 and 9.2 km, respectively, are clearly visible in the profile of the particle backscatter coefficient of both lidar systems. The MARTHA measurement indicates rather low volume depolarization in the upper 200 m of the cloud, suggesting the presence of a supercooled water layer. However, the comparison with the volume depolarization ratio measured with Polly<sup>XT</sup> shows that the low volume depolarization ratio measured with MARTHA is caused by specular reflection of horizontally aligned ice crystals. This finding is corroborated by the comparison of the Raman particle backscatter coefficients measured with both lidars. The particle backscatter coefficient determined from MARTHA data is much stronger throughout the entire cloud layer than the values measured with Polly<sup>XT</sup>. Peak values of the MARTHA particle backscatter coefficient are one order of magnitude larger than the values of Polly<sup>XT</sup> reached in the top layer of the cloud. However, specular reflection affected the returned signal in all parts of the cloud. The average particle lidar ratio of the cloud layer was determined by applying the Klett–Fernald method as described in Seifert *et al.* [2007]. The cloud mean particle lidar ratio of the MARTHA measurement was found to be 10 sr whereas it was 22 sr for the Polly<sup>XT</sup> data. The cloud mean particle lidar ratio is the ratio of the cloud optical depth to the cloud-integrated particle backscatter coefficient and is typically around 20–30 sr for randomly oriented ice crystals [Sassen and Comstock, 2001; Seifert *et al.*, 2007]. Values around 10 sr show the strong impact of specular reflection on the retrieved particle backscatter coefficient. The optical depth of the cloud was calculated to be about 0.3 from both MARTHA and Polly<sup>XT</sup> data because the extinction retrieval is not affected by specular reflection.

Figure 5.22 presents another example of the volume depolarization ratio and the particle backscatter coefficient of a cirrus cloud observed simultaneously with MARTHA and Polly<sup>XT</sup> on 14 October 2007. The cloud layer occurred at altitudes between 10 and 12 km above



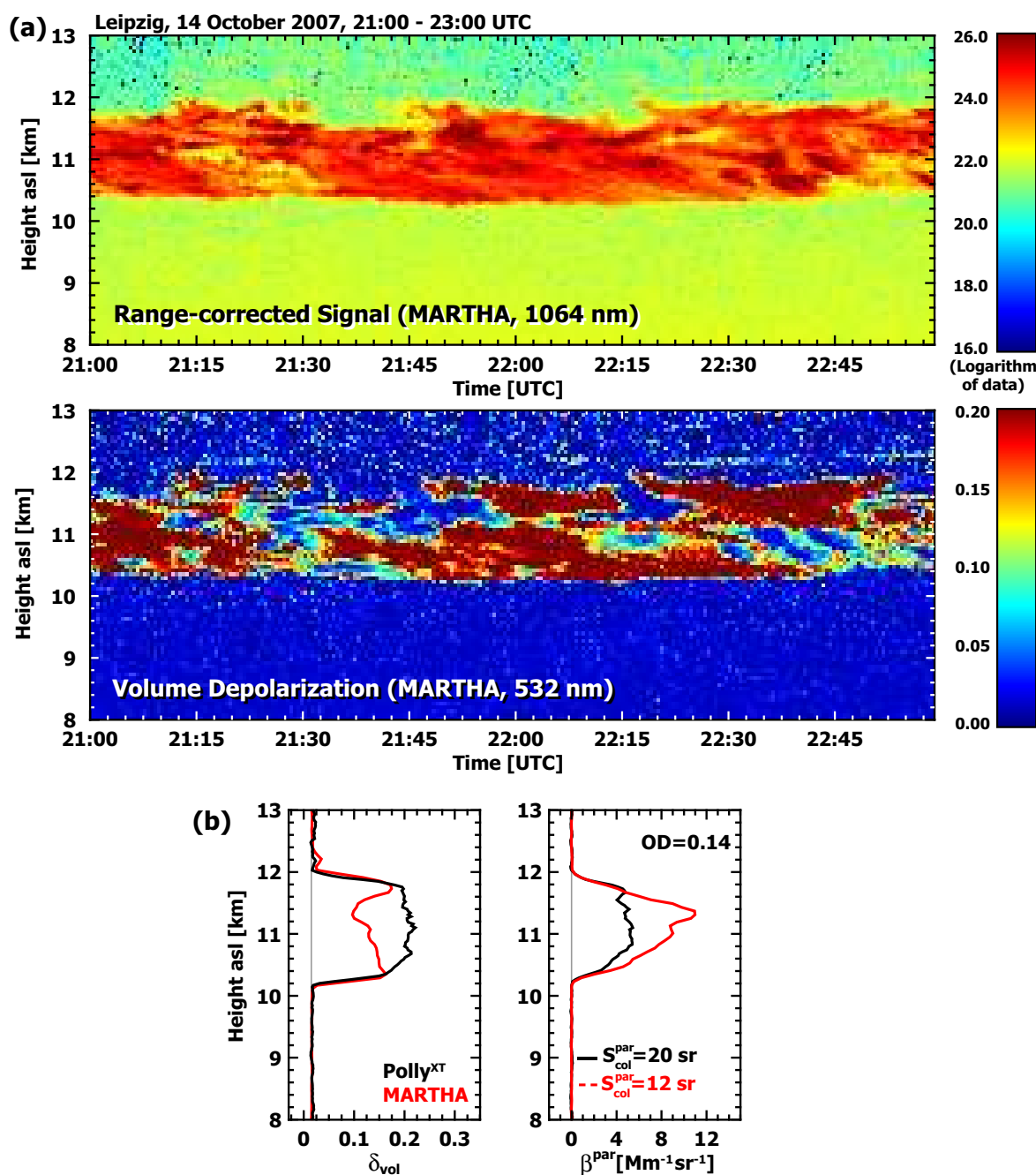


**Figure 5.22:** (a) Height–time cross section of the 1064–nm range–corrected signal and the 532–nm volume depolarization ratio measured with MARTHA on 14 October 2007. (b) Averaged vertical profiles of volume depolarization ratio  $\delta_{vol}$  and particle backscatter coefficient  $\beta^{par}$  observed with Polly<sup>XT</sup> (black) and MARTHA (red) for the full period shown in (a). The low layer–mean particle lidar ratio  $S_{col}^{par}$  of MARTHA compared to the value measured with Polly<sup>XT</sup> indicates the effect of specular reflection. The measured optical depth (OD) equals for both instruments.

ground, and cloud base and top temperatures were between  $-46$  and  $-62$  °C, respectively. Supercooled liquid water drops cannot exist at such low temperatures. Many blue areas (low depolarization) are visible in the depolarization panel. The comparison in Fig. 5.22 shows that the volume depolarization ratio measured with MARTHA is about 30%–50% lower than the one measured with Polly<sup>XT</sup>, whereas the particle backscatter coefficient of the MARTHA measurement reaches values which are up to 2.5 times higher than the particle backscatter coefficient derived from the Polly<sup>XT</sup> observation. As in the previous case, the cloud–mean particle extinction coefficients and thus the optical depths were equal and about 0.14 for both the MARTHA and Polly<sup>XT</sup> measurements. Thus, the derived particle lidar ratios measured with both instruments differ again. Whereas the specular–reflection–affected particle lidar ratio is only 12 sr in the case of MARTHA, a value of 20 sr was determined from the Polly<sup>XT</sup> data.

Figure 5.23 shows a measurement case that demonstrates the difficulties of cloud phase discrimination when a zenith–pointing lidar is used. A shallow, 200–m thick, non–depolarizing water layer at 6 km height and a specular–reflecting ice layer below were observed. The measurement was performed on 22 February 2007. A cirrus cloud at heights between 9.5 and 11 km was also present.

From the height–time cross section of the volume depolarization ratio in Fig. 5.23 (a) one would assume that the cloud system between 4–6 km height consisted of a layer of supercooled liquid water droplets at the top with another layer below consisting in parts of ice crystals and supercooled droplets. However, by averaging the lidar data over the time period indicated by the white rectangle in Fig. 5.23 (a) and computing the optical properties shown in Fig. 5.23 (b) with the Raman lidar method, strong differences become visible in the profiles of particle backscatter coefficient  $\beta^{\text{par}}$  and particle extinction coefficient  $\alpha^{\text{par}}$ . For the lower layer of the cloud system (3.5–5 km height) only the particle backscatter coefficient increases as a result of specular reflection up to values of  $\beta^{\text{par}} \approx 70 \text{ Mm}^{-1} \text{ sr}^{-1}$  whereas the particle extinction coefficient is almost zero because of the obviously rather low concentration of scatterers. In the upper layer of the cloud both parameters increase. The graph of the particle lidar ratio gives a better view of this behavior. In the lower layer  $S^{\text{par}}$  reaches values that are slightly above 0 sr whereas  $S^{\text{par}} \approx 20$  sr in the liquid water layer (altocumulus between 5.5–6 km height). A particle lidar ratio of around 18 sr is typical for liquid–water drops [O’Connor *et al.*, 2004]. The calculation of  $\beta^{\text{par}}$  and  $\alpha^{\text{par}}$  was used as additional source of information in critical cases of the 11–year DRIFT data set to identify the presence of ice crystals. Note again, that even in the case of strong specular reflection the volume depolarization ratio slightly increases at cloud base caused by an increasing number of randomly oriented ice crystals.

In the last two examples presented in Fig. 5.24 and 5.25, observations of pure liquid–water clouds are shown. The volume depolarization ratio is low (completely blue) in all clouds from 5–6.5 km height in Fig. 5.24 and in the cloud layer below 5 km in Fig. 5.25. To check whether these clouds are pure water clouds or whether they contain ice (horizontally oriented crystals), the backward–forward Klett–Fernald method was applied [Seifert *et al.*,

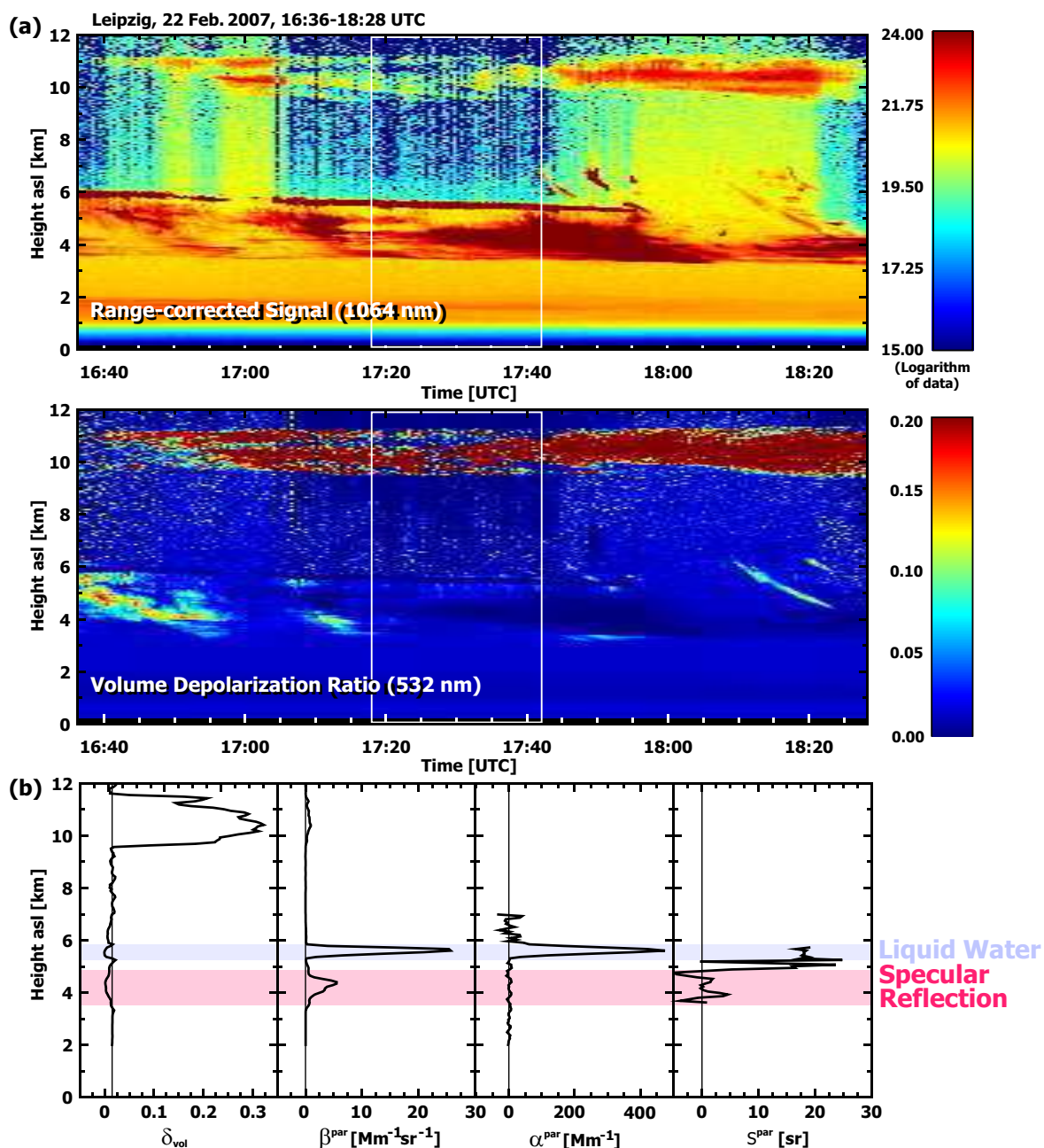


**Figure 5.23:** Separation of a water layer from a specular-reflecting ice layer with the Raman technique. (a) Height–time cross section of the 1064–nm range–corrected signal and the 532–nm volume depolarization ratio measured with MARTHA on 22 February 2007. (b) Averaged vertical profiles of volume depolarization ratio  $\delta_{\text{vol}}$  and Raman–derived particle backscatter coefficient  $\beta^{\text{par}}$ , extinction coefficient  $\alpha^{\text{par}}$ , and lidar ratio  $S^{\text{par}}$  for the time period indicated by the white boxes in (a).

2007]. This method is of advantage at daytime when Raman signals are weak, and can be applied to comparably small time periods of signal averaging. In the Klett–Fernald technique, the reference value of the particle backscatter coefficient is set in a region of negligible particle backscattering above or below the cloud. Then, the particle lidar ratio is varied in the Klett retrieval until the particle backscatter coefficient on the opposite side of the cloud equals the selected reference value of the particle backscatter coefficient (typically set to zero). If the particle lidar ratio is found to be in the range around 20 sr in optically thin water clouds (negligible multiple-scattering effect) and no depolarization is shown in the cloud layer, it consists unambiguously of liquid water droplets (see Fig. 5.24). If the particle lidar ratio reaches values of below 10 sr and the layer mean volume depolarization ratio is around zero, the layer unambiguously consists of horizontally aligned ice crystals (see Fig. 5.25). The backward–forward method was often used to check the cloud phase of apparently pure liquid–water clouds, indicated by low volume depolarization ratios throughout the cloud system.

## 5.7 Liquid/Ice-containing layer discrimination scheme for MARTHA

With respect to the identification of the phase–state of cloud layers measured with a zenith–pointing lidar the following conclusions were drawn from the investigation of specular reflection:

1. Because of the difficulty in identifying the phase state of each detected segment of a complex cloud system, clouds are categorized only as pure liquid–water clouds or ice–containing clouds. If the volume depolarization ratio is clearly enhanced at the base of a cloud, it is counted as an ice–containing cloud. If the depolarization is low throughout a cloud, keeping a small multiple–scattering effect into account, it is counted as a liquid cloud.
  2. In critical cases, e.g., low cloud top temperature of below  $-30\text{ }^{\circ}\text{C}$ , low volume depolarization ratio, the Raman–lidar and/or the Klett–Fernald methods are applied to determine whether a cloud is a pure water cloud (showing particle lidar ratios around 20 sr) or an ice–containing cloud (with particle lidar ratios of below 10 sr caused by specular reflection).
  3. If ice–crystal virgae, identified by enhanced depolarization, are detected below cloud base, the cloud layer is in general counted as ice–containing cloud, disregarding the volume depolarization ratio in the main cloud layer which may be close to zero.
-

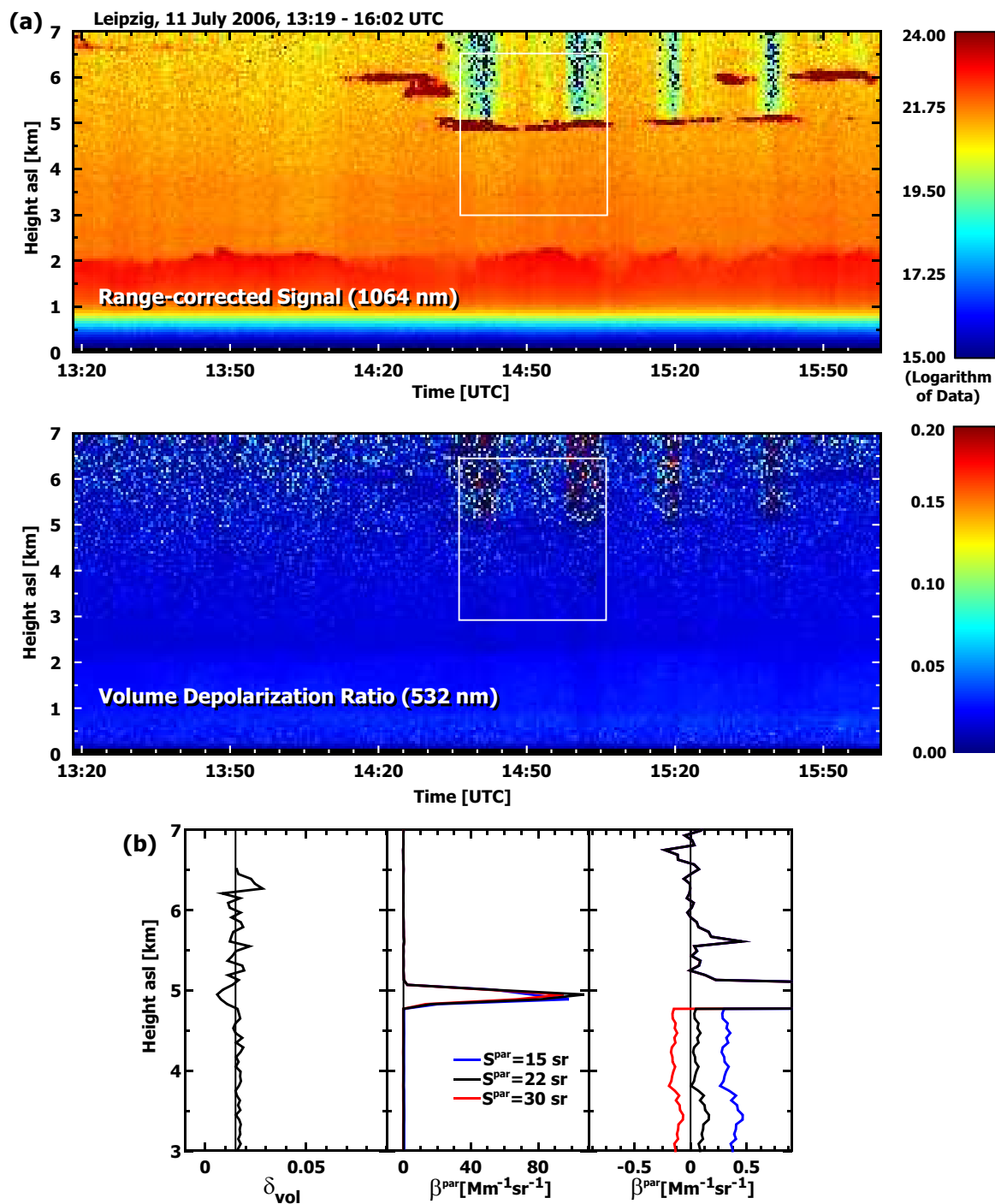


**Figure 5.24:** Classification of a water cloud with the Klett–Fernald method. (a) Height–time cross–section of the 1064–nm range–corrected signal and the 532–nm volume depolarization ratio measured with MARTHA on 11 July 2006. (b) Averaged vertical profiles of volume depolarization ratio  $\delta_{\text{vol}}$  and Klett–derived particle backscatter coefficient  $\beta^{\text{par}}$  for 3 different column–averaged particle lidar ratios  $S^{\text{par}}$ . The best solution is obtained for  $S^{\text{par}} = 20$  sr, indicating pure liquid water.

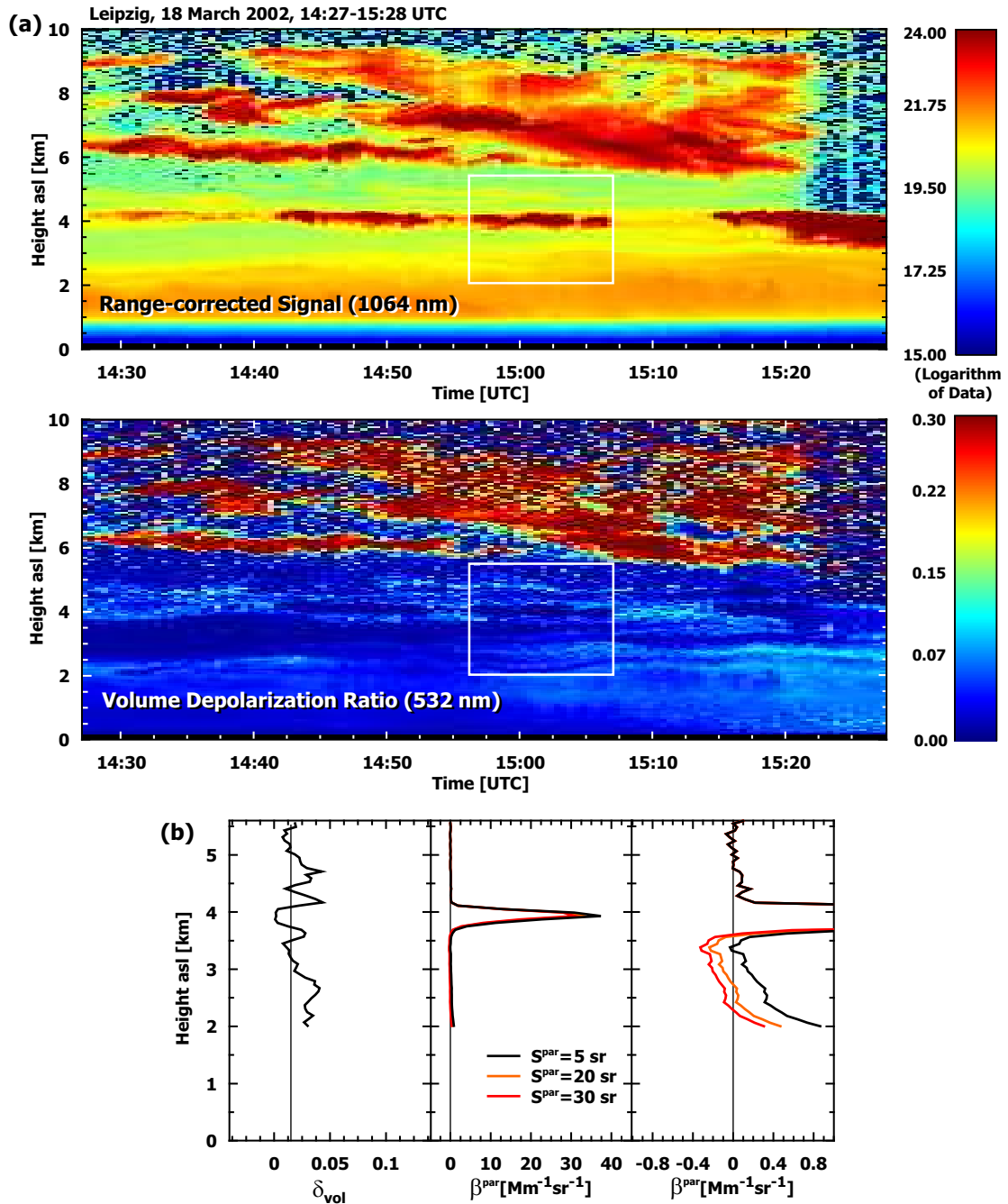


**Figure 5.25:** Classification of a specular-reflecting ice cloud with the Klett-Fernald method. (a) Height-time cross section of the 1064-nm range-corrected signal and the 532-nm volume depolarization ratio measured with MARTHA on 18 March 2002. (b) Averaged vertical profiles of volume depolarization ratio  $\delta_{vol}$  and Klett-derived particle backscatter coefficient  $\beta^{par}$  for three different column-averaged particle lidar ratios  $S^{par}$ . Only the backscatter profile for  $S^{par} = 5$  sr gives reasonable results ( $\beta^{par} > 0$   $Mm^{-1}sr^{-1}$  below cloud), indicating horizontally aligned ice crystals.



## Chapter 6

# Observations

Before the results of the statistical analysis of the cloud data set are discussed in the next chapter, case studies of cloud glaciation during a Saharan dust outbreak and in clean air are presented and contrasted in the following.

### 6.1 20 June 2007: Cloud development in Saharan dust

A period of strong Saharan dust outbreaks occurred from late spring to early summer of 2007. The synoptic condition was dominated by a low–pressure system over the Bay of Biscay and a high–pressure system over eastern Europe. This constellation provided preferable conditions for the advection of Saharan dust towards central Europe. One lidar measurement from this time period is shown in Fig. 6.1. The height–time cross sections of the range–corrected signal and of the volume depolarization ratio show the depolarizing dust layer that extends from the top of the boundary layer up to 5–6 km height. Desert dust particles are non–spherical and produce volume depolarization ratios from a few percent in almost dust–free air to values that are close to the particle depolarization ratio of 35% [Freudenthaler *et al.*, 2009] in heavily dust–laden layers. Traces of dust are visible in the profile of the 532–nm particle extinction coefficient up to 8 km height. The particle extinction coefficient was calculated with the Klett–Fernald method (see Section 4.3.1) because Raman signals are too noisy during daylight conditions. The a–priori particle lidar ratio was chosen to be 55 sr which is the characteristic value for Saharan dust [Ansmann *et al.*, 2003; Müller *et al.*, 2007; Esselborn *et al.*, 2009; Tesche *et al.*, 2009b]. The optical depth of the dust layer was about 0.1 at 532 nm. The HYSPLIT backward trajectories which are also shown in Fig. 6.1 do not provide a clear picture of the dust transport in this case. Nevertheless, the trajectory calculations show that the dust was advected from northern Africa at heights from 2–5 km and traveled roughly 3–5 days before arriving at Leipzig. A clearer picture and, more important, a quantitative measure for the dust load over Leipzig is given by the calculations of DREAM (see Section 5.3). Figure 6.2 (a) presents the column dust load for the whole model domain as it was calculated for 12 UTC on 20 June 2007. In Fig. 6.2 (b) the vertical distribution of mineral dust at the grid point of Leipzig [red star in Fig. 6.2 (a)] is shown.

---

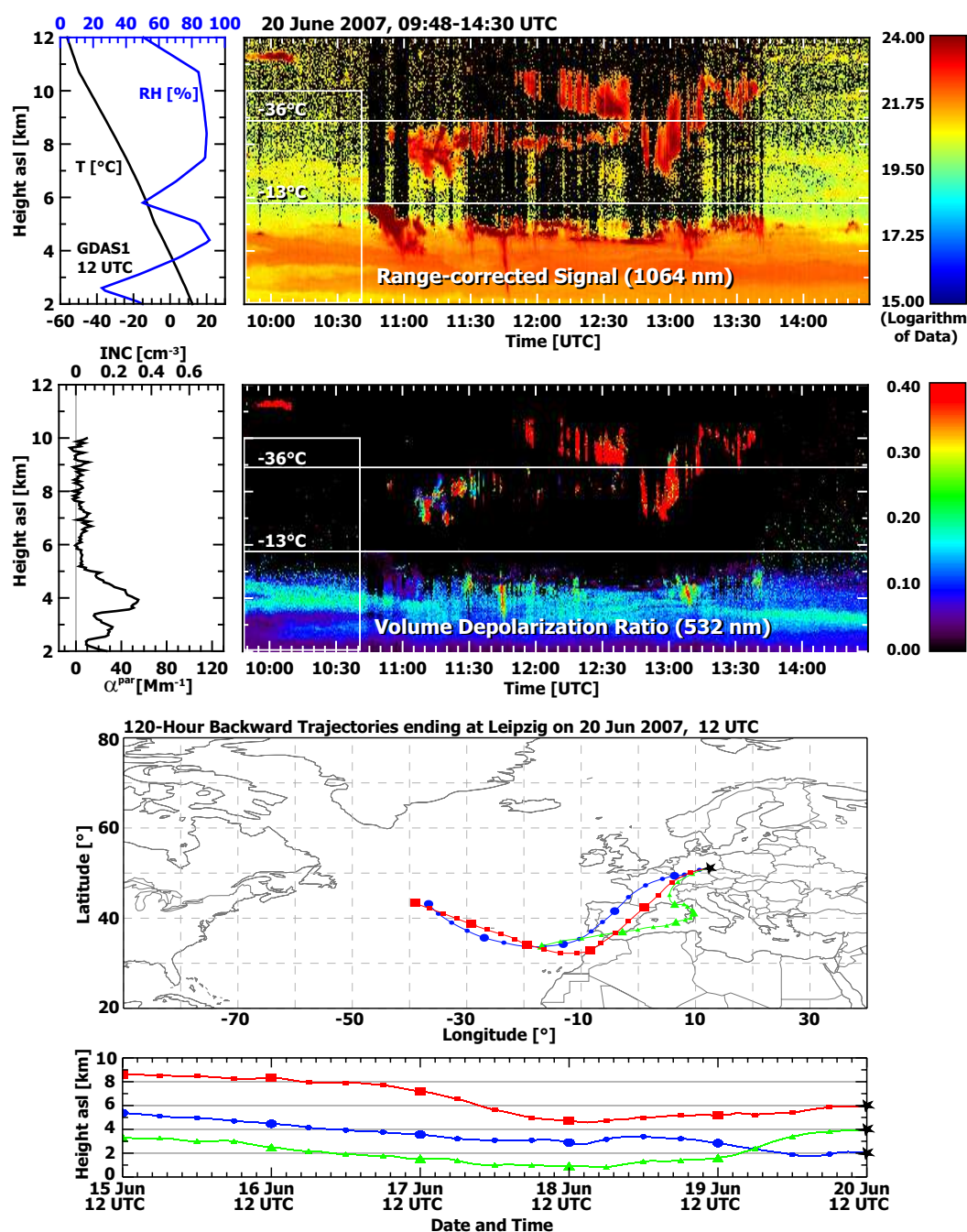


**Figure 6.1:** Ice-precipitating altocumulus clouds between 3 and 6 km height on 20 June 2007. The clouds develop in the upper part of a Saharan dust layer. Range-corrected 1064-nm signal (top, arbitrary units) and volume depolarization ratio at 532 nm are shown. Green to red column-like features from 3–5 km height in the depolarization plot indicate virgae containing ice crystals. In the left panels, height profiles of the simulated GDAS temperature and humidity profiles for the Leipzig grid point at 12 UTC (top), and particle extinction coefficient at 532 nm and estimated IN concentration are given (bottom). Aerosol properties are computed from the mean signal profiles observed from 09:50–10:40 UTC (indicated by a white frame). Temperature levels (horizontal lines) are taken from the temperature profile. Backward trajectories ending at Leipzig at 2, 4, and 6 km height are computed with HYSPLIT (see Section 5.3).

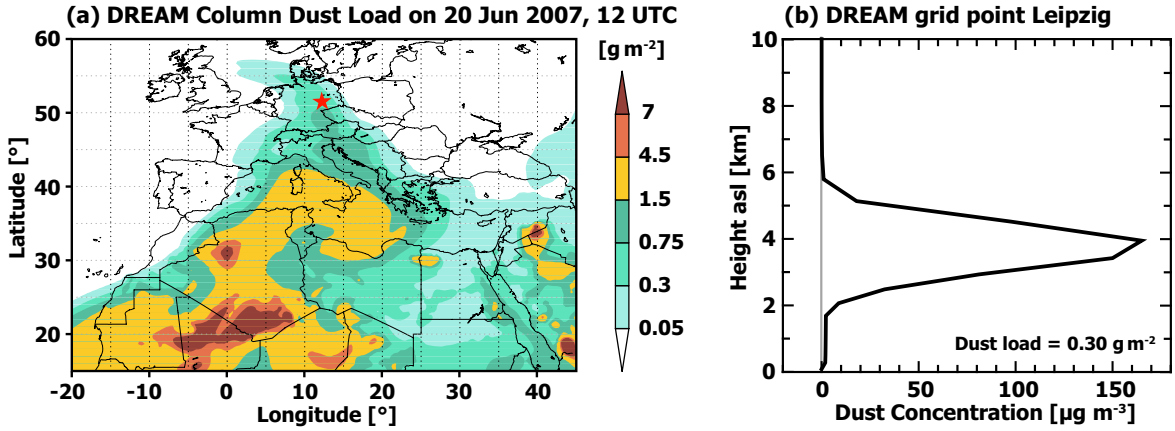


**Figure 6.2:** (a) Column mass concentration and (b) concentration of mineral dust particles calculated with the DREAM model for 20 June 2007, 12:00 UTC. The red star in (a) designates the location of Leipzig for which a column dust load of  $0.3 \text{ g m}^{-2}$  was calculated.

There is a remarkably good agreement between the modeled vertical distribution of the dust concentration and the profile of the particle extinction coefficient shown in Fig. 6.1. This is a good demonstration of the reliability of DREAM.

The temperature and humidity profiles are taken from the GDAS1 assimilation data set. The humidity profile indicates two moist layers in which the altocumulus and the cirrus clouds developed. Cirrus clouds (including virga) are visible from 7–11.5 km height. From the scene shown in Fig. 6.1 three ice-containing clouds were identified for the statistics. Information about occurrence time, heights, and temperatures of the cloud boundaries, cloud phase, and corresponding DREAM dust concentration within 500 m of the cloud boundaries as they were used for the statistical analysis in the following chapters are compiled in Table 6.1.

The plot of the range-corrected signal in Fig. 6.1 indicates that shallow altocumulus formed at the top of the dust layer at temperatures above  $-13 \text{ }^\circ\text{C}$ . The high volume depolarization ratio (red) in several virgae below the main cloud layer indicates ice formation at these high temperatures. A strong virga that occurred from 10:41 to 13:45 UTC shows increased depolarization down to a height of 3 km and temperatures of around  $5 \text{ }^\circ\text{C}$ . It is therefore likely that large aggregates of ice crystals or graupel formed in the altocumulus

**Table 6.1:** Clouds identified from the measurement on 20 June 2007 presented in Fig. 6.1.  $H_b/H_t$  refer to cloud base/top height and  $T_b/T_t$  to cloud base/top temperature, respectively. Maximum dust concentration within 500 m of the cloud boundaries was obtained from DREAM.

Time [UTC]	Duration [min]	$H_b/H_t$ [km]	$T_b/T_t$ [ $^\circ\text{C}$ ]	Phase State	Max. Dust Conc. [ $\mu\text{g m}^{-3}$ ]
09:48–10:10	22	10.97/11.67	$-52/-55$	ice-containing	$<0.01$
10:41–13:45	184	3.94/5.80	$-1/-13$	ice-containing	165.
10:54–13:45	171	6.66/10.96	$-19/-52$	ice-containing	0.22

layer because the crystals passed approximately 1000 m of air at temperatures above 0 °C without melting entirely. In the cross section of the range-corrected signal in Fig. 6.1 the melted virga that produces no depolarization anymore is visible down to at least 2 km height. The precipitation produced in the approximately 200 m thin altocumulus cloud layer from which the virga originated was exceptionally strong and nothing comparable was found in the altocumulus studies presented by *Ansmann et al.* [2008] and *Ansmann et al.* [2009] for Morocco and Cape Verde, respectively. Mixed-phase clouds (blue areas mixed with green to red areas in the depolarization ratio plot) may be present in the upper cloud layer up to 8.5 km height with temperatures of -36 °C. However, it cannot be excluded that the low depolarization ratio is caused by specular reflection. This is also the case for the cloud that occurred at 11:00 UTC in the altocumulus deck on top of the dust layer.

It is unlikely that cloud seeding effects (see Section 2.3) influenced the ice formation in the lower altocumulus layer. According to the humidity profile of GDAS1 the upper cloud was separated from the lower layer by 2 km of dry air and no indications are given that strong virgae, which are needed for effective seeding were produced in the upper layer.

The particle extinction coefficients derived from the lidar observations are 20–60  $\text{Mm}^{-1}$  in the main dust layer from 3.5–5.0 km height. The values of the dust particle extinction coefficients indicate aerosol particle number concentrations (APC) with radii larger than 250 nm of roughly 10–35  $\text{cm}^{-3}$  according to the study presented by *Ansmann et al.* [2008] for pure Saharan dust. There, the relationship between the lidar-derived particle extinction coefficient and the sunphotometer-derived particle size distribution for a pure-dust scenario is described. The INC values in Fig. 6.1 are estimated by assuming that particle extinction coefficients of 1, 10, and 50  $\text{Mm}^{-1}$  indicate INC values of 0.006, 0.06, and 0.3  $\text{cm}^{-3}$ , respectively, according to the APC/INC ratio of 100 as it was published by *Stith et al.* [2009] and *DeMott et al.* [2009] (see Section 2.2.2 for more details). The measured particle extinction coefficients of 20–60  $\text{Mm}^{-1}$  at cloud level thus indicate high INC values of about 0.1–0.35  $\text{cm}^{-3}$ . Free-tropospheric background values are of the order of 0.001 to 0.01  $\text{cm}^{-3}$  [*Richardson et al.*, 2007].

Regarding the relevance of the different heterogeneous ice nucleation processes that were introduced in Section 2.3 the following conclusions can be drawn from the lidar observation of the dust-embedded altocumulus layer on 20 June 2007:

- During most of the time the cloud top consisted of supercooled liquid water. Therefore, condensation and deposition nucleation must have played only a minor role for ice formation.
- The development of the long-lasting virga at 11:00 UTC suggests the formation of very large aggregates of crystals or graupel in an approximately 200 m thin cloud layer. This gives reason to assume that only few ice crystals formed in the layer which could later on grow quickly to large sizes by the Bergeron-Findeisen process. Probably contact nucleation occurred. Contact nucleation is the most effective process at temperatures higher than approximately -15 °C [*Pitter and Pruppacher*, 1973], especially when

large, dry aerosol particles are available to allow for efficient collisions. Large aerosol particles can be expected in the presented case of a strong Saharan dust outbreak.

## 6.2 3 November 2003 and 24 November 2006: Cloud development at aerosol background conditions

Figure 6.3 shows the development of three altocumulus layers at 6 and 7 km height on 3 November 2003. The liquid–water cloud layer formed at almost  $-32$  °C around 6 km height. In the layer around 7 km height temperature conditions were already favorable for homogeneous ice nucleation. Trajectories indicate that the clouds formed in a clean air mass that was advected from the North Atlantic and was always above 4 km height during the last five days of the transport to Leipzig. The low values of extinction and INC of the order of  $0.01 \text{ cm}^{-3}$  confirm that the clouds developed under aerosol background conditions. For the statistics, two liquid–water clouds and one ice–containing cloud were counted. Statistical information obtained for each cloud is summarized in Table 6.2.

Extended fields of mixed–phase clouds that formed at aerosol background conditions at 6 and 7 km height are shown in Fig. 6.4. Typical altocumulus structures with a liquid layer at cloud top (at  $-26$  °C) and ice–containing virgae below the main cloud layer were observed for more than two hours. Cloud seeding seems to have contributed to the ice production in the lowermost altocumulus deck. The air mass was advected from the North Atlantic according to the backward trajectories and always stayed above 4 km height during the last three days before arriving at Leipzig. The DREAM column dust load and the profile of dust concentration at Leipzig shown in Fig. 6.5 confirm that cloud formation occurred in dust–free air. It should be noted that the scale of the dust concentration profile in Fig. 6.5 (b) spans values that are two orders of magnitude lower than the ones shown in the respective profile in Fig. 6.2 (b). For the statistics, one long–lasting ice–containing cloud layer is counted for the case presented in Fig. 6.4 (see Table 6.2).

*Morrison et al.* [2005] show that the observed extended liquid–water layers can only persist for a longer time period in the presence of ice when the ice nucleation processes are slow enough. This is the case when contact nucleation takes place and the formed ice crystals precipitate quickly. Thus, according to *Morrison et al.* [2005], deposition and condensation nucleation can play a minor role only, because these processes would lead to large number concentrations within a short time period and completely deplete the liquid layers. Contact nucleation was suggested to be the dominant ice nucleation process. Furthermore, *Morrison et al.* [2005] pointed out that updrafts of  $10\text{--}50 \text{ cm s}^{-1}$  are permanently required to form new drops in the liquid layer. Radiative cooling of the cloud top triggers downward motion, turbulence, and subsequently updrafts.

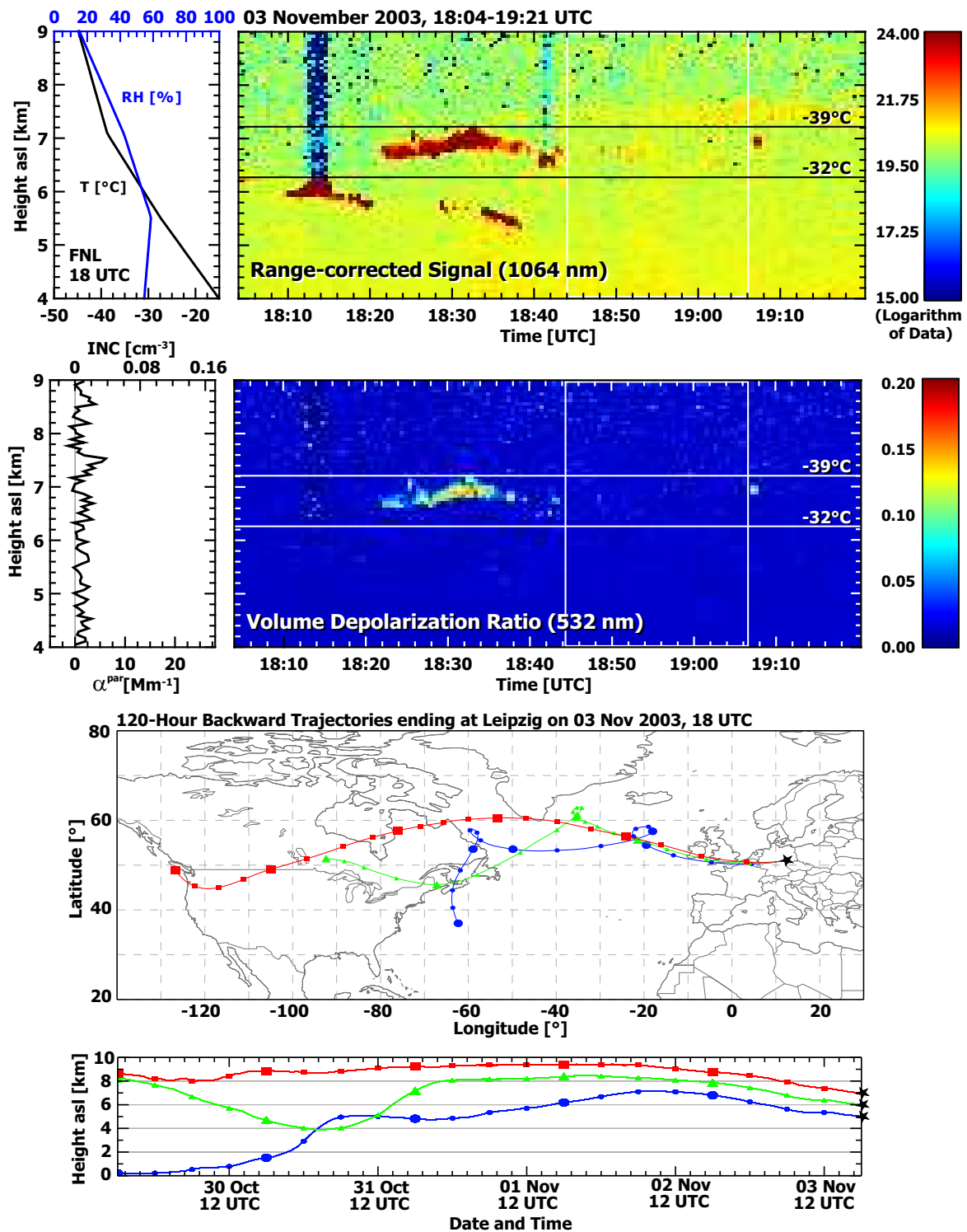


Figure 6.3: Same as Fig. 6.1, except for 3 November 2003. Development of liquid-water clouds at  $-32^\circ\text{C}$  at dust-free aerosol background conditions. An ice cloud formed at  $-39^\circ\text{C}$ .

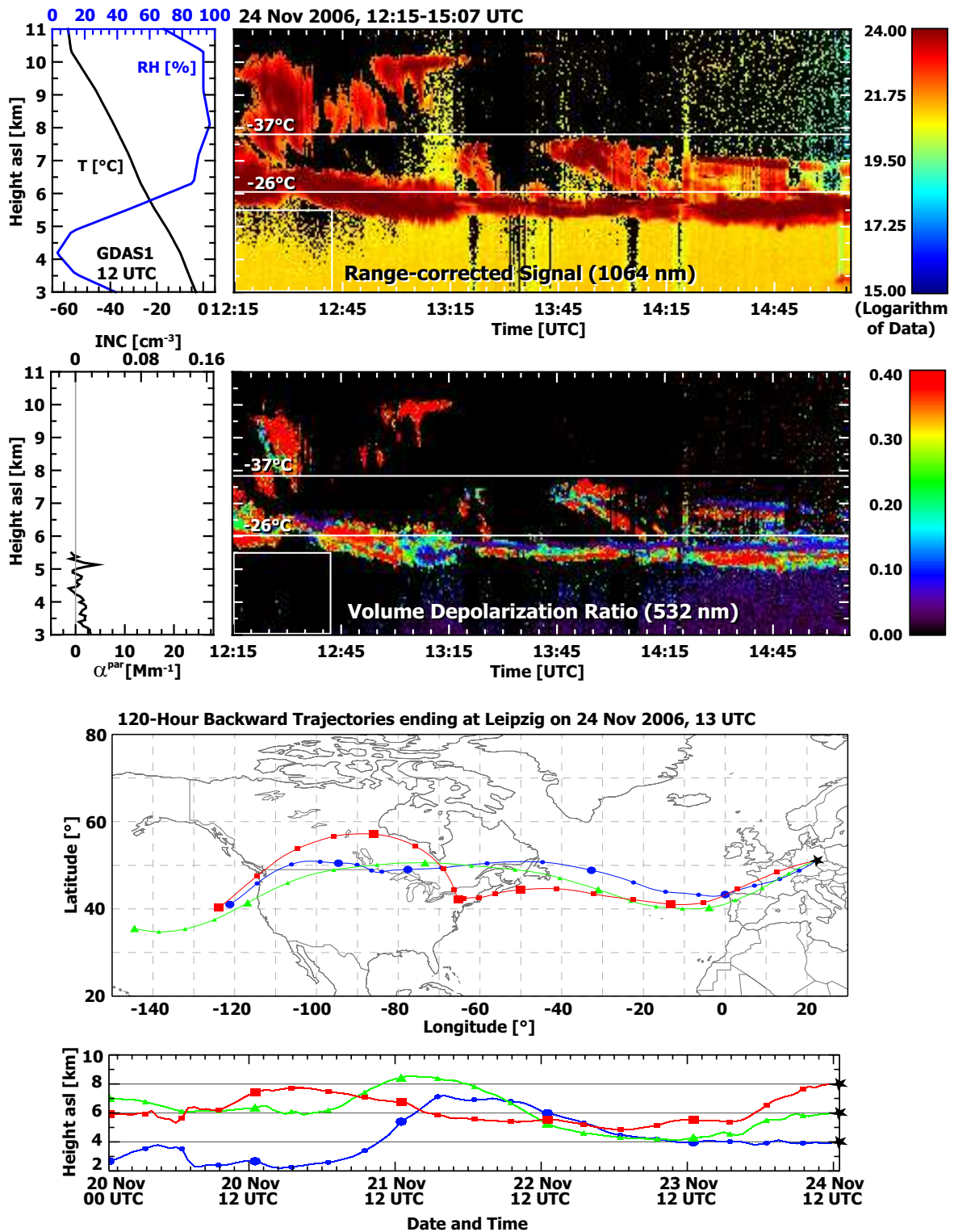
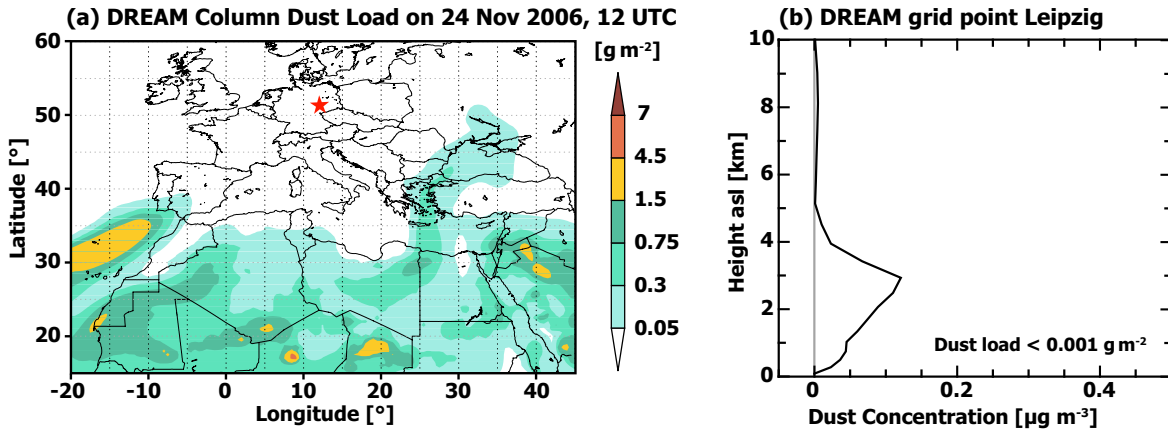


Figure 6.4: Same as Fig. 6.1, except for 24 November 2006. Extended ice-precipitating altocumulus layers developed in dust-free air in the height range from 5.0–8.0 km. Heterogeneous ice nucleation occurred at temperatures from about  $-26^{\circ}\text{C}$  to  $-37^{\circ}\text{C}$ . Cloud seeding effects partly contributed to ice formation in the lower cloud layers.



**Figure 6.5:** Same as Fig. 6.2, except for 24 November 2006, 12 UTC. Column dust load at grid point Leipzig (red star) was below  $0.001 \text{ g m}^{-2}$ .

### 6.3 26 May 2008 and 26 December 2008: Indications for deposition nucleation

The following two measurement examples show scenarios where most probably water vapor was directly transferred to the ice phase by deposition nucleation or, since both processes are hard to distinguish in field observations, by condensation nucleation.

An interesting case of a cloud life cycle was observed in the afternoon of 26 December 2008 (see Fig. 6.6). The observation is consistent with the following explanation. The advection of the altocumulus cloud field from northerly to northeasterly direction (visible by eye already several hours before crossing the lidar) is combined with the advection of warm and moist air. The cloud front marks the warm front. The approach of moist air leads to a slow and steady increase of the relative humidity over the lidar site. The depth (vertical extent) of this moist layer increases due to descent of the base of the moist layer. In this moist layer, ice nucleation starts when a certain ice saturation level is exceeded. The observation of the liquid layer indicates that ice formation starts 30 minutes before water saturation is reached (indicated by the liquid layer). Temperatures of  $-28$  to  $-32$  °C are rather favorable for

**Table 6.2:** Same as Table 6.1, except for measurements of 3 November 2003 and 24 November 2006 presented in Fig. 6.3 and 6.4, respectively.

Time [UTC]	Duration [min]	$H_b/H_t$ [km]	$T_b/T_t$ [°C]	Phase State	Max. Dust Conc. [ $\mu\text{g m}^{-3}$ ]
<b>03 Nov 2003</b>					
18:22–18:40	18	6.60/7.30	−36/−39	ice-containing	<0.001
18:11–18:20	9	5.63/6.20	−29/−34	liquid water	<0.001
18:34–18:39	5	5.18/5.75	−26/−30	liquid water	<0.001
<b>24 Nov 2006</b>					
12:15–15:07	172	4.90/10.57	−17/−57	ice-containing	0.01

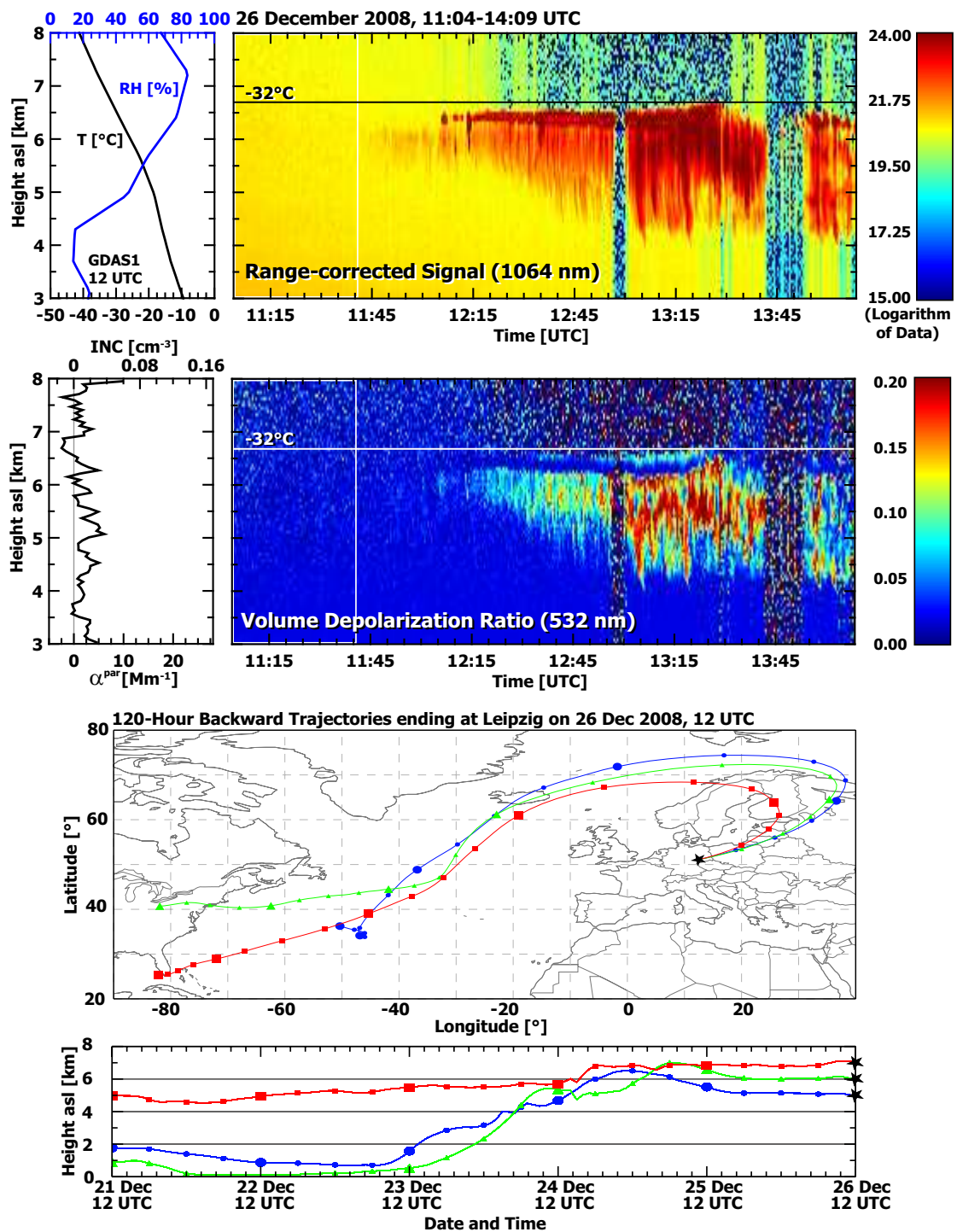


Figure 6.6: Same as Fig. 6.1, except for 26 December 2008. An almost complete life cycle of an altocumulus from the formation of liquid cloud cells to complete glaciation was observed. The backward trajectories indicate that the air mass in which the cloud layer formed originated from low heights over the subtropical North Atlantic and thus may have contained dust, maritime, and anthropogenic particles.

deposition and condensation nucleation [Pruppacher and Klett, 1997]. The vertical range of freshly formed ice crystals coincides with the position of the moist layer which also deepens with time by lowering of the layer base height. With time, relative humidity at the top of the moist layer reaches 100% (saturation over liquid water). The cloud forms and the released latent heat may lead to an ascent of the cloud layer by 50 to 100 m. Radiative cooling below the cloud improves the conditions for ice formation (temperatures decrease slightly, relative humidity increases slightly) indicated by the strengthening of the backscatter signal from ice crystals. Simultaneously, ice formation in the liquid layer and subsequent precipitation of ice crystals contribute to the strong backscatter signals below the cloud and the further descent of the base height of the moist, ice-containing layer. Radiative cooling also leads to a cooling of the boundary layer (below 1 km height) and triggers cloud formation at its top (indicated by the blue columns in the time–height displays in Fig. 6.6 at around 13:00 and 13:45 UTC). The ice-containing cloud observed during the measurement on 26 December 2008 is not included in the statistics since the DRIFT campaign ended in June 2008.

A second observation is presented in Fig. 6.7. The measurement was performed from 19:03–21:07 UTC on 26 May 2008 during a strong Saharan dust outbreak. Liquid–water layers were not observed. Only layers of ice crystals occurred. Backward trajectories calculated for heights from 4–8 km all originated over northern Africa. The panels of range–corrected signal and volume depolarization ratio indicate the depolarizing dust layer up to heights of 9 km. Also the profiles of particle extinction coefficient and IN concentration which were calculated for the time period from 20:20–20:40 UTC show elevated values up to this height. The Saharan dust plume reached peak INC of  $0.7 \text{ cm}^{-3}$ . Even at 9 km height estimates of  $0.1 \text{ cm}^{-3}$  indicate high INC, one to two orders of magnitude higher than the tropospheric background value. The 21 UTC GDAS1 humidity profile indicates two humid layers at 5 and 7.5 km, respectively. In the upper one of these layers, between 7.5 and 8.5 km height ( $-25$  to  $-33 \text{ }^\circ\text{C}$ ), clouds were observed. Temperatures thus were above the level of homogeneous nucleation and favorable for deposition, condensation, and immersion nucleation [Field *et al.*, 2006; Connolly *et al.*, 2009]. The clouds formed sporadically in clusters of only a few minutes in length. Only slightly enhanced backscatter signals and patches of increased depolarization were observed. No indications for a persistent liquid–water layer at their tops are given. Immersion or contact nucleation are thus unlikely to occur. In addition, no virgae were observed during the measurement. Therefore, it is likely that the formation of many small non–precipitating ice crystals occurred via the pathway of deposition or condensation nucleation. For the statistical data set, two cloud cases were found in the measurements presented in Fig. 6.7. They are listed in Table 6.3.

**Table 6.3:** Same as Table 6.1 except for measurements of 26 May 2008 presented in Fig. 6.7.

Time [UTC]	Duration [min]	$H_b/H_t$ [km]	$T_b/T_t$ [ $^\circ\text{C}$ ]	Phase State	Max. Dust Conc. [ $\mu\text{g m}^{-3}$ ]
19:03–19:55	52	7.32/8.31	$-25/-36$	ice-containing	297.
19:02–19:37	35	9.68/10.95	$-45/-55$	ice-containing	25.

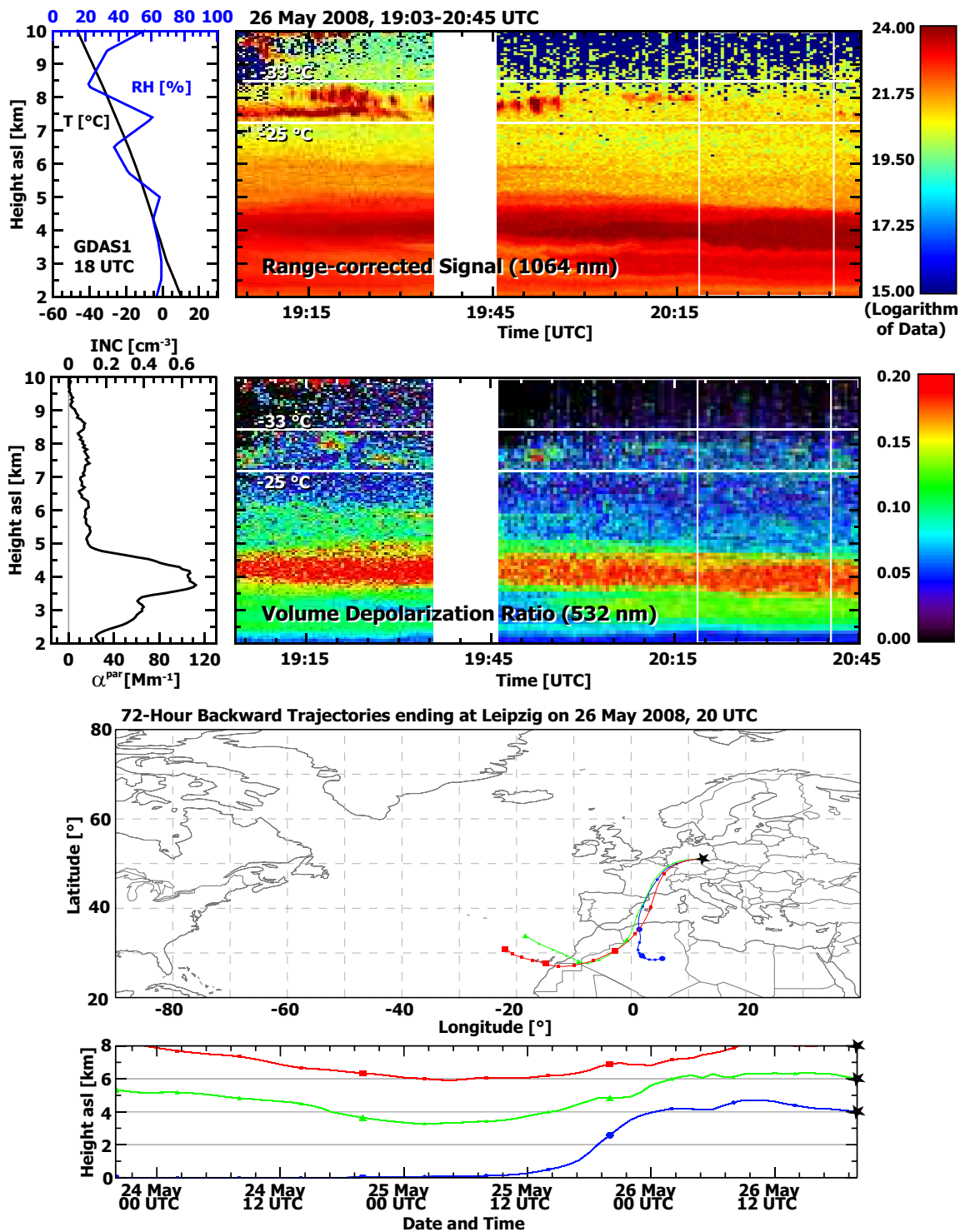


Figure 6.7: Same as Fig. 6.1, except for 26 May 2008. Thin filaments of ice clouds were observed during a Saharan dust outbreak. Even though temperatures were still below the level of homogeneous nucleation liquid water was absent. Given the weak backscatter signal of the clouds deposition nucleation is likely to have caused ice formation.



## Chapter 7

# The MARTHA 1997 – 2008 cloud data set

The following chapter presents the results of the statistical analysis of the MARTHA data set in terms of cloud properties and their relationship to temperature and the presence of Saharan dust. Basic information about the underlying lidar data set and the derived cloud layers is presented in Section 7.1. Section 7.2 concentrates on the analysis of the geometrical cloud properties. In Section 7.3, the relationship between heterogeneous ice nucleation and temperature is illuminated. Studies concerning the effect of Saharan dust on heterogeneous freezing are presented and discussed in Sections 7.4 and 7.5. The main points of the presented investigations were recently accepted for publication in a peer-reviewed journal [*Seifert et al.*, 2010].

### 7.1 Statistical basis

In the scope of the presented work all measurements since the start of regular observations in April 1997 until the major system upgrade in June 2008 [*Schmidt*, 2009] were evaluated for cloud occurrences according to the scheme presented in Chapter 5. The type of measurement can be separated into three groups — regular observations, DRIFT observations, and additional observations which are performed in case of special events like Saharan dust outbreaks or when smoke plumes cover large parts of Europe. Since 1997 MARTHA at IfT Leipzig has been a member of lidar networks. A fixed measurement schedule has been mandatory for all lidar stations of the networks in order to ensure a solid statistically unbiased data record. The measurement schedule specifies that regular measurements have to be carried out on Mondays at noon and after sunset as well as on Thursdays after sunset. From 1997 to 1999 measurements at Leipzig had been performed in the framework of the German lidar network. Since 2000 measurements have been performed within Earlinet.

Figure 7.1 illustrates the type, frequency, and duration of the measurements performed between 1997 and 2008. Mandatory Earlinet observations (blue lines) concentrate on the time enclosed by the straight lines (daytime) and curved black lines (after sunset) that denote the

---

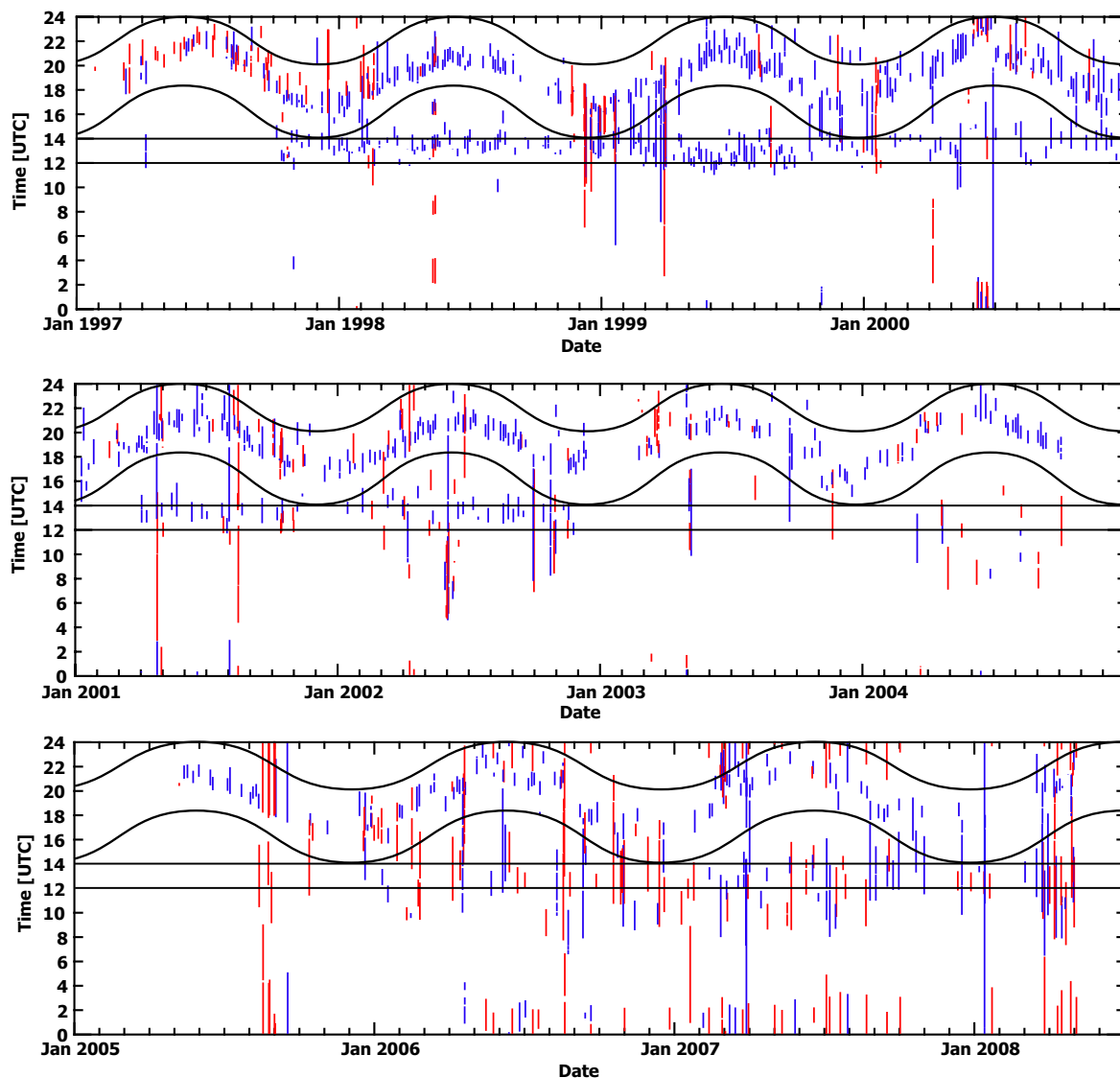


**Figure 7.1:** Frequency, duration, and type of MARTHA measurements from 1997 to 2008. Start and end points of the vertical lines detach start and end time of observations. Black horizontal lines and curves enframe the obligatory times of the regular noon and evening measurements performed within the German lidar network and Earlinet. Blue: Regular measurements within Earlinet and the German lidar network; red: additional measurements.

observational times specified in the fixed measurement schedule. Reasons for larger gaps in the time series are caused primarily by instrumental problems or bad weather, e.g., rain, fog, or overcast situations with clouds below 1 km height. A smaller density of measurements can be seen from 2003 to 2005. During this time, Earlinet was not funded and measurements were performed only voluntary. In addition, a major laser failure occurred in October 2004 so that a resumption of measurements was not possible before April 2005. In 2006 the frequency of additional measurements (red lines) increased. These measurements were motivated by the onset of the DRIFT studies as well as by the need to perform correlative measurements

**Table 7.1:** Number of measurement sessions and measurement hours of the regular network-related lidar observations performed within the German lidar network and Earlinet, DRIFT observations, and additional measurements.

Measurement Type	Time Period	Number of Measurements	Measurement Hours
Regular observations	1997–2008	781	1389
DRIFT	2006–2008	57	205
Additional	1997–2008	259	751
Total		1097	2345

for the space-borne Cloud-Aerosol Lidar with Orthogonal Polarization (CALIOP) aboard the polar-orbiting CALIPSO satellite [*Winker et al.*, 2007].

Information on the number and duration of the different measurement types are given in Table 7.1. As can be seen from the table, the regular observations in the framework of the German lidar network and Earlinet contribute the majority of the measurement cases and measurement hours. Additional observations and DRIFT measurements (February 2006 to June 2008) make up fraction of approximately 50% of all measurements.

All lidar measurements were reanalyzed with respect to clouds according to the scheme described in Chapter 5. Times of occurrence, top and base heights and temperatures as well as the phase state of every cloud layer were determined. Table 7.2 gives an overview of the retrieved cloud data set. 2319 cloud cases were determined with a total occurrence time of 1475 hours. 1899 of the observed cloud cases passed the quality check which means that the cloud phase as well as the cloud top could be determined accurately. Well-defined liquid-

**Table 7.2:** Cloud statistics from the 1997–2008 lidar data record. In 82% of the observed 2319 cases the cloud layers were well defined in terms of cloud phase and top height. Ice-containing clouds are in addition split up into estimated contributions of mixed-phase clouds and pure ice clouds.

April 1997 – June 2008	Cases	% of Cases	Hours	% of Hours
<b>Related to all cases</b>				
Observed cloud layers	2319		1475	
<b>Related to well-defined cases</b>				
Observed cloud layers	1899	100%	1204	100%
Liquid-water clouds	790	42%	213	18%
Ice-containing clouds	1109	58%	991	82%
Mixed-phase clouds	235	12%	170	14%
Pure ice clouds	874	46%	821	68%
Clouds with $T_{\text{top}} < -40$ °C	753	40%	743	62%
Clouds with $T_{\text{top}} > -40$ °C, $< 0$ °C	789	42%	378	32%
Clouds with $T_{\text{top}} > 0$ °C	357	19%	83	6%

water clouds were found in 790 cases and make up a fraction of 42%. With a fraction of 18% their contribution to the cloud occurrence time (214 hours) is much lower. The longevity of stratiform cirrus clouds increases the fraction of the 1109 ice-containing cloud layers to 82% of the occurrence time whereas they make up only a fraction of 58% of the number of well-defined cases. Disregarding the ambiguity in the depolarization observation (see Section 5.6) it was attempted to separate the ice-containing cloud layers into mixed-phase and ice clouds, respectively. A cloud layer was classified as mixed phase when it was observed at temperatures  $-35\text{ }^{\circ}\text{C} < T_{\text{top}} < 0\text{ }^{\circ}\text{C}$  and showed both virga-like structures and regions of low depolarization. However, concerning the potential impact of specular reflection, the uncertainty in this classification is about 5% to 10%.

A total of 420 cloud cases, 18% out of all cases, was excluded from further analysis. In 230 cases, low-quality depolarization measurements inhibited a determination of the cloud phase and in 190 cases the cloud top height could not be determined. The determination of the cloud top was in most cases not possible for long-lasting clouds as stratocumulus decks and warm-front cirrostratus. Cloud phase determination was occasionally hampered by low-quality depolarization measurements caused by frequent modifications of the receiver unit during lidar upgrading periods so that a proper alignment was not always possible. Figure 7.2 illustrates the temporal distribution of the cases for which the cloud phase could not be defined. The undefined cases accumulate in the years 1999 to 2001. Frequent modifications of the 532-nm detection branch (including the depolarization channels) and the implementation and tests of new Raman channels for temperature measurements in cooperation with a lidar group from Tomsk, Siberia, were performed during this period. The lidar field of view was often changed. These activities were finished in 2001. Other sporadic maxima of undefined

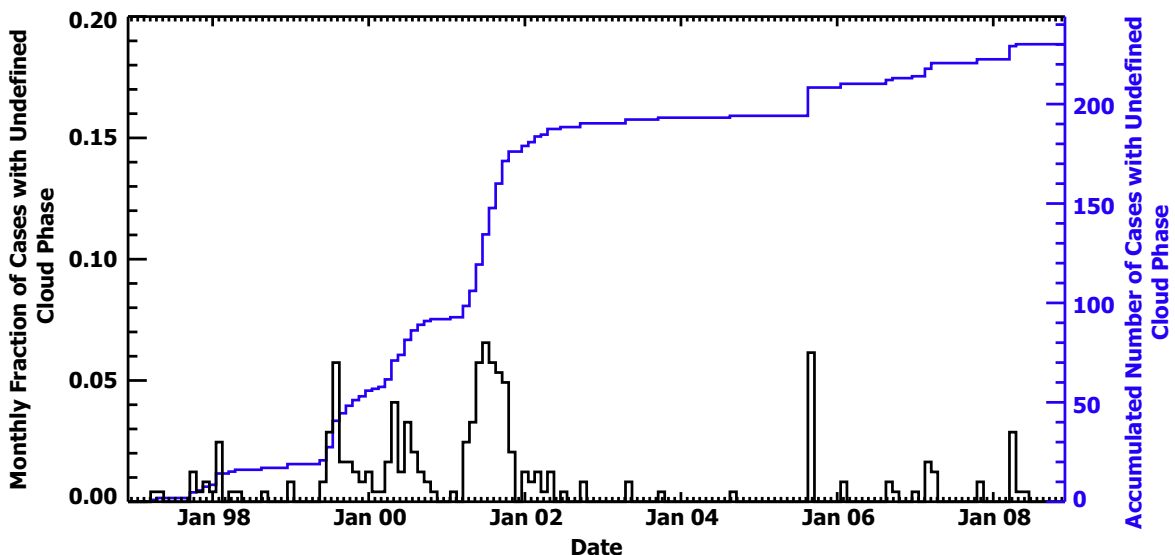


**Figure 7.2:** Temporal distribution of the cases for which the cloud phase could not be defined. Black line: Ratio between the the monthly number of undefined cases and the total number of observed cloud cases. Blue line: Cumulative distribution of undefined cases.

cloud phase can be attributed to the lack of depolarization channels which were deactivated in some cases as from October to November of 2005. Only in a few cases cloud phase determination was not possible because of strong multiple scattering and specular reflection in short-lived cloud decks to which the approaches listed in Section 5.7 could not be applied.

An overview of all cloud layers observed during the period from 1997 to 2008 is given in Fig. 7.3. It can be seen that the cloud cases are well distributed over the full time period with slightly less observations between 2003 and 2005 when Earlinet was not funded and the laser failure occurred (see Fig. 7.1).

## 7.2 Geometrical cloud properties

Figure 7.4 shows the distribution of cloud top heights and cloud depths of the identified, well-defined liquid-water and ice-containing clouds. Histograms for intervals of 500 m height and depth are presented. Two modes result from the distributions of the liquid-water and ice-containing clouds. As can be seen, liquid-water clouds with top heights above 6.5 km are rare whereas most ice-containing clouds reached higher. Most of the well-defined liquid-water clouds were geometrically thin with depths of less than 500 m. The lidar was not operated during overcast situations or when the probability for the occurrence of precipitation was given. Therefore, deep cumuliform clouds are missing in the statistics. The second mode in the distributions of cloud top heights and cloud depth is made up by the ice-containing clouds. They feature a wide range of cloud depth reaching from 0.5 to 5.5 km.

A three-modal distribution evolves when the ice-containing clouds are separated into mixed-phase clouds and pure ice clouds. This is shown in Fig. 7.5. Most of the mixed-phase clouds are found between 2 and 8.5 km height. The geometrical depth of these clouds is smaller than 2 km in 80% of all cases. Cloud depths include any virga layers in the case of the ice-containing clouds in Fig. 7.4 and 7.5.

Figure 7.6 is presented to discuss the representativeness of the cloud data set. Cloud abundance is shown. The abundance is defined as the ratio of integrated cloud occurrence time to total measurement time, as a function of height. The curves for the Leipzig lidar station are based on the well-defined clouds and respective information of the cloud base and top height. The black profile shows abundance of all cloud cases (liquid-water and ice-containing) of the Leipzig data set. The blue and red profiles consider only liquid-water and ice-containing clouds, respectively. The green line in Fig. 7.6 shows the cloud abundance based on combined ceilometer-radar observations from 2007 at Lindenberg (52.21° N, 14.12° E). Given the small distance of 150 km from Leipzig, meteorological conditions and atmospheric structure are similar at Lindenberg. The measurements are performed in the framework of the Cloudnet project [Illingworth *et al.*, 2007]. They are run continuously, 365 days a year and data are available online<sup>1</sup>. Cloudnet has the goal to develop a European pilot network of stations for observing cloud profiles and to use recorded data sets for model validation. For comparison, the orange curve shows the cloud abundance profile of data

---

<sup>1</sup>See <http://www.cloud-net.org/> for information and data of Cloudnet.

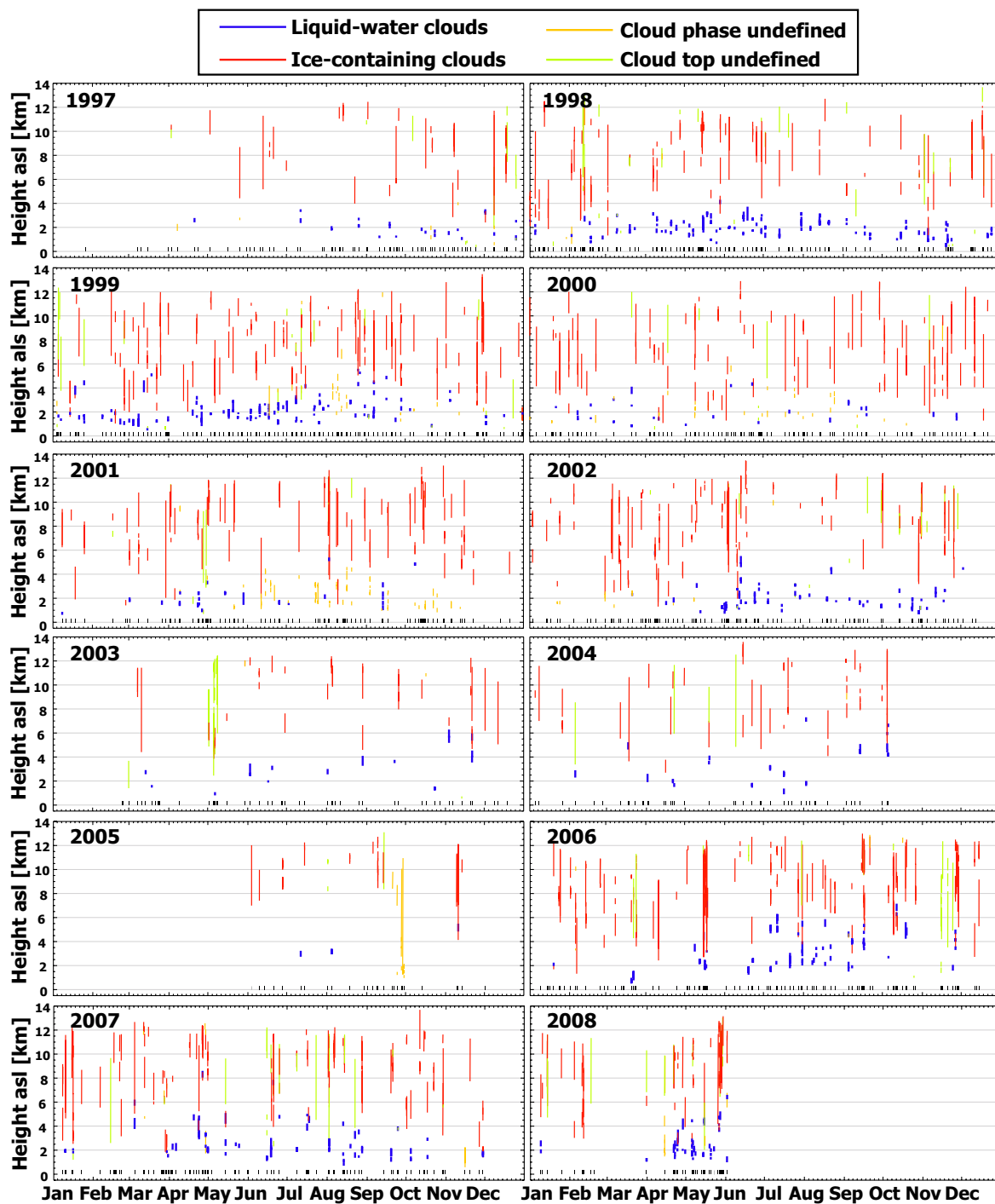


Figure 7.3: Cloud observations between 1997 and 2008. Red: ice-containing clouds, blue: liquid-water clouds, green: undefined cloud top, and orange: undefined cloud phase. Small black bars between 0 and 0.5 km height denote when measurements were performed.

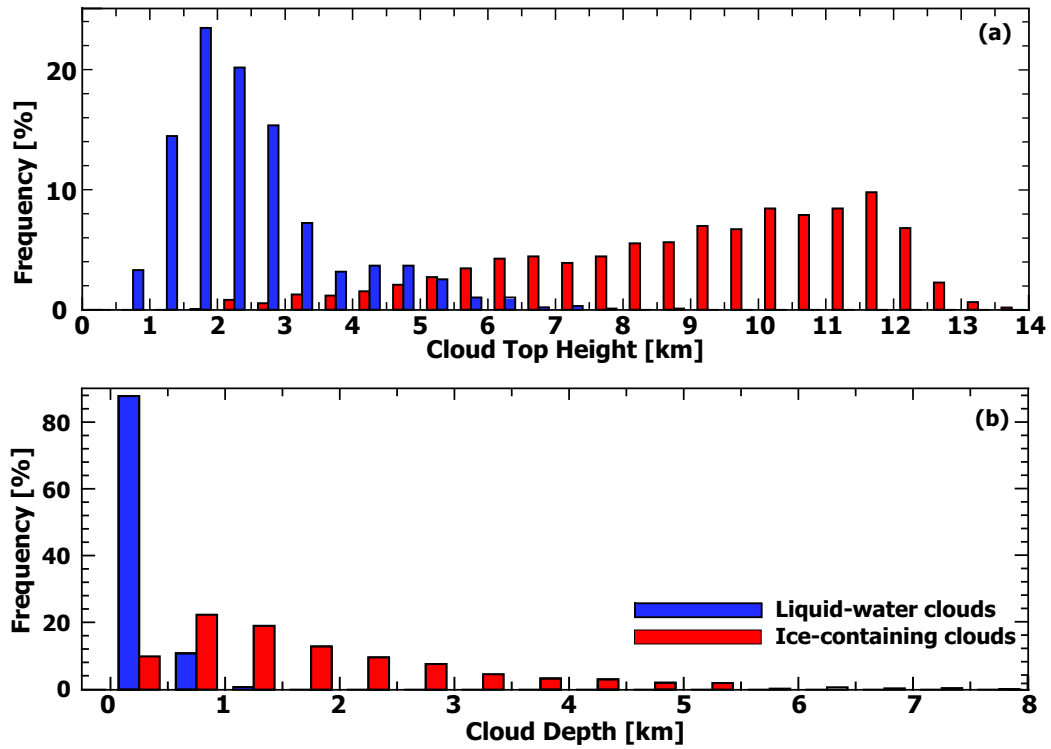


Figure 7.4: Distribution of cloud-top heights (a) and cloud depths (b) of liquid-water clouds (blue) and ice-containing clouds (red). Only well-defined cases are included.

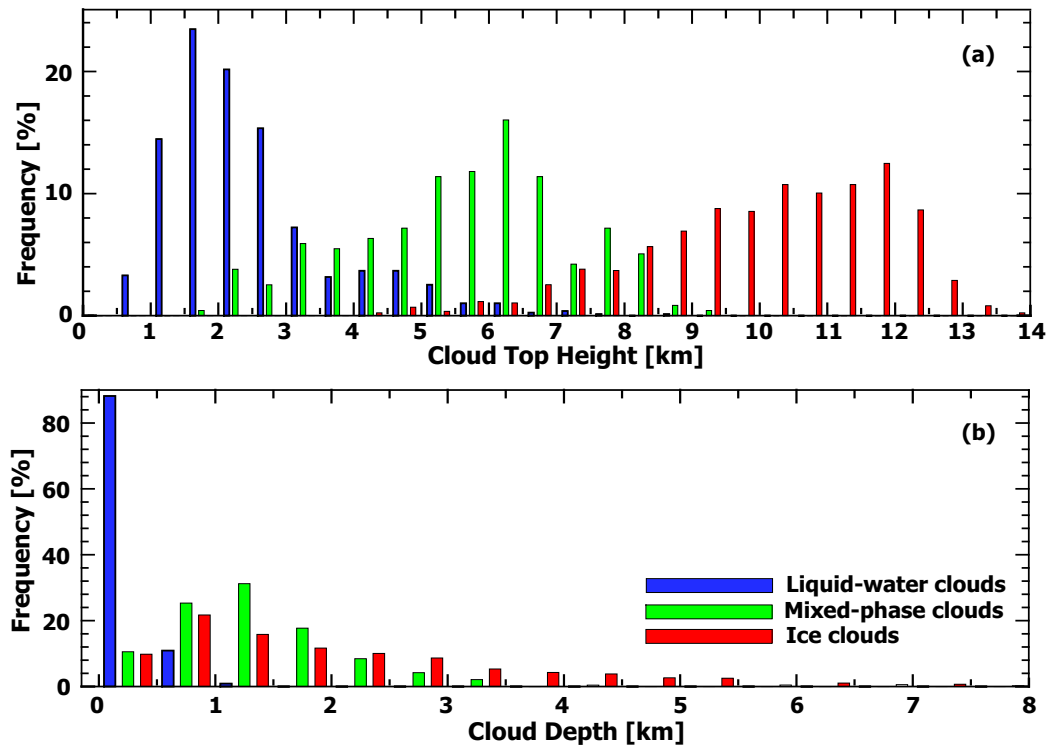


Figure 7.5: Same as Fig. 7.4, except for that three cloud types liquid-water (blue), mixed-phase (green), and pure ice (red) were separated.

from the operational model of the European Centre for Medium-range Weather Forecasts (ECMWF) for Lindenberg obtained for the year 2007.

By comparing the ceilometer-radar-derived cloud abundance profile with the respective one obtained from ECMWF runs for grid point Lindenberg (ECMWF 2007) it can be seen that the observational data provide representative values of cloud abundance for low-level clouds. The deviation from the model-based profile at greater heights indicates the failure of the ceilometer and radar combination to detect all high-level clouds. In contrast, MARTHA obviously detects only 10% of the clouds (3%–4% instead of 30%–40% from the model) at 2 km height. The reason for this discrepancy lies in the sparse availability of measurements during overcast situations. Only above 4 km height a representative picture concerning mid-tropospheric clouds and cirrus up to the tropopause is obtained.

According to the ECMWF model calculations and Lindenberg observations cloud occurrence frequency is high around 2 km and 10 km height. A similar picture is obtained from the Leipzig lidar data set when the observed relative number of cloud cases is analyzed in terms of cloud-top height. This distribution is shown in Fig. 7.7.

Figure 7.8 gives a final overview of cloud top temperatures of all cloud layers observed. Liquid-water clouds accumulate at temperatures above  $-10\text{ }^{\circ}\text{C}$ , solely ice-containing clouds (cirrus) are found for temperatures below  $-40\text{ }^{\circ}\text{C}$ , and mixed-phase clouds mostly occur from  $-10\text{ }^{\circ}\text{C}$  to  $-35\text{ }^{\circ}\text{C}$ . Undefined cases were mostly found in the temperature range above  $-15\text{ }^{\circ}\text{C}$

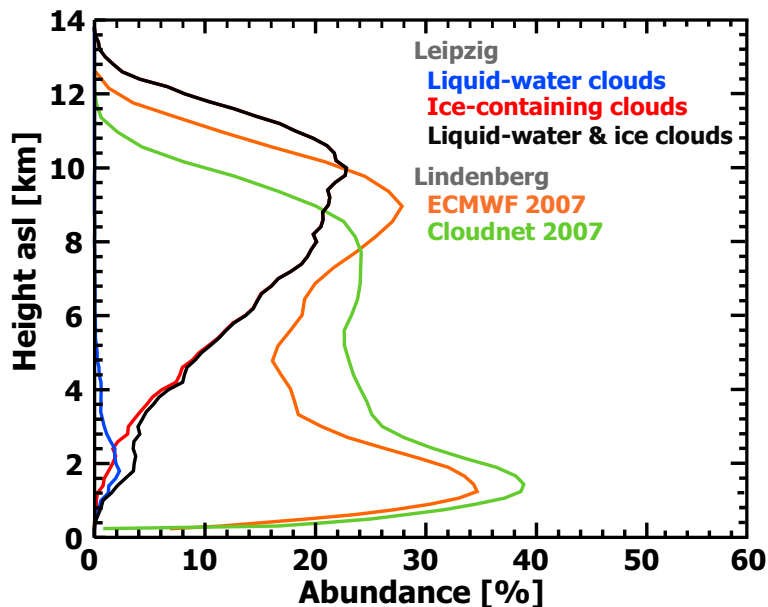


**Figure 7.6:** Cloud abundance, defined as the ratio of integrated cloud occurrence time to total measurement time, as a function of height. The black profile is based on all well-defined cloud cases of the Leipzig data set. The blue and red profiles consider liquid-water and ice-containing clouds, respectively. For comparison, cloud abundance profiles determined from continuous Cloudnet observations (ceilometer and radar; green) and from the ECMWF model output (orange) for Lindenberg in 2007 are shown.

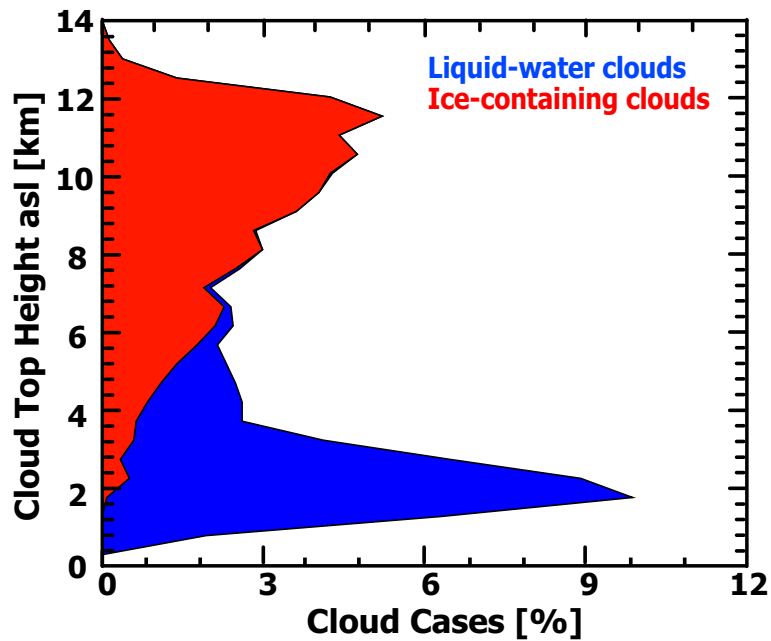


Figure 7.7: Vertical distribution of the cloud top heights of well-defined cloud cases of the Leipzig data set in relative numbers. Integration from 0–14 km height yields 100%. Blue and red areas indicate liquid-water and ice-containing clouds, respectively.

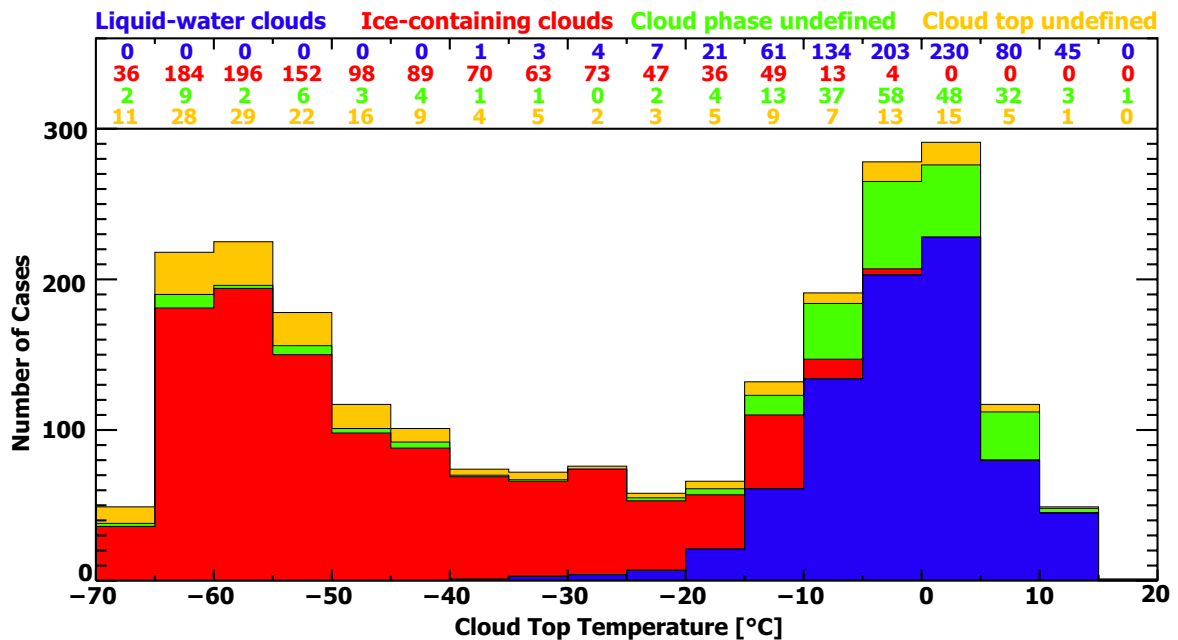


Figure 7.8: Number of liquid-water clouds (blue), ice-containing clouds (red), and clouds for which the phase state (green) or the cloud top height (orange) could not be defined, for temperature intervals of 5 K.

(in 19% of all observed cases). Cloud layers with undefined cloud top height accumulate at temperatures below  $-40$  °C.

### 7.3 Relationship between heterogeneous ice formation and temperature

As the next step in the data analysis the relationship between the amount of ice-containing clouds and cloud top temperature was investigated. The fraction of ice-containing clouds was calculated for cloud top temperature intervals of 5 K. In Fig. 7.9, the black curve shows the fraction of ice-containing clouds for the temperature range between  $-40$  and  $0$  °C. 789 well-defined cloud layers were counted within the given temperature range during the 11-year observational period that was screened for clouds in the framework of the DRIFT project (see Table 7.2). Error bars indicate the standard error  $\sigma$ , i.e., the statistical significance, that depends on the number of observed cloud events  $n$  and the fraction  $f$  of ice-containing clouds according to

$$\sigma = \sqrt{f(1-f)/n}. \quad (7.1)$$

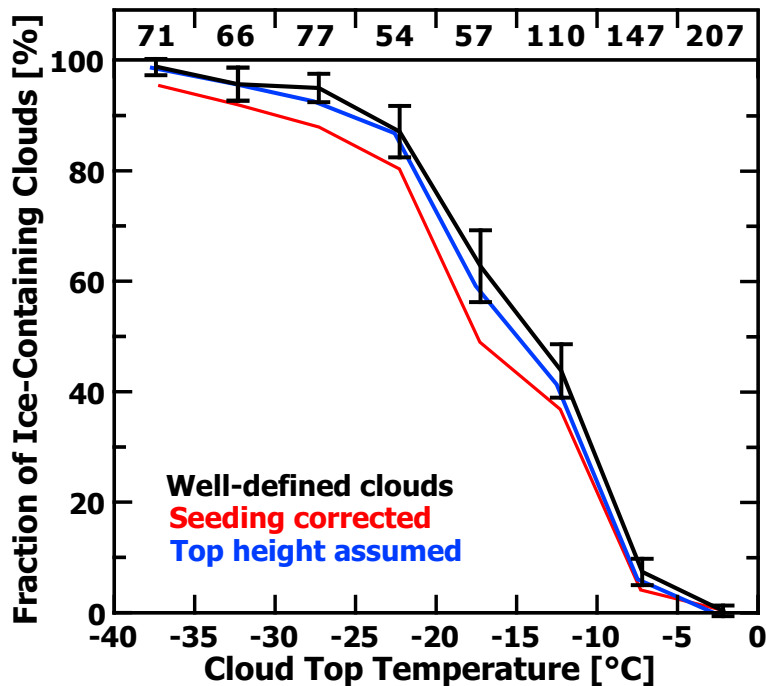


**Figure 7.9:** Frequency of occurrence of ice-containing clouds as a function of cloud top temperature for intervals of 5 K. The black curve shows the distribution for all well-defined clouds of the DRIFT data set. The red curve shows the respective distribution of the seeding-corrected data set. The blue curve is based on the DRIFT data set containing in addition clouds of undefined cloud top with assumed cloud top heights.

The basic feature is the strong increase of the relative number of ice-containing clouds in the temperature range from  $-5$  to  $-25$  °C. The cloud layers that are included in the black curve in Fig. 7.9 are in the following referred to as the DRIFT data set because only these cases are used for further analysis.

The blue and red curves in Fig. 7.9 demonstrate to what extent the study may be biased by excluding cases with undefined cloud top and by neglecting the seeder–feeder effect. The seeder–feeder effect was explained in Section 2.3. Ice crystals of higher, colder clouds can precipitate into lower, warmer liquid–water clouds and grow there significantly [Rutledge and Hobbs, 1983; Ansmann *et al.*, 2009]. New ice crystals are produced only by crystal fragmentation or splintering. The estimation of the potential impact of cloud seeding is complicated. Because of the complex occurrence of cirrus cloud decks, fragments, remnants, and virgae, layered mixed–phase clouds, and virgae originating from the mixed–phase clouds the identification of seeded clouds is difficult. Therefore, any observed cloud scenario in the middle to upper troposphere at temperatures below  $-25$  °C was inspected for potential cloud seeding effects by eye. An ice-containing cloud was counted as a liquid–water cloud in all cases in which a higher cloud layer or an ice virga was sufficiently close to the lower ice-containing cloud layer of interest. In such a case it was simply assumed that the ice in the lower cloud is caused by seeding from above. For temperatures above  $-25$  °C, a more objective method was applied. Here, any ice-containing cloud was counted as liquid–water cloud when the distance between the cloud top and the base of the overlying ice-containing cloud was less than one kilometer. The effect of this correction on the cloud statistics is shown in the red curve in Fig. 7.9. The correction leads to a reduction in the fraction of ice-containing clouds by, on average, 10%. Because the effect is small and the uncertainty of this rough estimation is of the same order of magnitude, cloud seeding effects in the DRIFT data set are ignored in the further discussion.

As discussed in Section 7.1, clouds for which the cloud top height could not be determined are excluded from the well–defined DRIFT data set. This may lead to an overestimation of the fraction of ice-containing clouds in the lower and middle troposphere because the cloud top could often not be determined for optically thick water clouds. In order to check for the possible effect of the exclusion of clouds with undefined tops on the DRIFT data set the top heights were assumed for these clouds. For liquid–water clouds the apparent top height, i.e., the height at which the signal dropped below the signal received at cloud base (see Section 5.1), was increased by 1 km and for ice-containing clouds by 2 km. This correction lowers the corresponding cloud top temperatures by about 6.5 K and 13 K, respectively, taking wet–adiabatic cooling into account [Liljequist and Cehak, 2006]. Adding the clouds with assumed top heights and temperatures to the DRIFT data set yields the blue curve in Fig. 7.9. The number of liquid–water clouds slightly increases in the temperature range from  $-5$  to  $-25$  °C, so that the fraction of ice-containing clouds between  $-5$  to  $-25$  °C decreases by approximately 5%. Apparently, the exclusion of clouds with undefined top height from the DRIFT data set affects the distribution of ice-containing and liquid–water clouds only marginally.

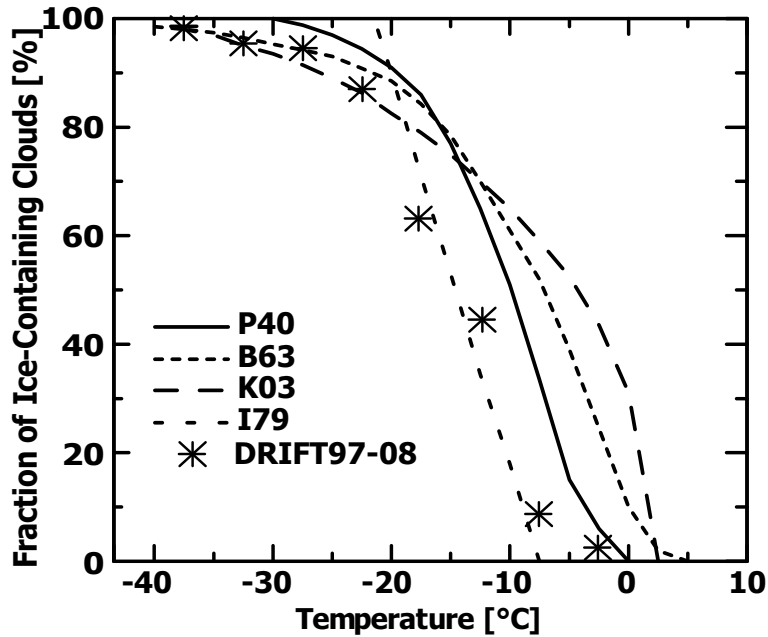


**Figure 7.10:** Comparison of the DRIFT observations with airborne *in situ* measurements at different mid-latitude sites (data are taken from Fig. 14 of Korolev *et al.* [2003]). Cloud observations of Pepler [1940] (P40), Borovikov *et al.* [1963] (B63), Isaac and Schemenauer [1979] (I79), and Korolev *et al.* [2003] (K03) are considered. The airborne observations are related to temperatures at flight level, whereas the lidar results are given as a function of cloud top temperature.

In Fig. 7.10 the DRIFT cloud observations are compared with other field observations (airborne *in situ* measurements) to check the representativeness of the derived relationship between ice formation and temperature. The airborne observations were conducted in Germany (P40, 180 km northeast of Leipzig) [Pepler, 1940], in the former USSR (B63) [Borovikov *et al.*, 1963], Canada (I79) [Isaac and Schemenauer, 1979], and at different sites in North America (K03, 42° N to 76° N) [Korolev *et al.*, 2003] between about 1930 and 2000. The curves P40 and B63 in Fig. 7.10 are based on 9000 impactor samplings. All samples that showed no ice crystals were counted as liquid-water clouds. The bulk of the K03 data are sampled in stratiform clouds. The I79 data were recorded in convective clouds. The agreement of the *in situ* field studies and the lidar observations is good considering that the airborne observations are related to ambient temperatures at flight level, and the lidar results are related to cloud top temperature. The cloud top temperature can be about 2 to 6 K lower for clouds with depths of 200 to 1000 m, and even lower for thicker cumulus clouds. Furthermore, the lidar is not sensitive enough to identify a few crystals in an environment dominated by water drops. Only if significant ice production occurs, the cloud is counted as an ice-containing cloud. This may in part explain the shift of the lidar-derived curve in Fig. 7.10 towards lower temperatures.

## 7.4 Impact of Saharan dust on heterogeneous ice nucleation

This section presents the investigations regarding the key question of this study: Is there an observational evidence for the influence of Saharan dust on the ice nucleation temperature in clouds? To answer this important question, several attempts were undertaken. In Section 7.4.1, results of a backward-trajectory cluster analysis are discussed. Clouds that formed in dust-free north-Atlantic air masses are compared with clouds that formed in air that may have contained dust according to the cluster analysis. In the second and third approach DREAM calculations of the column dust load and of the dust concentration at cloud level, respectively, were used to separate dust-free from dust-laden air masses. Results concerning these investigations are presented in Section 7.4.2.

The motivation to study the role of Saharan dust as IN by means of three different approaches was to investigate and to take into account potential limits or advantages of each of them. Trajectory cluster analysis is a practical method for the determination of main source regions of air masses for a high number of trajectories that arrived at a specific destination. The classification of the source region is usually followed by the investigation of relationships between parameters measured at the destination and typical characteristics associated to the source region that belongs to the backward trajectory calculated at the time of measurement. In the scope of this work the determination of the origin of the cloud-embedding air mass by a backward-trajectory cluster analysis is probably the simplest approach to separate the clouds observed over Leipzig into dust-free and dust-laden fractions. However, it is a frequently applied tool. Previous studies dealt, e.g., with the relationship between the measurement of trace gases [Cape *et al.*, 2000] or of optical aerosol properties [Wandinger *et al.*, 2004] and the origin of the associated air mass. Also the availability of unprocessed mineral dust for interactions with clouds was recently investigated by using forward-trajectory calculations [Wiacek and Peter, 2009]. The accuracy of air-mass source regions determined from backward trajectories may be limited because it can not be excluded that the air mass interfered with other air masses during transport, even at times earlier than the starting point of the backward-trajectory calculation. Consequently, properties measured in an air mass at a destination point may not be exclusively related to the air mass properties at the trajectory starting position.

Therefore, if possible, it should be aspired to correlate only parameters that are obtained at the same location. In the case of this work these parameters are the cloud properties, e.g., cloud hydrometeor thermodynamic state, and the information on the dust load at and above Leipzig. The incorporation of DREAM data to separate dust-free from dust-laden clouds is likely to perform better than the separation by the trajectory cluster analysis. The trajectory-based approach separates dust-laden from dust-free cloud layers by examining whether a backward trajectory crossed desert areas or not. DREAM is optimized to accurately model dust dispersion, diffusion, and dry as well as wet deposition of mineral dust (see Section 5.3). Such information is available either vertically resolved or in the form of column values. Relating vertically-resolved data, as it is the case for the DRIFT cloud data set, to column-based parameters, as the column dust load provided by DREAM, may yield ambigu-

---

ous results. *Feingold et al.* [2003] stated that it is unclear to what extent column-integrated aerosol properties are representative of the aerosol entering clouds which may not be located within any aerosol layer. Nevertheless, similar studies were done before. Frequently, column parameters like aerosol optical depth measured with space-borne or ground-based passive remote sensors were correlated with passively measured microphysical cloud properties [*Quaas et al.*, 2004; *Kaufman et al.*, 2005; *Ou et al.*, 2009], even though it could not be ensured that the clouds were embedded in aerosol layers. However, best conditions for a correlative study as it was performed in the scope of this work should be given when the vertically resolved cloud data is compared with the corresponding vertical profiles of the dust distribution provided by DREAM.

### 7.4.1 Trajectory cluster analysis

In the scope of this study the offline version of HYSPLIT 4.8 was used to calculate 5-day analytical backward trajectories for the layer mean height of every observed cloud layer on the basis of the FNL and GDAS1 data sets. The description of the trajectory calculation process and of the clustering algorithm was given in Section 5.3. The cluster analysis was performed with the 72-hour backward trajectories of 753 well-defined cloud layers with cloud top temperatures between  $-40$  and  $0$  °C. For 36 well-defined cloud layers in this temperature range backward trajectories could not be calculated because of missing FNL or GDAS1 data.

During the analysis of the case studies that were discussed in Chapter 6 indications were found that the HYSPLIT backward trajectories did not pass the African continent when high dust loads were detected at the trajectory endpoints. An example for such a case was shown in Fig. 6.1. Therefore, as a first approach, it was decided to use southerly and southwesterly trajectories as indicators for dust-laden clouds. Cloud layers whose trajectories originated over the open Atlantic Ocean and approached Leipzig from northwesterly directions were assigned to be dust-free cases. The corresponding air masses are in general of low aerosol load and optically thin [*Wandinger et al.*, 2004].

Twelve main flow patterns were determined by the clustering algorithm. They are shown in Fig. 7.11. All backward trajectories which were compiled in one cluster are shown in black and their number is given for each cluster. Green, red, and blue colors indicate dust-free, dust-laden, and unspecified air masses, respectively. The two clusters in the upper left domain of Fig. 7.11 contain the trajectories for which the corresponding cloud layers were categorized as dust-laden clouds. According to the HYSPLIT calculations the air masses of the clouds in these two clusters passed the African continent or passed by closely within the 72 hours of the trajectory traveling time. The blue-flagged clusters are not indicative neither for dust-laden nor for dust-free clouds. The trajectories contained in these clusters spent most of their occurrence time over the European landmass. Mixing with continental aerosols as forest fire smoke or industrial pollution are likely for these cases which negates the use of the corresponding cloud layers for both dust-free and dust-laden scenarios. Trajectories of the five green clusters spent most of their occurrence time over the ocean. Contamination of the air masses with aerosol concentrations far above background values is unlikely in these

---

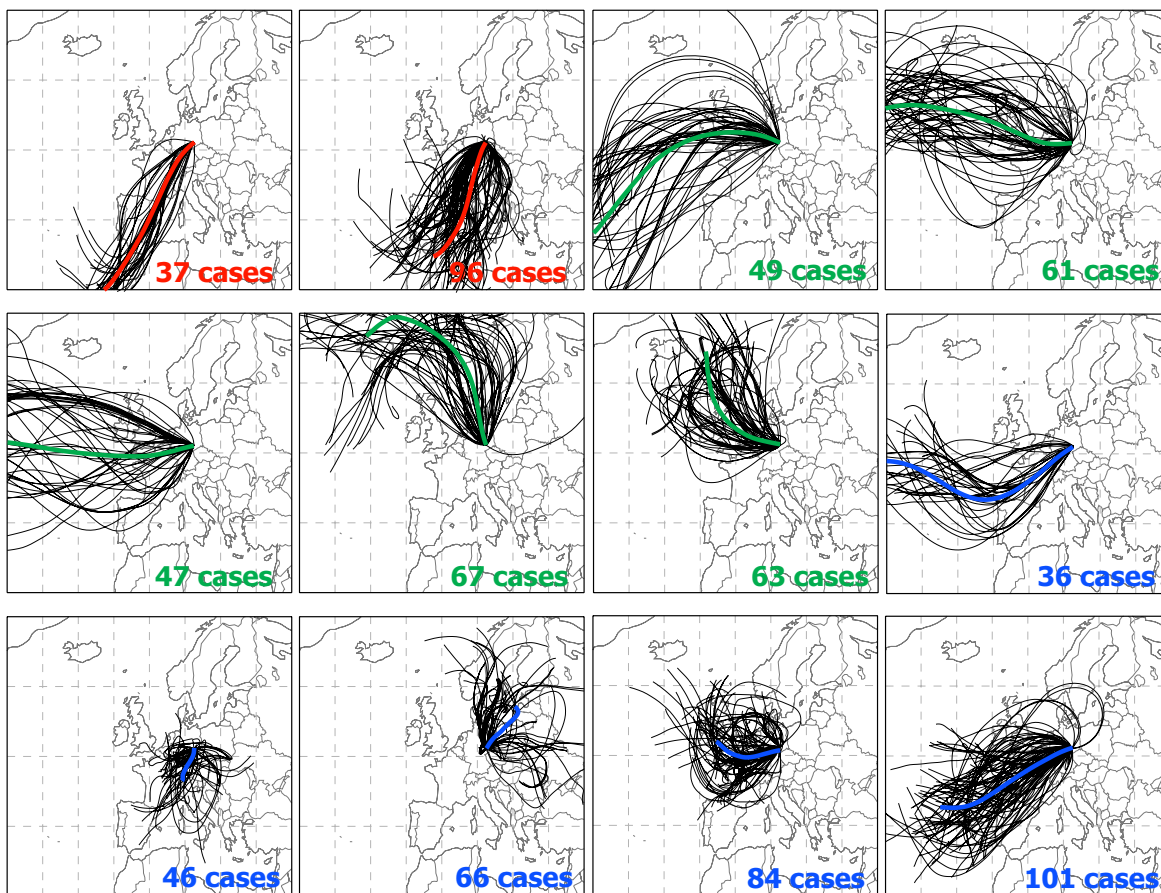


**Figure 7.11:** Trajectory cluster analysis performed with 753 trajectories. Red: dust-laden clusters, green: dust-free clusters, and blue: unspecified clusters. Thin black lines: Trajectories contained in each cluster. Thick solid lines indicate the mean trajectories of the respective cluster. Numbers denote the amount of trajectories contained in each cluster.

cases. For further analysis 125 dust-laden and 289 dust-free cloud layers were found.

Figure 7.12 shows the fraction of ice-containing dust-laden clouds (red curve) and dust-free clouds (green curve) for temperature intervals of 5 K. Both curves show a similar behavior as the one based on the full DRIFT data set (black curve). Down to temperatures of  $-20^{\circ}\text{C}$  the curve for the dust-laden air masses shows slightly higher fractions of ice-containing clouds than the curve for the dust-free clusters. A pronounced deviation between the two curves is, however, not given. In addition, the small number of dust-laden cloud cases introduces relatively large error bars. Therefore, a definite conclusion concerning the influence of Saharan dust on the freezing temperature of clouds cannot be drawn from Fig. 7.12.

#### 7.4.2 Dust-model-based investigations

An improved and more accurate separation of dust-laden and dust-free air masses and embedded cloud layers is expected when using data of DREAM. As mentioned in Section 5.3,

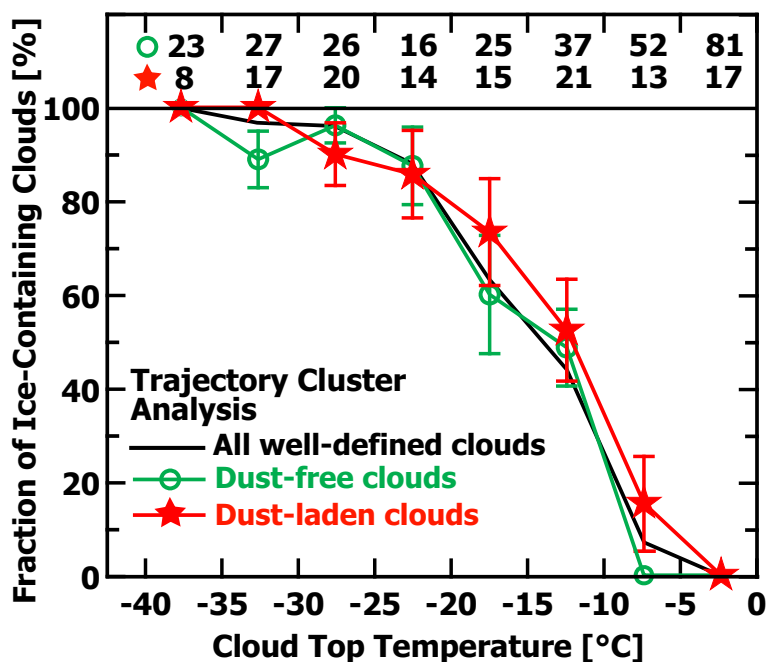


**Figure 7.12:** Frequency of occurrence of ice-containing clouds as a function of cloud top temperature (5 K intervals) for clouds from the dust-free clusters (green, open circles) and clouds which belong to the dust-laden clusters shown in Fig. 7.11 (red, closed stars). The error bars represent the standard error [see Eq. (7.1)]. The number of cases in each temperature interval are shown in the top area of the figure.

DREAM was explicitly developed to accurately model the spatial and temporal distribution of mineral dust including the prediction of dust outbreaks.

DREAM calculations of the vertical dust distribution and of the column dust load for the grid point of Leipzig cover the full time period of lidar observations at Leipzig with 12-hourly resolution. Therefore, cloud observations can be classified as dust-laden cases either by means of column dust load or by means of dust concentration at cloud height. Both approaches are investigated in the following.

### Cloud separation based on DREAM column dust load

First, Fig. 7.13 provides an overview of the frequency and strength of dust events over Leipzig. Time series of the column dust load above Leipzig from 1997 to June 2008 are shown. From the distribution of the peaks of the dust load it can be seen that major Saharan dust outbreaks (with dust load larger than  $0.2 \text{ g m}^{-2}$ ) occur 1–6 times per year. The green-colored sections in the horizontal bars below the time series indicate dust-free conditions with a column dust load of below  $0.001 \text{ g m}^{-2}$  which is the lowest level that is given in the output of DREAM. A well distributed separation of dust-laden from dust-free scenarios is obtained for a threshold of  $0.02 \text{ g m}^{-2}$ . Days for which this threshold was exceeded are colored red in the horizontal bars in Fig. 7.13. For higher thresholds the number of dust-laden periods decreases strongly and clouds that formed under potentially dust-laden

conditions would consequently be left out from further analysis. The resulting yearly and total number of days with dust-free and dust-laden conditions and corresponding numbers of observed dust-free and dust-laden cloud layers that were found in the DRIFT data set by applying the above-mentioned thresholds are listed in Table 7.3. 220 dust-laden clouds were found that formed in air masses with a dust load above the threshold of  $0.02 \text{ g m}^{-2}$ , whereas 321 clouds formed in dust-free air masses with a dust load of below  $0.001 \text{ g m}^{-2}$ . For the remaining 248 cloud layers intermediate conditions were found. These layers were excluded from further analysis. Two case studies, one representing the African air masses (high dust load) and one observation representing dust-free conditions (North-atlantic air) were presented in Sections 6.1 and 6.2, respectively.

Before the DREAM data are analyzed with respect to the occurrence of ice-containing clouds in dust-laden and dust-free air, Figure 7.14 is presented to illustrate the consistency between the HYSPLIT backward trajectory data set and the DREAM data set. HYSPLIT backward trajectories for all clouds that formed in dust-free and dust-laden air according to the DREAM dust-load criterion are shown. The comparison with Fig. 7.11 indicates similar flow patterns of the dust-laden air masses identified by using HYSPLIT and by applying the DREAM dust-load criterion. The majority of the backward trajectories of the 220 dust-laden clouds arrived at Leipzig from southwesterly directions which is the prevalent flow pattern when high dust loads are observed at Leipzig. However, among the dust-laden clouds that were derived applying the dust-load criterion, there are many HYSPLIT trajectories that never came close to the African continent even though the respective air mass contained dust loads above the DREAM threshold value of  $0.02 \text{ g m}^{-2}$  for dust-laden air. According to the HYSPLIT trajectories, some dust-laden air masses apparently originated over the subtropical North Atlantic from areas of the Saharan dust long-range transport regime between Africa and the Caribbean [*Liu et al.*, 2008]. Some backward trajectories of dust-laden clouds approached Leipzig from easterly directions. Probably, in these cases dust was transported from the Sahara, over western Asia, and then back to central Europe. The backward-trajectory travel time of 72 hours that was used in the clustering algorithm apparently was too short to identify the Saharan desert as source region in these cases of long-range transport. In addition, also the error of the trajectory calculation that is based on data with  $1^\circ$  horizontal resolution is likely to increase with increasing trajectory travel time.

The backward trajectories of the dust-free cloud cases derived from the cluster analysis and DREAM dust-load data show a comparable prevailing flow pattern. Most of the green trajectories (Fig. 7.14) arrive from western and northwestern to northeastern directions. The majority of the dust-free clouds in the dust-load approach are also contained in the dust-free sample of the cluster analysis. With 321 cloud layers that were identified applying the dust-load criterion, 10% more dust-free cloud cases were derived compared to the cluster analysis. It is likely that some of the backward trajectories from the unspecified clusters in Fig. 7.11 are included in the data set derived from the DREAM dust load criterion. Backward trajectories of some clouds that were classified as dust-free from the DREAM dust load even

---

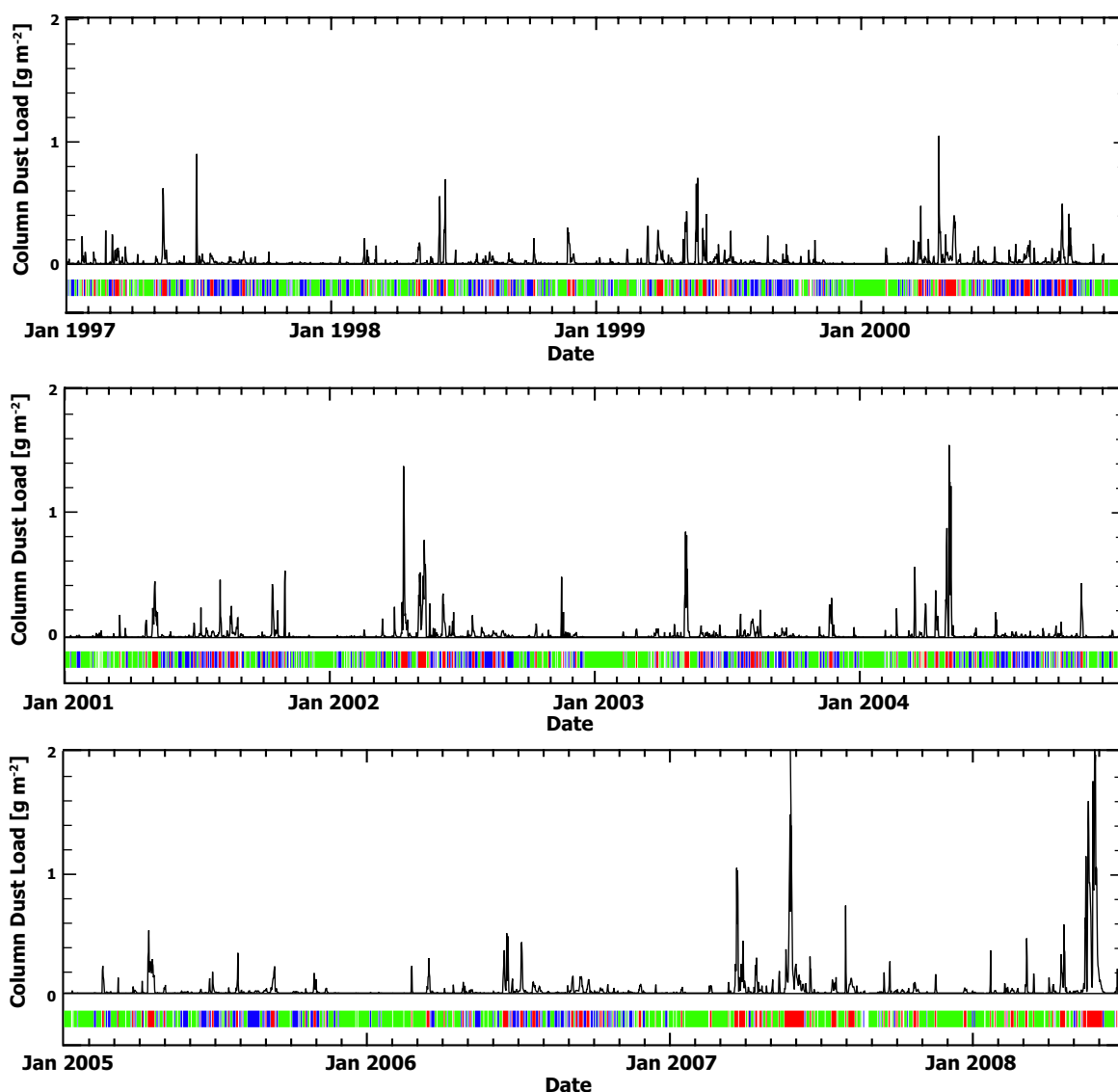


**Figure 7.13:** Column dust load above Leipzig for the years 1997 to 2008 computed with DREAM. The colored line shows episodes of dust-laden (dust load above  $0.02 \text{ g m}^{-2}$ , red), dust-free (dust load below  $0.001 \text{ g m}^{-2}$ , green), and intermediate conditions (blue). White sections refer to episodes for which no DREAM data were available. Dust-laden and dust-free conditions occurred during 24% and 47% of the time, respectively.

passed northern Africa. Apparently, these air masses crossed the desert at high altitudes so that a mixing with dust did not occur.

Figure 7.15 shows the temperature dependence of the occurrence of ice-containing clouds separately for dust-free and dust-laden air masses when the DREAM dust-load criterion is applied. In comparison to Fig. 7.12, the fraction of ice-containing clouds between 0 and  $-20 \text{ }^\circ\text{C}$  decreased for the dust-free data set. This can be explained by a more accurate identification of dust-free cloud layers when the DREAM data were used for the separation,

**Table 7.3:** Number of days and observed cloud layers per year at grid point Leipzig for which DREAM computed dust-laden conditions (dust load larger than  $0.02 \text{ g m}^{-2}$ ) and dust-free conditions (dust load below  $0.001 \text{ g m}^{-2}$ ), respectively.

Year	Dust-laden conditions		Dust-free conditions	
	days	clouds	days	clouds
1997	72	0	135	13
1998	72	18	161	101
1999	86	21	130	51
2000	103	16	131	33
2001	72	19	162	23
2002	87	14	133	36
2003	78	10	163	8
2004	60	7	165	3
2005	52	0	169	4
2006	81	43	153	9
2007	116	36	216	32
2008	70	36	100	8
Total	949	220	1818	321

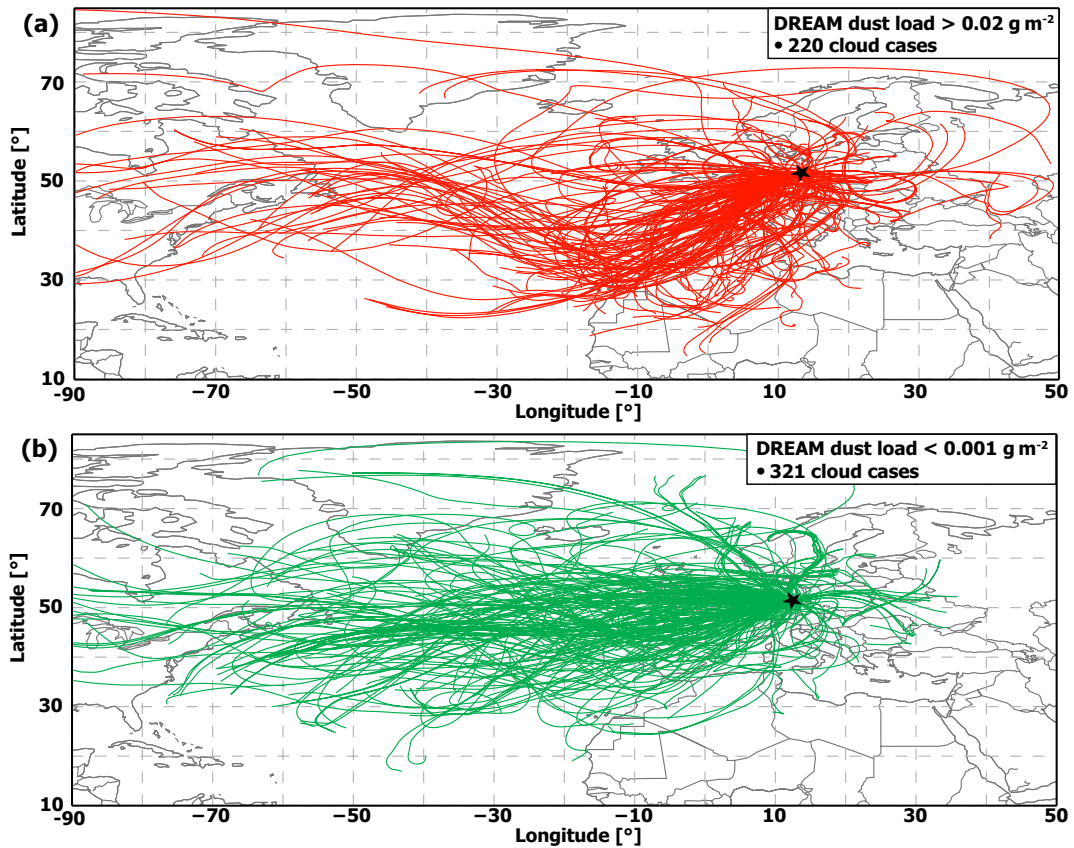


**Figure 7.14:** HYSPLIT backward trajectories for all clouds that formed (a) in dust-laden air masses according to the DREAM column dust load, and (b) for all clouds that formed in dust-free air masses according to the DREAM column dust load. The star marks the location of the trajectory end point Leipzig.

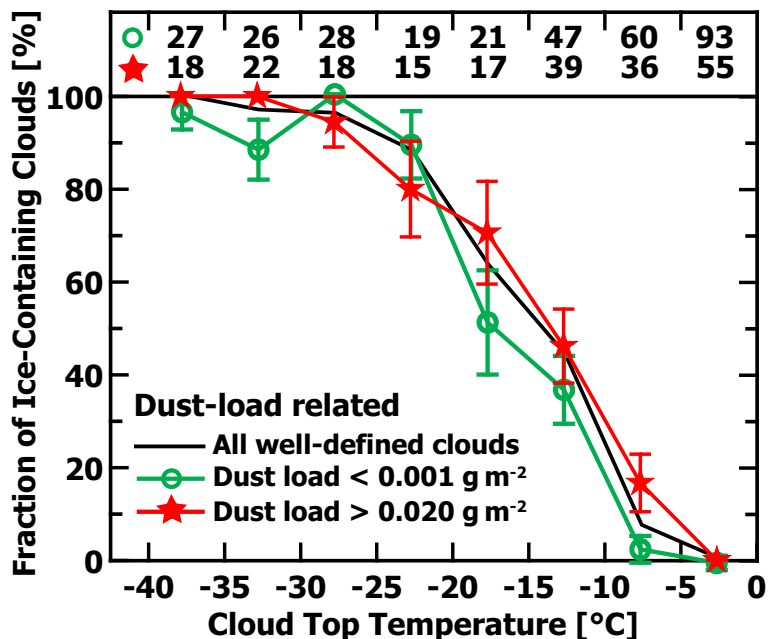


**Figure 7.15:** Frequency of occurrence of ice-containing clouds as a function of cloud top temperature (5 K intervals) for clouds which formed in dust-free air with column dust load of below  $0.001 \text{ g m}^{-2}$  (green, open circles) and in dust-laden air with column dust load larger than  $0.02 \text{ g m}^{-2}$  (red, closed stars), respectively. Error bars indicate the standard error [see Eq. (7.1)]. The number of cases in each temperature interval are shown in the top area of the figure.

even though only columnar values were used for the identification of dusty scenarios. The fraction of ice-containing clouds from the dust-laden data set is similar to the one of the cluster analysis. Only a weak correlation between an increased dust load and the fraction of ice-containing clouds is obtained.

### Cloud separation based on DREAM dust concentration at cloud level

The less pronounced dust-related ice formation that was found from the trajectory cluster analysis (see Fig. 7.12) and the dust-load-related cloud separation (see Fig. 7.15) may be explained by the missing information about the vertical dust distribution. Even during strong dust outbreaks the dust may be concentrated in detached layers. Clouds outside of these layers would not be affected by the dust. Therefore, in the next step, the data set was separated into dust-laden and dust-free clouds by means of the dust concentration at cloud level. For the identification of a dust-laden cloud, the maximum dust concentration within 500 m of the cloud boundaries must exceed a threshold value of  $2 \mu\text{g m}^{-3}$ . Dust-free clouds are characterized by a maximum dust concentration of below  $0.001 \mu\text{g m}^{-3}$  within 500 m of the cloud. This value again corresponds to the lowest output level of DREAM. If the entire troposphere (0–10 km height) would be loaded with a dust concentration of  $2 \mu\text{g m}^{-3}$ , the column value would yield  $0.02 \text{ g m}^{-2}$ .

Figure 7.16 shows the HYSPLIT backward trajectories of the identified dust-laden and dust-free clouds. 218 layers were identified as dust-laden clouds and 213 cloud layers did

not show any dust within 500 m of the cloud boundaries. The comparison of Fig. 7.16 with Fig. 7.14 reveals that no dust-free backward trajectories passed northern Africa or the Mediterranean when the data set was separated according to the DREAM dust concentration. The number of dust-free clouds decreased by 108 in the dust-concentration-related data set. The found difference in the number of dust-free clouds is owed to the fact that for this study the output of the DREAM dust load was available with an accuracy of only 3 digits. A dust load of below  $0.001 \text{ g m}^{-2}$  is given as  $0.000 \text{ g m}^{-2}$ . Therefore, when small traces of dust are calculated in the vertical profile of the dust concentration, the column-integrated dust concentration, i.e., the dust load, may still be below  $0.001 \text{ g m}^{-2}$ . With 218 vs 220 cloud cases, the number of dust-laden clouds is about the same as for the dust-load-related data set. However, the members of each sample may in part be different ones because high column dust loads are not necessarily related to high dust concentrations at cloud level.

Figure 7.17 shows the temperature dependence of the occurrence of ice-containing clouds separately for air masses that are dust-free and dust-laden, respectively, according to the dust-concentration at cloud level. As can be seen, the difference between the curves of the dust-laden and the dust-free air masses increased. A considerably enhanced fraction of ice-containing clouds is now observed in Saharan air masses in the temperature range from  $-5 \text{ }^\circ\text{C}$

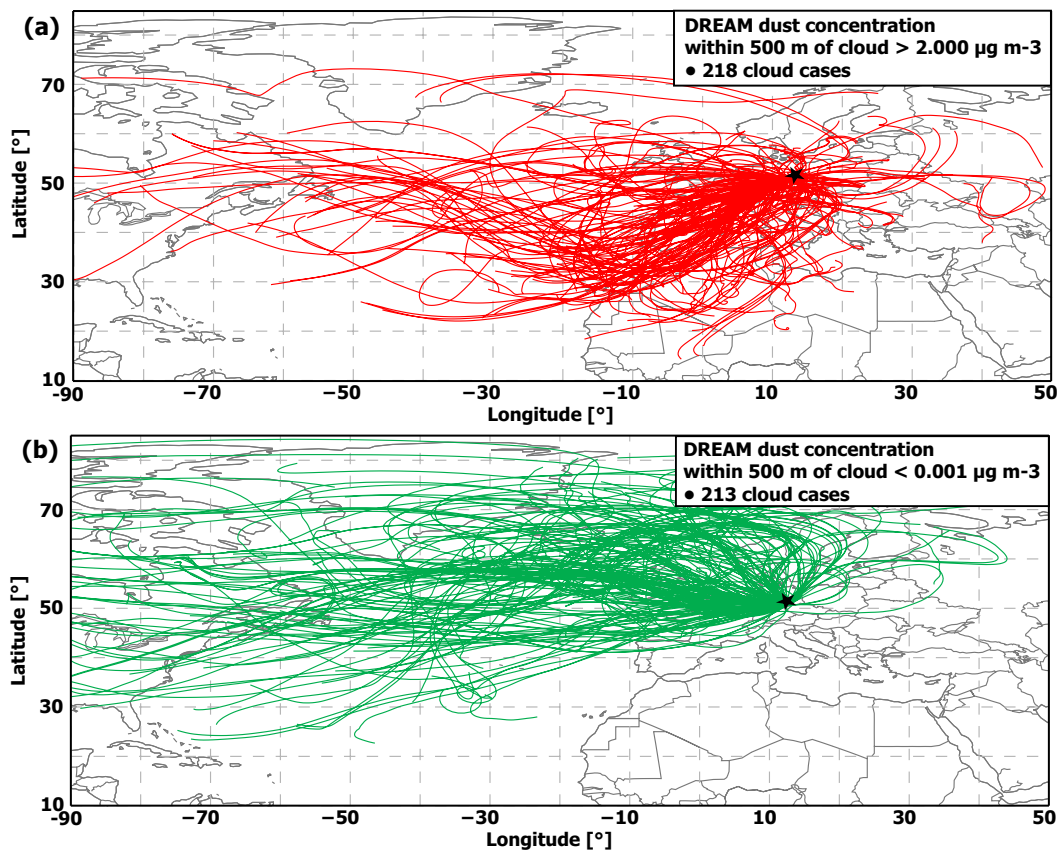


**Figure 7.16:** HYSPLIT backward trajectories for all clouds that formed (a) in dust-laden air masses and (b) in dust-free air masses according to the DREAM dust concentration. The star marks the location of the trajectory end point Leipzig.

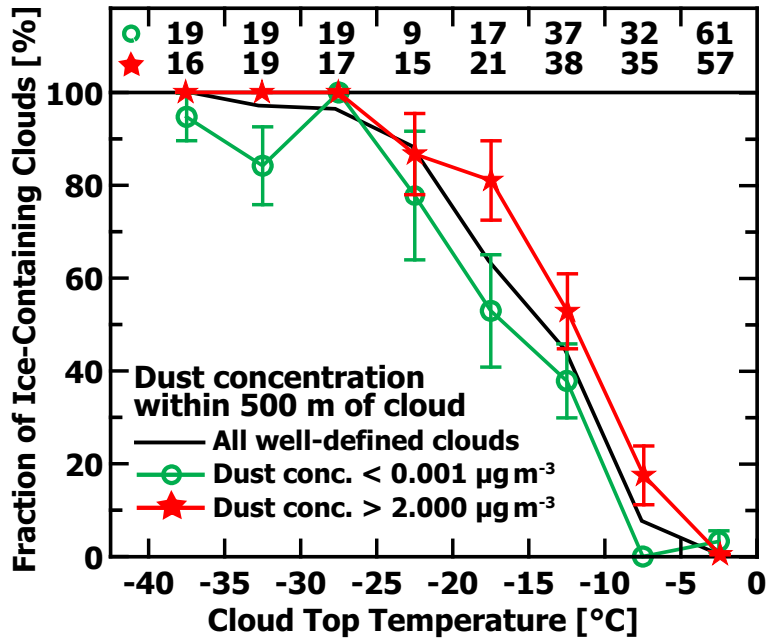


**Figure 7.17:** Frequency of occurrence of ice-containing clouds as a function of cloud top temperature (5 K intervals) for clouds which formed in dust-free air (green, open circles) and which formed in dust-laden air (red, closed stars) with a maximum dust concentration within 500 m of the cloud boundaries of below  $0.001 \mu\text{g m}^{-3}$  and of above  $2 \mu\text{g m}^{-3}$ , respectively. Error bars indicate the standard error [see Eq. (7.1)]. The number of cases in each temperature interval are shown in the top area of the figure.

to  $-20^\circ\text{C}$ . In turn, the dust-free data set shows a decreased fraction of ice-containing clouds in this temperature range compared to Fig. 7.15. About 20% to 30% more ice-containing clouds occur in dust-laden air in the temperature range from  $-5$  to  $-20^\circ\text{C}$ . The fraction increases from 38% to 53% at  $-10$  to  $-15^\circ\text{C}$  and from 50% to 81% at  $-15$  to  $-20^\circ\text{C}$  and thus by a factor of 1.6.

## 7.5 Discussion

The presented study of the occurrence of ice-containing clouds as a function of cloud top temperature corroborates the hypothesis that Saharan dust particles are effective ice nuclei. The 789 cloud cases contained in the DRIFT data set were separated into dust-free and dust-laden subsamples by means of three different approaches. Each of these, a trajectory cluster analysis and the separation based on DREAM column dust load and dust concentration at cloud level, respectively, showed that the fraction of dust-laden ice-containing clouds increases in the temperature range from  $-5^\circ\text{C}$  to  $-20^\circ\text{C}$  compared to the observations in dust-free air. Possible ambiguities in the identification of dust-laden from dust-free clouds evolve when the data set is separated by the trajectory cluster analyses and the DREAM column dust load, respectively. These approaches are only passive indicators for dust-laden or dust-free scenarios, because they do not contain information about the actual dust con-

centration at cloud level. The separation according to the DREAM dust concentration at cloud level revealed the strongest indications for an influence of Saharan dust on the temperature of heterogeneous nucleation. Nevertheless, even though DREAM is optimized for dust transport modeling, the calculated parameters are subject to uncertainties. Potential errors in the modeled dust load and dust concentration emerge from the imperfect knowledge of the starting conditions needed for model initialization and implemented parameterizations. Both of these effects affect any model. However, as mentioned in Section 5.3, DREAM demonstrated high accuracy during comparisons with observations.

The comparison shown in Fig. 7.17 suggests that dust particles are not activated as IN at temperatures above  $-5$  °C. At temperatures below  $-20$  to  $-25$  °C there may generally be enough dust and non-dust IN to initiate ice formation by heterogeneous nucleation. In the temperature range from  $-5$  to  $-20$  °C, where mixed-phase clouds dominate, dust is obviously playing a major role. Given this strong impact of mineral dust on ice formation the question arises whether other or additional processes have contributed to the observed differences between the observations in dust-free and dust-laden air masses.

It cannot be excluded that the meteorological conditions were different in the different air mass types. Stronger turbulent and convective motions in the subtropical, dust-enriched air masses may have led to enhanced upward and downward motions and entrainment of dry environmental air into the clouds. Such processes could have contributed to the observed differences. This impact should however be also visible in the geometrical properties of the detected clouds. Table 7.4 lists the mean cloud depth and corresponding standard deviation of dust-free and dust-laden liquid-water and ice-containing clouds when the DRIFT data set (clouds with top temperatures between  $-40$  and  $0$  °C) is separated according to the DREAM dust concentration. With values of  $0.35 \pm 0.16$  km and  $0.37 \pm 0.17$  km, respectively, the mean depth is similar for the dust-laden and dust-free liquid-water clouds. Standard deviations are large indicating that the cloud depth varies strongly from case to case. Mean depths of ice-containing dust-free and dust-laden clouds are  $1.39 \pm 0.77$  km and  $1.61 \pm 0.92$  km, respectively. The ice-containing dust-laden clouds appear on average slightly thicker compared to the dust-free clouds, but standard deviations are large. Probably virga production increases under dust-laden conditions, leading to increased cloud depths. Because of the similar cloud

**Table 7.4:** Mean cloud depth and corresponding standard deviation of dust-free and dust-laden liquid-water and ice-containing clouds with cloud top temperatures between  $-40$  and  $0$  °C. The clouds were separated according to the thresholds of the DREAM dust concentration.

Cloud Type	Mean Cloud Depth [km]	Std. Dev. [km]
<b>Dust-free</b>		
Liquid water	0.35	0.16
Ice-containing	1.39	0.77
<b>Dust-laden</b>		
Liquid water	0.37	0.17
Ice-containing	1.61	0.92

depths for the different data sets it appears to be not very likely that meteorological aspects had a strong impact on the found differences.

Similarities of the backward trajectories in Fig. 7.14 and 7.16 support this assumption. The backward trajectories of the dust-laden clouds arrive from various directions. Not only southwesterly flows contribute to these data sets. Many trajectories arrived at Leipzig from the western and northwestern Atlantic Ocean. In turn, dust-free cloud cases also showed trajectories coming directly from southern and southwestern Europe. The main flow patterns of the backward trajectories did also not vary between the clouds that were categorized according to dust load or to dust concentration.

Another opportunity to discuss the possible influence of meteorological, geographical and aerosol-related effects on the fraction of ice-containing clouds as a function of height or temperature is the comparison of the DRIFT results with similar ones obtained during the SAMUM-2 campaign performed in the tropics at Cape Verde (14.9° N, 23.5° W) in 2008 [Ansmann *et al.*, 2009]. The corresponding graphs are shown in Fig. 7.18. The curves of the two data sets differ strongly. When the Cape Verde data set is corrected for cloud-seeding effects, which can easily be identified in the tropics and thus be corrected for, the onset temperature of heterogeneous ice formation is  $-15$  °C. In the DRIFT data set ice-containing clouds were already detected at  $-5$  to  $-10$  °C. The resulting temperature shift between the SAMUM-2 and the DRIFT curve is thus 10 to 15 K. This shift is much larger

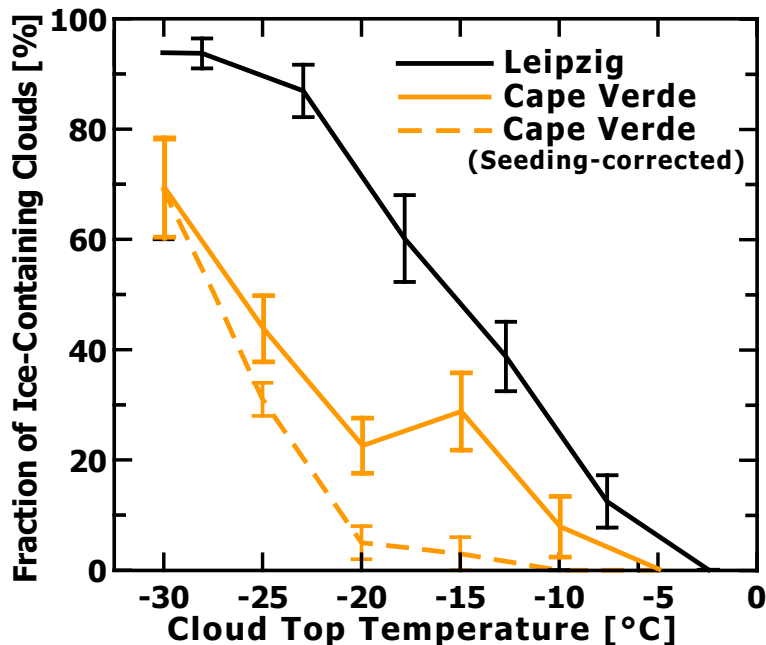


**Figure 7.18:** Comparison of the temperature dependence of the occurrence of ice-containing clouds over the tropical lidar site at Cape Verde (orange) [Ansmann *et al.*, 2009] and Leipzig (black). All clouds observed over Cape Verde and from the DRIFT data set are considered. Cloud seeding effects are corrected for the Cape Verde data set (dashed orange curve). Error bars indicate the standard error (see Eq. 7.1).

compared to the shift of only 5 K for temperatures from  $-5$  to  $-20$  °C for the resulting curves when the DRIFT data set was separated into dust-free and dust-laden clouds, respectively (see Fig. 7.17). Results similar to the curves of the Cape Verde data set were found during SAMUM-1 conducted close to the source of mineral dust in southern Morocco ( $30.9^\circ$  N,  $-6.9^\circ$  W) in 2006 [Ansmann *et al.*, 2008]. From 31 cloud layers observed with lidar only one contained ice at temperatures above  $-20$  °C. A more detailed analysis of the relationship between temperature and heterogeneous ice nucleation was not possible during this study because of the rather low number of observed cloud layers.

A simple explanation for the observed differences between the DRIFT and the SAMUM observations cannot be given. A multitude of effects may be active and probably even linked. If the relationship between temperature and the fraction of ice-containing clouds would only depend on the concentration of mineral dust particles, the curves of the dust-laden subset of the DRIFT data set and the SAMUM observations should equal. However, in comparison to the SAMUM observations even the dust-free subset of the DRIFT data shown in Figure 7.17 contains a larger fraction of ice-containing clouds at all temperatures.

The differences between the tropics and central Europe may be explained by the presence of other IN over the European continent that are active at higher temperatures than mineral dust particles. In laboratory studies biological particles as bacteria, pollen, and decayed organic material have been identified as favorable IN which may be active already in the temperature range from  $-2$  to  $-10$  °C [Szyrmer and Zawadzki, 1997; Diehl *et al.*, 2006; Möhler *et al.*, 2007]. There are many other aerosol constituents like lead and other metals or salts available over the polluted, industrialized continents that show favorable IN properties [Szyrmer and Zawadzki, 1997; Richardson *et al.*, 2007; Cziczo *et al.*, 2009b; Kamphus *et al.*, 2009; Pratt *et al.*, 2009; Stith *et al.*, 2009]. The overall IN concentration may be much lower in outflow plumes from the less industrialized African continent. In addition, air masses over central Europe are predominantly advected from the Atlantic Ocean (from southwesterly to northwesterly directions), and the free-tropospheric aerosols often contain a complex mixture of maritime and anthropogenic particles, mineral dust, and aged forest fire smoke from Canada or Siberia [Mattis *et al.*, 2008].

During the SAMUM-2 observations at Cape Verde in Winter 2008 typically only the lower troposphere up to 4–5 km height was heavily laden with a mixture of Saharan dust and biomass-burning aerosol [Tesche *et al.*, 2008, 2009a]. This is further illustrated in Figure 7.19 that shows the height-time cross section of the dust concentration calculated with DREAM for the SAMUM-2 observational period. The DREAM dust concentration above 4.5 km height at Cape Verde never exceeded the threshold value of  $2 \mu\text{g m}^{-3}$  (black line in Fig. 7.19) that was used to separate dust-free from dust-laden clouds in the DRIFT data set. A large fraction of the altocumulus clouds observed during SAMUM-2, indicated by white vertical bars, formed in dust-free air with dust concentrations of below  $0.001 \mu\text{g m}^{-3}$ . However, aerosol concentrations and thus IN concentrations exceeding tropospheric background values cannot be excluded, even at higher altitudes. Aerosols in the free troposphere above 5 km height may originate from remote, less polluted, tropical maritime

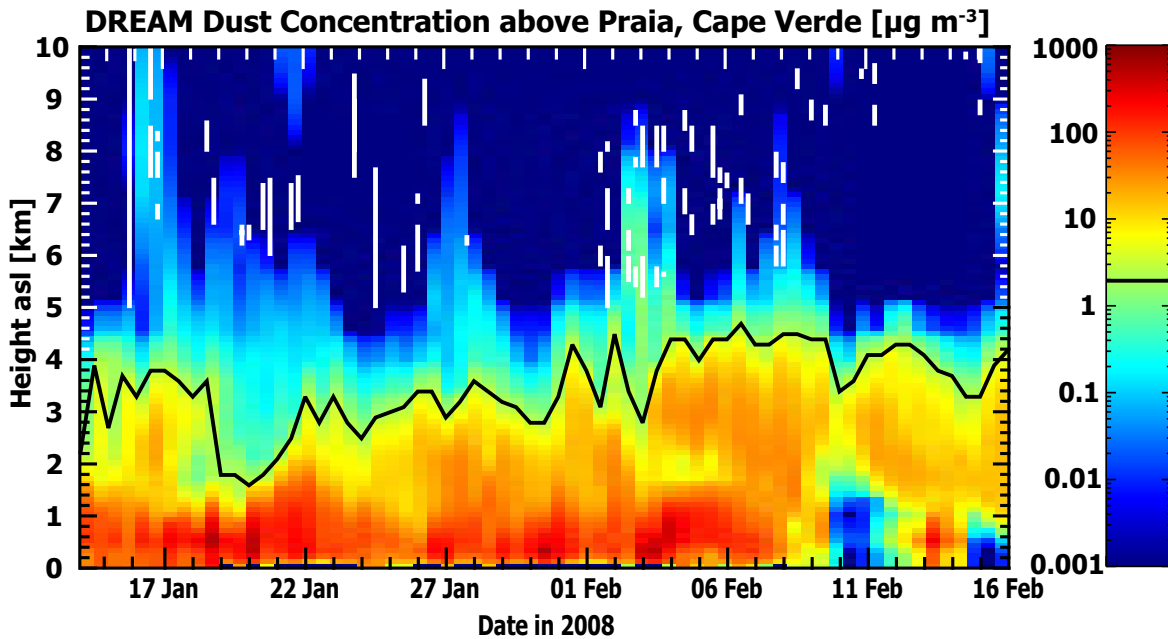


**Figure 7.19:** Altocumulus cloud layers (white vertical bars) observed during SAMUM-2 and corresponding temporal evolution of the DREAM dust concentration profile over Praia, Cape Verde. The length of the bars indicates the depth of the cloud layer (from bottom to top). The black curve indicates the maximum altitude with a dust concentration larger than  $2 \mu\text{g m}^{-3}$ . All altocumulus cloud layers from Figure 3 of *Ansmann et al.* [2009] are shown.

regions (Caribbean, northern South America, Pacific). However, they may contain traces of aged, cloud-processed smoke and dust which are injected into the free troposphere by deep convection at remote locations [*Dunjon and Velden, 2004; Ansmann et al., 2009; Wiacek and Peter, 2009*]. Additionally, as mentioned above, a comparable temperature relation of heterogeneous ice nucleation as observed over Cape Verde was also observed during the SAMUM-1 campaign in 2006 [*Ansmann et al., 2008*] where high aerosol particle concentrations of pure mineral dust were frequently present. Thus, if differences in the aerosol properties contribute to the found deviations between the observations in the tropics and at Leipzig mineral dust cannot be the responsible type of IN.

Also other processes may have contributed to the observed contrasts between central Europe and the tropics. Chemical processing, e.g., leading to a coating of dust with hygroscopic material, must be taken into account. Coating may reduce the ability of dust particles to serve as ice nuclei [*Wurzler et al., 2000; Möhler et al., 2008; Cziczo et al., 2009a*]. Furthermore, with increasing long-range transport time more and more large dust particles, which are the most favorable IN, are removed by sedimentation and washout [*Tegen and Fung, 1994; Tegen and Lacis, 1996*]. Chemical aging associated with coating during in-cloud processes and removal of dust particles by washout may have a stronger impact on the IN concentration in the tropics than in mid latitudes. Most of the long-range transports towards Europe occur during high-pressure situations during which cloud development is

widely suppressed [Ansmann *et al.*, 2003]. On the other hand, preactivation of dust particles [Knopf and Koop, 2006; Vali, 2008] may lead to an increasingly efficient ice nucleation with increasing transport time and an increasing number of cloud processes in which the IN were involved before. A simple conclusion on the role of cloud processing cannot be drawn at this point.

Ice enhancement mechanisms, such as the Hallett–Mossop mechanism [Hallett and Mossop, 1974] leading to enhanced ice formation at temperatures between  $-10$  and  $-5$  °C and other secondary ice production mechanisms [Cantrell and Heymsfield, 2005], may influence ice production over Europe and western Africa in a different way, too. As described in Section 2.3, the efficiency of most of these processes depends strongly on atmospheric turbulence and cloud dynamics. The majority of the observed clouds in the tropics, which were detected at heights from 5 to 10 km, were optically and spatially thinner than the ones in mid latitudes. This fact may indicate weaker radiative cooling effects and, as a consequence, weaker vertical motions in the free-tropospheric clouds in the tropics. Stronger vertical motions in mid latitudes associated with frontal passages probably improve conditions for drop formation, resulting in larger geometrical and optical depth of the formed clouds and stronger ice formation. For the Cape–Verde data set, Ansmann *et al.* [2009] reported geometrical depths of the observed liquid–water layers of below 300 m. From the DRIFT data set a geometrical depth of 360 m for the liquid–water clouds was obtained (see Table 7.4). Fronts, and in the case of the SAMUM–2 measurements also deep convection, were completely absent at Cape Verde. Stronger up– and downward motions in the middle and free troposphere in mid latitudes may cause large drops with diameters larger than  $25\ \mu\text{m}$  and broader drop size distributions, which seems to be a prerequisite for heterogeneous ice formation after Hobbs and Rangno [1985].

---



## Chapter 8

# Summary, conclusions, and outlook

### 8.1 Summary and conclusions

Within the scope of this work a unique lidar data set of tropospheric cloud observations at the central-European site of Leipzig covering a time period of 11 years (1997–2008) was analyzed with focus on the occurrence of ice crystals and liquid water droplets in optically thin, mostly stratiform cloud layers. The observed pure-liquid-water and ice-containing clouds, respectively, were categorized according to their layer-top temperatures and the aerosol properties in the air masses in which the clouds formed. Based on the compiled information the fraction of ice-containing clouds with respect to all clouds was studied in dependence of cloud top temperature in the range of heterogeneous ice nucleation between  $-40$  and  $0$  °C. Further, for the first time an attempt was presented that aims to quantify the influence of desert dust particles on heterogeneous ice formation based on long-term lidar observations. Therefore, the cloud data set was separated into dust-laden and dust-free fractions by means of a trajectory cluster analysis and by means of DREAM-derived profiles of the mineral dust concentration above Leipzig. The relationship between cloud top temperature and the fraction of ice-containing clouds was then studied separately for the dust-laden and dust-free data sets.

The following paragraphs summarize and conclude the results which were found from the analysis of the lidar data set. The steps which were carried out to find answers to the motivating questions listed in Chapter 3 are recapitulated.

Before the thermodynamic state of the observed clouds could be derived from the volume depolarization ratio measured with MARTHA, question 5 from Chapter 3 needed to be addressed (*Is it possible to unambiguously separate ice-containing from pure liquid-water clouds based on data of a zenith-pointing lidar as it was used for this study?*). Because MARTHA is a zenith-pointing lidar the measured depolarization ratio is affected by specular reflection produced by the horizontally aligned planar planes of falling ice crystals. Specular reflection leads to depolarization ratios of approximately zero which complicates the separation of the specular reflecting ice crystals from liquid-water droplets. Therefore, before the 11-year lidar data set of MARTHA was checked for the occurrence of clouds, a scheme had to be

---

found to separate ice-containing clouds and liquid-water clouds from data measured with a zenith-pointing lidar. Extensive and unique field studies with three lidars (MARTHA, Polly<sup>XT</sup>, WiLi) were performed to characterize specular reflection from horizontally aligned ice crystals in mixed-phase and cirrus clouds. Such a comprehensive study has never been done before, but is a prerequisite for a high-quality analysis of the data set. From the comparison of MARTHA measurements with data of the scanning Doppler lidar WiLi and the 5°-off-zenith-pointing lidar Polly<sup>XT</sup> it was found that specular reflection rarely affects entire cloud layers and that the cloud-base region is usually less affected by specular reflection because there the falling ice crystals sublimate which prevents the crystals to align horizontally. It was found that ice-containing cloud layers which are influenced by specular reflection can be identified by increased depolarization ratios at cloud base. Detailed studies of the distribution of liquid water droplets and ice crystals within one cloud layer was however found to be complicated when a zenith-pointing lidar is applied. Besides this important main finding, the comparative study revealed that specular reflection occurs most frequently at rather high temperatures from  $-10$  to  $-15$  °C. At temperatures below  $-50$  °C, specular reflection is almost absent. This behavior is most likely a consequence of changes in the shape and size of crystals with temperature.

In the next step, the 11-year lidar data set was screened for the occurrence of liquid-water and ice-containing clouds. From 2345 measurement hours 2319 cloud layers were identified. 1899 well-defined cloud layers passed the quality check of which 790 layers contained only liquid water droplets and 1109 layers were classified as ice-containing. Information about temperature and relative humidity at the cloud boundary heights were taken from radiosonde data obtained 40 km northwest of Leipzig or from archived model assimilation data for a grid point 25 km south of Leipzig. A comparison between coinciding radiosonde ascents and modeled profiles of temperature revealed deviations that are on the order of 1 K at heights above the boundary layer and below the tropopause.

The number of observed clouds accumulated around 0 °C for liquid-water clouds and around  $-60$  °C for ice-containing clouds. In the temperature range from  $-40$  to 0 °C 789 well-defined cloud layers were observed. This subset of clouds was denoted the DRIFT data set because all investigations concerning the relationship between cloud top temperature, heterogeneous freezing, and mineral dust concentration were based on these data.

Addressing question 1 from Chapter 3 (*Is there a clear dependence of the formation and presence of ice on cloud top temperature?*), now the fraction of ice-containing clouds with respect to all clouds in dependence of temperature was studied for the DRIFT data set. A strong increase of the fraction of ice-containing clouds was observed with decreasing temperature between  $-5$  and  $-25$  °C. Whereas only 8% of the observed clouds contained ice at temperatures between  $-5$  and  $-10$  °C, the fraction increased to 90% already at  $-20$  to  $-25$  °C. These findings were compared with *in situ* aircraft-based cloud climatologies of the ice-to-liquid-water ratio in dependence of temperature. The respective curve of the DRIFT data set was found to be similar to the other climatologies, showing the representativeness of the lidar-based cloud data set. The possible impact of the seeder-feeder mechanism and of

---

the restriction of the DRIFT data set to optically thin cloud layers was checked in addition. Both effects only marginally influence the relationship between cloud top temperature and the fraction of ice-containing clouds.

MARTHA observations of heterogeneous ice nucleation in dust-laden and in dust-free air masses were presented in detail in the context of five case studies. One observation of heterogeneous ice nucleation in a Saharan dust plume that was observed on 20 June 2007 documented the development of ice virgae in an altocumulus layer at cloud top temperatures of below  $-13\text{ }^{\circ}\text{C}$ . Contact nucleation was most likely the dominating process for the formation of the strong virgae. A completely different scenario was observed during a measurement on 3 November 2003 when supercooled liquid water was found down to temperatures of  $-32\text{ }^{\circ}\text{C}$  at aerosol background conditions.

Indications for the occurrence of deposition nucleation were discussed as well. In two case studies it was presented that temperatures of around  $-30\text{ }^{\circ}\text{C}$  appear to be needed for the nucleation of ice crystals via the deposition mode. In reference to question 2 from Chapter 3 (*Do the observations corroborate the hypothesis that freezing by deposition nucleation and condensation nucleation are of minor importance for the heterogeneous nucleation of ice?*) the general notion that deposition nucleation and condensation nucleation are of minor relevance at temperatures above  $-25\text{ }^{\circ}\text{C}$  was thus confirmed. At higher temperatures, the majority of the observed clouds showed, according to the measured low depolarization ratios, liquid-water layers at their tops. This finding implies that immersion or contact nucleation are the dominating pathways for ice formation in these cases.

Large efforts were undertaken to answer the question of the relevance of Saharan dust on heterogeneous freezing that was motivated in item 3 of Chapter 3 (*Is it possible to clearly identify the influence of Saharan dust on ice formation in ambient clouds on the basis of the long-term lidar data set of IfT?*). The separation of the DRIFT data set into dust-free and dust-laden fractions was realized through three different approaches — a HYSPLIT backward-trajectory cluster analysis and analyses that were based on DREAM data of column dust load and profiles of the dust concentration, respectively. Based on these data sets, a detailed investigation of the impact of dust on heterogeneous ice nucleation was performed by contrasting cloud observations in dust-free and dust-laden air masses. From the trajectory cluster analysis dust-free clouds whose air masses originated over the clean northern Atlantic Ocean were separated from dust-laden clouds whose trajectories passed the African continent and southwestern and southern Europe. From this separation it was found that the dust-laden clouds showed only a slightly enhanced amount of ice-containing clouds in the temperature range from  $-5$  to  $-20\text{ }^{\circ}\text{C}$ .

In the next approach the clouds were separated according to the corresponding DREAM column dust load. Thresholds of column dust load smaller than  $0.001\text{ g m}^{-2}$  and larger than  $0.02\text{ g m}^{-2}$  were used to define dust-free and dust-laden clouds, respectively. The subsequent comparison revealed also a slightly enhanced fraction of ice-containing clouds at temperatures from  $-5$  to  $-20\text{ }^{\circ}\text{C}$ .

In the third approach the DRIFT data set was separated according to the maximum

---

dust concentration that was calculated by DREAM within 500 m of the cloud boundaries. When the dust concentration was below the first output level of DREAM of  $0.001 \mu\text{g m}^{-3}$  the corresponding cloud layer was assigned to be dust-free. When more than  $2 \mu\text{g m}^{-3}$  of mineral dust were predicted within 500 m the corresponding cloud layer was defined to be dust-laden. Compared to dust-free air masses, a considerably higher amount of ice-containing clouds (about 30% more) was observed for cloud top temperatures from  $-5$  to  $-20$  °C in air masses that contained more than  $2 \mu\text{g m}^{-3}$  of Saharan dust within 500 m of the cloud boundaries. Ice formation by heterogeneous nucleation was thus found to start at approximately 5 K higher temperatures under dust-laden conditions compared to dust-free situations.

Of the three applied approaches to separate the cloud data set into dust-free and dust-laden subsamples the one based on vertically resolved information of the dust concentration revealed the most striking positive effect of mineral dust on ice nucleation at temperatures between  $-5$  and  $-20$  °C. Apparently, the rather passive indicators for the presence of dust in a cloud by means of the cluster analysis and the DREAM dust load do not allow for an accurate separation of dust-free and dust-laden clouds. This suggests that studies that relate column aerosol properties with height-dependent cloud parameters, as it was done in numerous satellite-based studies, may yield more accurate results when both compared parameters are available vertically resolved.

In the last step question 4 from Chapter 3 was addressed (*Is it possible to separate and quantify the aerosol-related and the meteorological (dynamical and thermodynamical) influence on heterogeneous ice nucleation in tropospheric stratiform clouds?*). To separate the possible contributions of aerosols and atmospheric dynamics on the temperature of heterogeneous nucleation, the central-European DRIFT data set was compared to similar observations in the tropics performed during the SAMUM-2 campaign at Cape Verde ( $15^\circ$  N) in 2008. The comparison revealed that ice formation is considerably enhanced and starts at higher temperatures at the mid-latitude site of Leipzig even in the absence of desert dust. In a literature review indications were discussed that aerosol-related as well as meteorological aspects may have contributed to the observed strong contrasts. It could not be clarified which of the two aspects is the dominant factor for the observed differences between the tropics and central Europe. Aerosol-related effects may arise from differences in the availability of efficient IN species like metals and biogenic material. These aerosol types may be more frequent over the anthropogenically polluted European continent. Also the age of the air masses in which the clouds formed may be different for the two sites. As a consequence, processes like IN preactivation or coating could influence the IN properties at both sites in a different way. Meteorological effects may arise from differences in the orography, leading to weaker wave activity over the maritime site of Cape Verde. According to earlier studies, differences in the strength of up- and downdrafts may yield smaller cloud drop sizes which would lead to less-efficient ice nucleation.

---

## 8.2 Outlook

The presented study successfully extended the range of mainly aerosol-oriented applications of the 11-year long-term lidar data set of MARTHA to the statistical evaluation of cloud properties. Synergies between different lidar instruments and between lidar data and model data were exploited in order to improve the accuracy of measured parameters but also in order to use lidar data in new fields of research as it is the case for the statistical studies of cloud-aerosol interactions.

A statistical evaluation of the dust-related ice formation based solely on lidar data was however not applied in the frame of this work. Before this approach can be performed, further investigations are needed to relate depolarization ratio, backscatter coefficient, and extinction coefficient to quantitative measures of the mineral dust concentration. Also the minimum detectable value of the mineral dust concentration must be determined in future studies. Even though the potential of lidar to provide a measure of the dust concentration was illustrated in the case studies presented in Chapter 6, to time the application of an approved model like DREAM can be regarded as a preferable data source when long-term, quantitative information about the presence of dust are needed as it was the case for this study.

Future lidar-based studies of cloud-aerosol interactions or of freezing processes in clouds will benefit considerably from complementary data of co-located instruments. The instrumental infrastructure of IfT Leipzig provides a solid basis for such attempts.

From co-located, simultaneous observations with MARTHA and the Doppler lidar WiLi of heterogeneous ice nucleation and dynamics (up- and downdrafts) in free-tropospheric clouds the relation between cloud dynamics and ice formation can be studied in more detail. During SAMUM-2 at Cape Verde, such measurements had been already performed with a polarization lidar and WiLi. Similar measurements must also be performed at Leipzig in order to make a comparative study possible. Besides such campaigns, it should nevertheless be aspired to continue running the regular measurements in order to increase the extent of the cloud data set. Automated polarization-lidar systems have the potential to provide almost unattended continuous measurements. Such measurements would increase the number of cloud observations considerably compared to the relatively small number of measurements that are performed with MARTHA.

The limitation of lidar to measure only optically thin clouds could be overcome by adding a cloud radar. Radar is almost not affected by precipitation and it would provide cloud-top information even when the lidar beam is already attenuated. From the spectral differences of the measured signals, Doppler velocities, and polarization properties at the different radar and lidar wavelengths information about the microphysics of the scattering cloud hydrometeors can be inferred in addition.

---



---

## Bibliography

- Albrecht, B. A. (1989), Aerosols, cloud microphysics, and fractional cloudiness, *Science*, *245*, 1227–1230.
- Althausen, D., R. Engelmann, H. Baars, B. Heese, A. Ansmann, D. Müller, and M. Kompula (2009), Portable Raman lidar Polly<sup>XT</sup> for automated profiling of aerosol backscatter, extinction, and depolarization, *Journal of Atmospheric and Oceanic Technology*, *26*, 2366–2378.
- Anderson, R. J., R. C. Miller, J. L. Kassner, Jr., and D. E. Hagen (1980), A study of homogeneous condensation–freezing nucleation of small water droplets in an expansion cloud chamber, *Journal of the Atmospheric Sciences*, *37*, 2508–2520.
- Ansmann, A. (2002), Molecular–backscatter lidar profiling of the volume–scattering coefficient in cirrus, in *Cirrus*, edited by D. K. Lynch, K. Sassen, D. O. Starr, and G. L. Stephens, pp. 197–210, Oxford University Press.
- Ansmann, A., and D. Müller (2005), Lidar and atmospheric aerosol particles, in *Lidar: Range-Resolved Optical Remote Sensing of the Atmosphere*, edited by C. Weitkamp, pp. 105–142, Springer.
- Ansmann, A., M. Riebesell, and C. Weitkamp (1990), Measurement of atmospheric aerosol extinction profiles with a Raman lidar, *Optics Letters*, *15*, 746–748.
- Ansmann, A., M. Riebesell, U. Wandinger, C. Weitkamp, E. Voss, W. Lahmann, and W. Michaelis (1992), Combined Raman elastic–backscatter lidar for vertical profiling of moisture, aerosol extinction, backscatter, and lidar ratio, *Applied Physics B*, *55*, 18–28.
- Ansmann, A., J. Bösenberg, A. Chaikovsky, A. Comerón, S. Eckhardt, R. Eixmann, V. Freudenthaler, P. Ginoux, L. Komguem, H. Linné, M. A. L. Márquez, V. Matthias, I. Mattis, V. Mitev, D. Müller, S. Music, S. Nickovic, J. Pelon, L. Sauvage, P. Sobolewsky, M. K. Srivastava, A. Stohl, O. Torres, G. Vaughan, U. Wandinger, and M. Wiegner (2003), Long–range transport of Saharan dust to northern Europe: The 11–16 October 2001 outbreak observed with EARLINET, *Journal of Geophysical Research*, *108*(D24), 4783, doi: 10.1029/2003JD003757.
-

- Ansmann, A., I. Mattis, D. Müller, U. Wandinger, M. Radlach, D. Althausen, and R. Damoah (2005), Ice formation in Saharan dust over central Europe observed with temperature/humidity/aerosol Raman lidar, *Journal of Geophysical Research*, *110*, D18S12, doi:10.1029/2004JD005000.
- Ansmann, A., M. Tesche, D. Althausen, D. Müller, P. Seifert, V. Freudenthaler, B. Heese, M. Wiegner, G. Pisani, P. Knippertz, and O. Dubovik (2008), Influence of Saharan dust on cloud glaciation in southern Morocco during the Saharan Mineral Dust Experiment, *Journal of Geophysical Research*, *113*, D04210, doi:10.1029/2007JD008785.
- Ansmann, A., M. Tesche, P. Seifert, D. Althausen, R. Engelmann, J. Fruntke, U. Wandinger, I. Mattis, and D. Müller (2009), Evolution of the ice phase in tropical altocumulus: SAMUM lidar observations over Cape Verde, *Journal of Geophysical Research*, *114*, D17208, doi:10.1029/2008JD011659.
- Beard, K. V. (1992), Ice initiation in warm-base convective clouds: An assessment of microphysical mechanisms, *Atmospheric Research*, *28*, 125–152.
- Bissonnette, L. R. (2005), Lidar and multiple scattering, in *Lidar: Range-Resolved Optical Remote Sensing of the Atmosphere*, edited by C. Weitkamp, pp. 43–103, Springer.
- Bohren, C. F., and D. R. Huffman (1983), *Absorption and Scattering of Light by Small Particles*, 530 pp., John Wiley.
- Borovikov, A. M., I. I. Gaivoronskii, E. G. Zak, V. V. Kostarev, I. P. Manzi, V. E. Minervin, A. K. Khrgian, and S. M. Shmeter (1963), Cloud physics, *Translation from Russian. Izrael Program for Scientific Translations*, p. 392.
- Borys, R. D., and M. A. Wetzel (1997), Storm peak laboratory: A research, teaching, and service facility for the atmospheric sciences, *Bulletin of the American Meteorological Society*, *78*, 2115–2123.
- Bucholtz, A. (1995), Rayleigh-scattering calculations for the terrestrial atmosphere, *Applied Optics*, *34*, 2765–2773.
- Burrows, S. M., W. Elbert, M. G. Lawrence, and U. Pöschl (2009), Bacteria in the global atmosphere—Part 1: Review and synthesis of literature data for different ecosystems, *Atmospheric Chemistry and Physics*, *9*, 9263–9280.
- Cairo, F., G. di Donfrancesco, A. Adriani, L. Pulvirenti, and F. Fierli (1999), Comparison of various linear depolarization parameters measured by lidar, *Applied Optics*, *38*, 4425–4432.
- Cantrell, W., and A. Heymsfield (2005), Production of ice in tropospheric clouds: A review, *Bulletin of the American Meteorological Society*, *86*, 795–807.
-

- Cape, J. N., J. Methven, and L. E. Hudson (2000), The use of trajectory cluster analysis to interpret trace gas measurements at Mace Head, Ireland, *Atmospheric Environment*, *34*, 3651–3663.
- Chen, Y., S. M. Kreidenweis, L. M. McInnes, D. C. Rogers, and P. J. DeMott (1998), Single particle analyses of ice nucleating aerosols in the upper troposphere and lower stratosphere, *Geophysical Research Letters*, *25*, 1391–1394, doi:10.1029/97GL03261.
- Collis, R. T. H., and P. B. Russell (1976), Lidar measurement of particles and gases by elastic backscattering and differential absorption, in *Laser Monitoring of the Atmosphere*, edited by E. D. Hinkley, pp. 71–151, Springer.
- Connolly, P. J., O. Möhler, P. R. Field, H. Saathoff, R. Burgess, T. Choularton, and M. Gallagher (2009), Studies of heterogeneous freezing by three different desert dust samples, *Atmospheric Chemistry and Physics*, *9*, 2805–2824.
- Cotton, R. J., and P. R. Field (2002), Ice nucleation characteristics of an isolated wave cloud, *Quarterly Journal of the Royal Meteorological Society*, *128*, 2417–2437.
- Cozic, J., S. Mertes, B. Verheggen, D. J. Cziczo, S. J. Gallavardin, S. Walter, U. Baltensperger, and E. Weingartner (2008), Black carbon enrichment in atmospheric ice particle residuals observed in lower tropospheric mixed phase clouds, *Journal of Geophysical Research*, *113*, D15209, doi:10.1029/2007JD009266.
- Cziczo, D. J., P. J. DeMott, S. D. Brooks, A. J. Prenni, D. S. Thomson, D. Baumgardner, J. C. Wilson, S. M. Kreidenweis, and D. M. Murphy (2004a), Observations of organic species and atmospheric ice formation, *Geophysical Research Letters*, *31*, L12116, doi:10.1029/2004GL019822.
- Cziczo, D. J., D. M. Murphy, P. K. Hudson, and D. S. Thomson (2004b), Single particle measurements of the chemical composition of cirrus ice residue during CRYSTAL-FACE, *Journal of Geophysical Research*, *109*(D18), D04201, doi:10.1029/2003JD004032.
- Cziczo, D. J., K. Froyd, S. Gallavardin, O. Moehler, S. Benz, H. Saathoff, and D. Murphy (2009a), Deactivation of ice nuclei due to atmospherically relevant surface coatings, *Environmental Research Letters*, *4*, 044013.
- Cziczo, D. J., O. Stetzer, A. Worringer, M. Ebert, S. Weinbruch, M. Kamphus, S. J. Gallavardin, J. Curtius, S. Borrmann, K. D. Froyd, S. Mertes, O. Möhler, and U. Lohmann (2009b), Inadvertent climate modification due to anthropogenic lead, *Nature Geoscience*, *2*, 333–336.
- Deirmendian, D. (1969), *Electromagnetic Scattering on Spherical Particles*, 290 pp., Elsevier.
- DeMott, P. J. (2002), Laboratory studies of cirrus cloud processes, in *Cirrus*, edited by D. K. Lynch, K. Sassen, D. O. Starr, and G. L. Stephens, pp. 102–135, Oxford University Press.
-

- DeMott, P. J., D. J. Cziczo, A. J. Prenni, D. M. Murphy, S. M. Kreidenweis, D. S. Thomson, R. Borys, and D. C. Rogers (2003a), Measurements of the concentration and composition of nuclei for cirrus formation, *Proceedings of the National Academy of Science*, *100*, 14655–14660.
- DeMott, P. J., K. Sassen, M. R. Poellot, D. Baumgardner, D. C. Rogers, S. D. Brooks, A. J. Prenni, and S. M. Kreidenweis (2003b), African dust aerosols as atmospheric ice nuclei, *Geophysical Research Letters*, *30*, 1732, doi:10.1029/2003GL017410.
- DeMott, P. J., K. Sassen, M. R. Poellot, D. Baumgardner, D. C. Rogers, S. D. Brooks, A. J. Prenni, and S. M. Kreidenweis (2009), Correction to “African dust aerosols as atmospheric ice nuclei”, *Geophysical Research Letters*, *36*, L07808, doi:10.1029/2009GL037639.
- Diehl, K., and S. K. Mitra (1998), A laboratory study of the effects of a kerosene–burner exhaust on ice nucleation and the evaporation rate of ice crystals, *Atmospheric Environment*, *32*, 3145–3151.
- Diehl, K., M. Simmel, and S. Wurzler (2006), Numerical sensitivity studies on the impact of aerosol properties and drop freezing modes on the glaciation, microphysics, and dynamics of clouds, *Journal of Geophysical Research*, *111*, D07202, doi:10.1029/2005JD005884.
- Dorling, S. R., T. D. Davies, and C. E. Pierce (1992), Cluster analysis: A technique for estimating the synoptic meteorological controls on air and precipitation chemistry — Method and applications, *Atmospheric Environment*, *26*, 2575–2581.
- Draxler, R. R., and G. D. Hess (1998), An overview of the HYSPLIT4 modelling system for trajectories, dispersion, and deposition, *Australian Meteorological Magazine*, *47*, 295–308.
- Draxler, R. R., and G. D. Rolph (2003), HYSPLIT (HYbrid Single-Particle Lagrangian Integrated Trajectory). Model access via NOAA ARL READY website (<http://www.arl.noaa.gov/ready/hysplit4.html>), *NOAA Air Resources Laboratory, Silver Spring, MD*.
- Draxler, R. R., B. Stunder, G. D. Rolph, A. Stein, and A. Taylor (2009), HYSPLIT4 user’s guide. Access via NOAA ARL READY Website (<http://www.arl.noaa.gov/ready/hysplit4.html>), *NOAA Air Resources Laboratory, Silver Spring, MD*.
- Duce, R. (1995), Distributions and fluxes of mineral aerosol, in *Aerosol Forcing of Climate*, edited by R. J. Charlson and J. Heintzenberg, pp. 43–72, John Wiley.
- Dunion, J. P., and C. S. Velden (2004), The impact of the Saharan air layer on Atlantic tropical cyclone activity, *Bulletin of the American Meteorological Society*, *85*, 353–365.
- Durant, A. J., and R. A. Shaw (2005), Evaporation freezing by contact nucleation inside-out, *Geophysical Research Letters*, *32*, L20814, doi:10.1029/2005GL024175.
-

- Ehrlich, A., M. Wendisch, E. Bierwirth, J. F. Gayet, G. Mioche, A. Lampert, and B. Mayer (2009), Evidence of ice crystals at cloud top of arctic boundary–layer mixed–phase clouds derived from airborne remote sensing, *Atmospheric Chemistry and Physics*, *9*, 9401–9416.
- Engelmann, R. (2009), Aerosol vertical exchange in the convective planetary boundary layer — turbulent particle flux measurements with combined wind and aerosol lidar, Ph.D. thesis, University of Leipzig. 153 pp.
- Engelmann, R., U. Wandinger, A. Ansmann, D. Müller, E. Žeromskis, D. Althausen, and B. Wehner (2008), Lidar observations of the vertical aerosol flux in the planetary boundary layer, *Journal of Atmospheric and Oceanic Technology*, *25*, 1296–1306.
- Esselborn, M., M. Wirth, A. Fix, B. Weinzierl, K. Rasp, M. Tesche, and A. Petzold (2009), Spatial distribution and optical properties of Saharan dust observed by airborne high spectral resolution lidar during SAMUM 2006, *Tellus Series B*, *61*, 131–143.
- Feingold, G., W. L. Eberhard, D. E. Veron, and M. Previdi (2003), First measurements of the Twomey indirect effect using ground-based remote sensors, *Geophysical Research Letters*, *30*, 1287, doi:10.1029/2002GL016633.
- Fernald, F. G. (1984), Analysis of atmospheric lidar observations: some comments, *Applied Optics*, *23*, 652–653.
- Field, P. R., O. Möhler, P. Connolly, M. Krämer, R. Cotton, A. J. Heymsfield, H. Saathoff, and M. Schnaiter (2006), Some ice nucleation characteristics of Asian and Saharan desert dust, *Atmospheric Chemistry and Physics*, *6*, 2991–3006.
- Findeisen, W. (1938), Die kolloidmeteorologischen Vorgänge bei der Niederschlagsbildung, *Meteorologische Zeitschrift*, *55*, 121–133.
- Flanner, M. G., C. S. Zender, J. T. Randerson, and P. J. Rasch (2007), Present–day climate forcing and response from black carbon in snow, *Journal of Geophysical Research*, *112*, D11202, doi:10.1029/2006JD008003.
- Fleishauer, R. P., V. E. Larson, and T. H. Vonder Haar (2002), Observed microphysical structure of midlevel, mixed–phase clouds, *Journal of the Atmospheric Sciences*, *59*, 1779–1804.
- Fletcher, N. H. (1962), *Physics of Rain Clouds*, 386 pp., Cambridge University Press.
- Freudenthaler, V., M. Esselborn, M. Wiegner, B. Heese, M. Tesche, A. Ansmann, D. Müller, D. Althausen, M. Wirth, A. Fix, G. Ehret, P. Knippertz, C. Toledano, J. Gasteiger, M. Garhammer, and M. Seefeldner (2009), Depolarization ratio profiling at several wavelengths in pure Saharan dust during SAMUM 2006, *Tellus Series B*, *61*, 165–179.
-

- Fridlind, A. M., A. S. Ackerman, G. McFarquhar, G. Zhang, M. R. Poellot, P. J. DeMott, A. J. Prenni, and A. J. Heymsfield (2007), Ice properties of single-layer stratocumulus during the Mixed-Phase Arctic Cloud Experiment: 2. Model results, *Journal of Geophysical Research*, *112*, D24202, doi:10.1029/2007JD008646.
- Gayet, J.-F., R. Treffeisen, A. Helbig, J. Bareiss, A. Matsuki, A. Herber, and A. Schwarzenboeck (2009), On the onset of the ice phase in boundary layer Arctic clouds, *Journal of Geophysical Research*, *114*, D19201, doi:10.1029/2008JD011348.
- Georgii, H.-W. (1959), Neue Untersuchungen über den Zusammenhang zwischen atmosphärischen Gefrierkernen und Kondensationskernen, *Geofisica Pura e Applicata*, *42*, 62–72.
- Gorbunov, B., A. Baklanov, N. Kakutkina, H. L. Windsor, and R. Toumi (2001), Ice nucleation on soot particles, *Journal of Aerosol Science*, *32*, 199–215.
- Grein, M. (2006), Charakterisierung und Erweiterung der Empfängeroptik des IFT-Ramanlidars MARTHA für kombinierte Aerosol- und Wolkenmessungen, Diploma thesis, University of Leipzig. 78 pp.
- Hallett, J., and S. C. Mossop (1974), Production of secondary ice particles during the riming process, *Nature*, *249*, 26–28.
- Hallett, J., W. P. Arnott, M. P. Bailey, and J. T. Hallett (2002), Ice crystals in cirrus, in *Cirrus*, edited by D. K. Lynch, K. Sassen, D. O. Starr, and G. L. Stephens, pp. 41–77, Oxford University Press.
- Harrington, J. Y., T. Reisin, W. R. Cotton, and S. M. Kreidenweis (1999), Cloud resolving simulations of Arctic stratus—Part II: Transition-season clouds, *Atmospheric Research*, *51*, 45–75.
- Haustein, K., C. Pérez, J. M. Baldasano, D. Müller, M. Tesche, A. Schladitz, M. Esselborn, B. Weinzierl, K. Kandler, and W. von Hoyningen-Huene (2009), Regional dust model performance during SAMUM 2006, *Geophysical Research Letters*, *36*, L03812, doi:10.1029/2008GL036463.
- Heintzenberg, J. (2009), The SAMUM-1 experiment over Southern Morocco: overview and introduction, *Tellus Series B*, *61*, 2–11.
- Heintzenberg, J., and B. J. Charlson (Eds.) (2009), *Clouds in the perturbed climate system: Their relationship to energy balance, atmospheric dynamics, and precipitation*, 597 pp., MIT Press.
- Herich, H., T. Tritscher, A. Wiacek, M. Gysel, E. Weingartner, U. Lohmann, U. Baltensperger, and D. J. Cziczo (2009), Water uptake of clay and desert dust aerosol particles at sub- and supersaturated water vapor conditions, *Physical Chemistry Chemical Physics*, *11*, 7804–7809.
-

- Heymsfield, A. J., and R. M. Sabin (1989), Cirrus crystal nucleation by homogeneous freezing of solution droplets, *Journal of the Atmospheric Sciences*, *46*, 2252–2264.
- Hobbs, P. V. (1969), Ice multiplication in clouds, *Journal of the Atmospheric Sciences*, *26*, 315–318.
- Hobbs, P. V., and A. L. Rangno (1985), Ice particle concentrations in clouds, *Journal of the Atmospheric Sciences*, *42*, 2523–2549.
- Hoffer, T. E. (1961), A laboratory investigation of droplet freezing, *Journal of the Atmospheric Sciences*, *18*, 766–778.
- Hogan, R. J., P. N. Francis, H. Flentje, A. J. Illingworth, M. Quante, and J. Pelon (2003), Characteristics of mixed-phase clouds. I: Lidar, radar and aircraft observations from CLARE'98, *Quarterly Journal of the Royal Meteorological Society*, *129*, 2089–2116.
- Holben, B. N., D. Tanré, A. Smirnov, T. F. Eck, I. Slutsker, N. Abuhassan, W. W. Newcomb, J. S. Schafer, B. Chatenet, F. Lavenu, Y. J. Kaufman, J. V. Castle, A. Setzer, B. Markham, D. Clark, R. Frouin, R. Halthore, A. Karneli, N. T. O'Neill, C. Pietras, R. T. Pinker, K. Voss, and G. Zibordi (2001), An emerging ground-based aerosol climatology: Aerosol optical depth from AERONET, *Journal of Geophysical Research*, *106*, 12067–12098, doi: 10.1029/2001JD900014.
- Howell, W. E. (1977), Environmental impacts of precipitation management: Results and inferences from project Skywater, *Bulletin of the American Meteorological Society*, *58*, 488–587.
- Huffman, P. J. (1973), Supersaturation spectra of AgI and natural ice nuclei, *Journal of Applied Meteorology*, *12*, 1080–1081.
- Iaquinta, J., H. Isaka, and P. Personne (1995), Scattering phase function of bullet rosette ice crystals, *Journal of the Atmospheric Sciences*, *52*, 1401–1413.
- Illingworth, A. J., R. J. Hogan, E. J. O'Connor, D. Bouniol, M. E. Brooks, J. Delanoë, D. P. Donovan, J. D. Eastment, N. Gaussiat, J. W. F. Goddard, M. Haeffelin, H. K. Baltink, O. A. Krasnov, J. Pelon, J.-M. Piriou, A. Protat, H. W. J. Russchenberg, A. Seifert, A. M. Tompkins, G.-J. van Zadelhoff, F. Vinit, U. Willén, D. R. Wilson, and C. L. Wrench (2007), Cloudnet — continuous evaluation of cloud profiles in seven operational models using ground-based observations, *Bulletin of the American Meteorological Society*, *88*, 883–898.
- IPCC (2001), *Climate Change 2001: The Scientific Basis. Contribution of Working Group I to the Third Assessment Report of the Intergovernmental Panel on Climate Change*, 881 pp., Cambridge University Press.
-

- IPCC (2007), *Climate Change 2007: The Scientific Basis. Contribution of Working Group I to the Fourth Assessment Report of the Intergovernmental Panel on Climate Change*, 996 pp., Cambridge University Press.
- Isaac, G. A., and R. S. Schemenauer (1979), Large particles in supercooled regions of northern Canadian cumulus clouds, *Journal of Applied Meteorology*, *18*, 1056–1065.
- Jenson, E., D. Starr, and O. B. Toon (2004), Mission investigates tropical cirrus clouds, *EOS Transactions*, *85*, 45–50.
- Jickells, T. D., Z. S. An, K. K. Andersen, A. R. Baker, G. Bergametti, N. Brooks, J. J. Cao, P. W. Boyd, R. A. Duce, K. A. Hunter, H. Kawahata, N. Kubilay, J. LaRoche, P. S. Liss, N. Mahowald, J. M. Prospero, A. J. Ridgwell, I. Tegen, and R. Torres (2005), Global iron connections between desert dust, ocean biogeochemistry, and climate, *Science*, *308*, 67–71.
- Kamphus, M., M. Ettner-Mahl, F. Drewnick, L. Keller, D. J. Cziczo, S. Mertes, S. Borrmann, and J. Curtius (2009), Chemical composition of ambient aerosol, ice residues and cloud droplet residues in mixed-phase clouds: single particle analysis during the Cloud and Aerosol Characterization Experiment (CLACE 6), *Atmospheric Chemistry and Physics Discussions*, *9*, 15375–15421.
- Kanamitsu, M. (1989), Description of the NMC global data assimilation and forecast system, *Weather and Forecasting*, *4*, 335–342.
- Kanji, Z. A., and J. P. D. Abbatt (2006), Laboratory studies of ice formation via deposition mode nucleation onto mineral dust and n-hexane soot samples, *Journal of Geophysical Research*, *111*, D16204, doi:10.1029/2005JD006766.
- Kaufman, Y. J., I. Koren, L. A. Remer, D. Rosenfeld, and Y. Rudich (2005), The effect of smoke, dust, and pollution aerosol on shallow cloud development over the Atlantic Ocean, *Proceedings of the National Academy of Science*, *102*, 11207–11212.
- Kerkweg, A., S. Wurzler, T. Reisin, and A. Bott (2003), On the cloud processing of aerosol particles: An entraining air-parcel model with two-dimensional spectral cloud microphysics and a new formulation of the collection kernel, *Quarterly Journal of the Royal Meteorological Society*, *129*, 1–18.
- Klett, J. D. (1981), Stable analytical solution for processing lidar returns, *Applied Optics*, *20*, 211–220.
- Knopf, D. A., and T. Koop (2006), Heterogeneous nucleation of ice on surrogates of mineral dust, *Journal of Geophysical Research*, *111*, D12201, doi:10.1029/2005JD006894.
- Koop, T., B. Luo, A. Tsias, and T. Peter (2000), Water activity as the determinant for homogeneous ice nucleation in aqueous solutions, *Nature*, *406*, 611–614.
-

- Koren, I., Y. J. Kaufman, L. A. Remer, and J. V. Martins (2004), Measurement of the effect of Amazon smoke on inhibition of cloud formation, *Science*, *303*, 1342–1345.
- Korolev, A. V. (2007), Limitations of the Wegener Bergeron Findeisen mechanism in the evolution of mixed-phase clouds, *Journal of the Atmospheric Sciences*, *64*, 3372.
- Korolev, A. V., and P. R. Field (2008), The effect of dynamics on mixed-phase clouds: Theoretical considerations, *Journal of the Atmospheric Sciences*, *65*, 66–86.
- Korolev, A. V., G. A. Isaac, S. G. Cober, J. W. Strapp, and J. Hallett (2003), Microphysical characterization of mixed-phase clouds, *Quarterly Journal of the Royal Meteorological Society*, *129*, 39–65.
- Kulkarni, G., and S. Dobbie (2010), Ice nucleation properties of mineral dust particles: determination of onset  $RH_i$ , IN active fraction, nucleation time-lag, and the effect of active sites on contact angles, *Atmospheric Chemistry and Physics*, *10*, 95–105.
- Lebo, Z. J., N. C. Johnson, and J. Y. Harrington (2008), Radiative influences on ice crystal and droplet growth within mixed-phase stratus clouds, *Journal of Geophysical Research*, *113*, D09203, doi:10.1029/2007JD009262.
- Levin, Z., and J. L. Brenguier (2008), Effects of pollution and biomass burning aerosols on clouds and precipitation: Observational studies, in *Aerosol Pollution Impact on Precipitation — A Scientific Review*, edited by Z. Levin and W. R. Cotton, chap. 6, pp. 205–241, Springer.
- Levin, Z., and S. A. Yankofsky (1983), Contact versus immersion freezing of freely suspended droplets by bacterial ice nuclei, *Journal of Applied Meteorology*, *22*, 1964–1966.
- Levin, Z., A. Teller, E. Ganor, and Y. Yin (2005), On the interactions of mineral dust, sea-salt particles, and clouds: A measurement and modeling study from the Mediterranean Israeli Dust Experiment campaign, *Journal of Geophysical Research*, *110*, D20202, doi:10.1029/2005JD005810.
- Liljequist, G. H., and K. Cihak (2006), *Allgemeine Meteorologie*, Springer.
- Liou, K. N., and H. Lahore (1974), Laser sensing of cloud composition: A backscattered depolarization technique, *Journal of Applied Meteorology*, *13*, 257–263.
- Liou, K. N., and R. M. Schotland (1971), Multiple backscattering and depolarization from water clouds for a pulsed lidar system, *Journal of the Atmospheric Sciences*, *28*, 772–784.
- Liu, Z., A. Omar, M. Vaughan, J. Hair, C. Kittaka, Y. Hu, K. Powell, C. Trepte, D. Winker, C. Hostetler, R. Ferrare, and R. Pierce (2008), CALIPSO lidar observations of the optical properties of Saharan dust: A case study of long-range transport, *Journal of Geophysical Research*, *113*, D07207, doi:10.1029/2007JD008878.
-

- Liu, Z., M. Vaughan, D. Winker, C. Kittaka, B. Getzewich, R. Kuehn, A. Omar, K. Powell, C. Trepte, and C. Hostetler (2009), The CALIPSO lidar cloud and aerosol discrimination: Version 2 algorithm and initial assessment of performance, *Journal of Atmospheric and Oceanic Technology*, *26*, 1198.
- Lohmann, U., and J. Feichter (2005), Global indirect aerosol effects: a review, *Atmospheric Chemistry and Physics*, *5*, 715–737.
- Lohmann, U., and C. Hoose (2009), Sensitivity studies of different aerosol indirect effects in mixed-phase clouds, *Atmospheric Chemistry and Physics*, *9*, 8917–8934.
- Magono, C., and C. W. Lee (1966), Meteorological classification of natural snow crystals, *Journal of the Faculty of Science of Hokkaido University, Series 7, 2*, 320–335.
- Mason, B. J. (1950), The nature of ice-forming nuclei in the atmosphere, *Quarterly Journal of the Royal Meteorological Society*, *76*, 59–74.
- Mason, B. J. (1971), *The Physics of Clouds*, 544 pp., Oxford University Press.
- Mattis, I. (2002), Aufbau eines Feuchte–Temperatur–Aerosol–Ramanlidars und Methodenentwicklung zur kombinierten Analyse von Trajektorien und Aerosolprofilen, Ph.D. thesis, University of Leipzig. 130 pp.
- Mattis, I., A. Ansmann, D. Müller, U. Wandinger, and D. Althausen (2002), Dual-wavelength Raman lidar observations of the extinction-to-backscatter ratio of Saharan dust, *Geophysical Research Letters*, *29*, 1306, doi:10.1029/2002GL014721.
- Mattis, I., A. Ansmann, D. Müller, U. Wandinger, and D. Althausen (2004), Multiyear aerosol observations with dual-wavelength Raman lidar in the framework of EARLINET, *Journal of Geophysical Research*, *109*, 13203, doi:10.1029/2004JD004600.
- Mattis, I., D. Müller, A. Ansmann, U. Wandinger, J. Preißler, P. Seifert, and M. Tesche (2008), Ten years of multiwavelength Raman lidar observations of free-tropospheric aerosol layers over central Europe: Geometrical properties and annual cycle, *Journal of Geophysical Research*, *113*, D20202, doi:10.1029/2007JD009636.
- McFarquhar, G. M., and A. J. Heymsfield (1996), Microphysical characteristics of three anvils sampled during the Central Equatorial Pacific Experiment, *Journal of the Atmospheric Sciences*, *53*, 2401–2423.
- McFarquhar, G. M., and A. J. Heymsfield (1997), Parameterization of tropical cirrus ice crystal size distributions and implications for radiative transfer: Results from CEPEX, *Journal of the Atmospheric Sciences*, *54*, 2187–2200.
- Meyers, M. P., P. J. DeMott, and W. R. Cotton (1992), New primary ice-nucleation parameterizations in an explicit cloud model, *Journal of Applied Meteorology*, *31*, 708–721.
-

- Möhler, O., A. Nink, H. Saathoff, S. Schaefers, M. Schnaiter, W. Schöck, and U. Schurath (2001), The Karlsruhe aerosol chamber facility AIDA: Technical description and first results of homogeneous and heterogeneous ice nucleation experiments, in *Proceedings of Workshop on Ion–Aerosol–Cloud–Interactions (IACI), CERN 2001–007, Geneva*, edited by J. Kirkby.
- Möhler, O., P. J. DeMott, G. Vali, and Z. Levin (2007), Microbiology and atmospheric processes: The role of biological particles in cloud physics, *Biogeosciences*, *4*, 1059–1071.
- Möhler, O., S. Benz, H. Saathoff, M. Schnaiter, R. Wagner, J. Schneider, S. Walter, V. Ebert, and S. Wagner (2008), The effect of organic coating on the heterogeneous ice nucleation efficiency of mineral dust aerosols, *Environmental Research Letters*, *3*, 025007.
- Morrison, H., M. D. Shupe, J. O. Pinto, and J. A. Curry (2005), Possible roles of ice nucleation mode and ice nuclei depletion in the extended lifetime of Arctic mixed–phase clouds, *Geophysical Research Letters*, *32*, L18801, doi:10.1029/2005GL023614.
- Muhlbauer, A., and U. Lohmann (2009), Sensitivity studies of aerosol–cloud interactions in mixed–phase orographic precipitation, *Journal of the Atmospheric Sciences*, *66*, 2517–2538.
- Müller, D., I. Mattis, U. Wandinger, A. Ansmann, D. Althausen, O. Dubovik, S. Eckhardt, and A. Stohl (2003), Saharan dust over a central European EARLINET–AERONET site: Combined observations with Raman lidar and Sun photometer, *Journal of Geophysical Research*, *108*, 4345, doi:10.1029/2002JD002918.
- Müller, D., I. Mattis, A. Ansmann, B. Wehner, D. Althausen, U. Wandinger, and O. Dubovik (2004), Closure study on optical and microphysical properties of a mixed urban and Arctic haze air mass observed with Raman lidar and Sun photometer, *Journal of Geophysical Research*, *109*, D13206, doi:10.1029/2003JD004200.
- Müller, D., I. Mattis, U. Wandinger, A. Ansmann, D. Althausen, and A. Stohl (2005), Raman lidar observations of aged Siberian and Canadian forest fire smoke in the free troposphere over Germany in 2003: Microphysical particle characterization, *Journal of Geophysical Research*, *110*, D17201, doi:10.1029/2004JD005756.
- Müller, D., A. Ansmann, I. Mattis, M. Tesche, U. Wandinger, D. Althausen, and G. Pisani (2007), Aerosol–type–dependent lidar ratios observed with Raman lidar, *Journal of Geophysical Research*, *112*, D16202, doi:10.1029/2006JD008292.
- Nickovic, S., G. Kallos, A. Papadopoulos, and O. Kakaliagou (2001), A model for prediction of desert dust cycle in the atmosphere, *Journal of Geophysical Research*, *106*, 18113–18130, doi:10.1029/2000JD900794.
- Niedermeier, D., S. Hartmann, R. A. Shaw, D. Covert, T. F. Mentel, J. Schneider, L. Poulain, P. Reitz, C. Spindler, T. Clauss, A. Kiselev, E. Hallbauer, H. Wex, K. Mildenerger,
-

- and F. Stratmann (2010), Heterogeneous freezing of droplets with immersed mineral dust particles—measurements and parameterization, *Atmospheric Chemistry and Physics*, 8, 3601–3614.
- O’Connor, E. J., A. J. Illingworth, and R. J. Hogan (2004), A technique for autocalibration of cloud lidar, *Journal of Atmospheric and Oceanic Technology*, 21, 777.
- Ou, S., K. Liou, X. Wang, R. Hansell, R. Lefevre, and S. Cocks (2009), Satellite remote sensing of dust aerosol indirect effects on ice cloud formation, *Applied Optics*, 48, 633–642.
- Penner, R. (1995), Carbonaceous aerosols influencing atmospheric radiation: Black and organic carbon, in *Aerosol Forcing of Climate*, edited by R. J. Charlson and J. Heintzenberg, pp. 91–108, John Wiley.
- Peppler, W. (1940), Unterkühlte Wasserwolken und Eiswolken, *Forschungs- und Erfahrungsberichte des Reichsamts für Wetterdienst, Band 1*, 3–68.
- Pérez, C., S. Nickovic, J. M. Baldasano, M. Sicard, F. Rocadenbosch, and V. E. Cachorro (2006a), A long Saharan dust event over the western Mediterranean: Lidar, Sun photometer observations, and regional dust modeling, *Journal of Geophysical Research*, 111, D15214, doi:10.1029/2005JD006579.
- Pérez, C., S. Nickovic, G. Pejanovic, J. M. Baldasano, and E. Özsoy (2006b), Interactive dust-radiation modeling: A step to improve weather forecasts, *Journal of Geophysical Research*, 111, D16206, doi:10.1029/2005JD006717.
- Pérez, C., P. Jimènez, O. Jorba, J. M. Baldasano, E. Cuevas, S. Nickovic, and X. Querol (2007), Long-term simulations (1958–2006) of Saharan dust over the Mediterranean and the Eastern North Atlantic with the DREAM regional dust model, in *IUGG 2007 Perugia, Session: MS004 Mineral Dust Cycle and its Impact on Clouds and Radiation (ICCP) Perugia (Italia), 2–13 July*.
- Pitter, R., and H. Pruppacher (1973), A wind tunnel investigation of freezing of small water drops falling at terminal velocity in air, *Quarterly Journal of the Royal Meteorological Society*, 99, 540–550.
- Plass, G. N., and G. W. Kattawar (1971), Reflection of light pulses from clouds, *Applied Optics*, 10, 2304–2310.
- Platt, C. M. R. (1977), Lidar observation of a mixed-phase altostratus cloud, *Journal of Applied Meteorology*, 16, 339–345.
- Platt, C. M. R., N. L. Abshire, and G. T. McNice (1978), Some microphysical properties of an ice cloud from lidar observation of horizontally oriented crystals, *Journal of Applied Meteorology*, 17, 1220–1224.
-

- Pratt, K. A., P. J. DeMott, J. R. French, Z. Wang, D. L. Westphal, A. J. Heymsfield, C. H. Twohy, A. J. Prenni, and K. A. Prather (2009), In situ detection of biological particles in cloud ice-crystals, *Nature Geoscience*, *2*, 398–401.
- Pruppacher, H. R. (1995), A new look at homogeneous ice nucleation in supercooled water drops, *Journal of the Atmospheric Sciences*, *52*, 1924–1933.
- Pruppacher, H. R., and J. D. Klett (1997), *Microphysics of Clouds and Precipitation*, 954 pp., Springer.
- Quaas, J., O. Boucher, and F. Bréon (2004), Aerosol indirect effects in POLDER satellite data and the Laboratoire de Météorologie Dynamique-Zoom (LMDZ) general circulation model, *Journal of Geophysical Research*, *109*, D08205, doi:10.1029/2003JD004317.
- Radke, L. F., J. A. Coakley, and M. D. King (1989), Direct and remote sensing observations of the effects of ships on clouds, *Science*, *246*, 1146–1149.
- Ramanathan, V., and G. Carmichael (2008), Global and regional climate changes due to black carbon, *Nature Geoscience*, *1*, 221–227.
- Rauber, R. M., and A. Tokay (1991), An explanation for the existence of supercooled water at the top of cold clouds, *Journal of the Atmospheric Sciences*, *48*, 1005–1023.
- Richardson, M. S., P. J. DeMott, S. M. Kreidenweis, D. J. Cziczo, E. J. Dunlea, J. L. Jimenez, D. S. Thomson, L. L. Ashbaugh, R. D. Borys, D. L. Westphal, G. S. Casuccio, and T. L. Lersch (2007), Measurements of heterogeneous ice nuclei in the western United States in springtime and their relation to aerosol characteristics, *Journal of Geophysical Research*, *112*, D02209, doi:10.1029/2006JD007500.
- Roberts, P., and J. Hallett (1968), A laboratory study of the ice nucleating properties of some mineral particulates, *Quarterly Journal of the Royal Meteorological Society*, *94*, 25–34.
- Rosinski, J. (1995), Cloud condensation nuclei as a real source of ice forming nuclei in continental and marine air masses, *Atmospheric Research*, *38*, 351–359.
- Rosinski, J., and G. Morgan (1991), Cloud condensation nuclei as a source of ice-forming nuclei in clouds, *Journal of Aerosol Science*, *22*, 123–133.
- Rutledge, S. A., and P. V. Hobbs (1983), The mesoscale and microscale structure and organization of clouds and precipitation in midlatitude cyclones. VIII: A model for the ‘Seeder–Feeder’ process in warm-frontal rainbands, *Journal of the Atmospheric Sciences*, *40*, 1185–1206.
- Sassen, K. (1980), Remote sensing of planar ice crystals fall attitude, *Journal of the Meteorological Society of Japan*, *58*, 422–429.
-

- Sassen, K. (2002), Indirect climate forcing over the western US from Asian dust storms, *Geophysical Research Letters*, *29*, 1465, doi:10.1029/2001GL014051.
- Sassen, K. (2005a), Meteorology: Dusty ice clouds over Alaska, *Nature*, *434*, p. 456, doi: 10.1038/434456a.
- Sassen, K. (2005b), Polarization in lidar, in *Lidar: Range-Resolved Optical Remote Sensing of the Atmosphere*, edited by C. Weitkamp, pp. 19–42, Springer.
- Sassen, K., and J. M. Comstock (2001), A midlatitude cirrus cloud climatology from the Facility for Atmospheric Remote Sensing. Part III: Radiative properties, *Journal of the Atmospheric Sciences*, *58*, 2113–2127.
- Sassen, K., and R. L. Petrilla (1986), Lidar depolarization from multiple scattering in marine stratus clouds, *Applied Optics*, *25*, 1450–1459.
- Sassen, K., P. J. DeMott, J. M. Prospero, and M. R. Poellot (2003), Saharan dust storms and indirect aerosol effects on clouds: CRYSTAL–FACE results, *Geophysical Research Letters*, *30*, 1633, doi:10.1029/2003GL017371.
- Schaller, R. C., and N. Fukuta (1979), Ice nucleation by aerosol particles: Experimental studies using a wedge-shaped ice thermal diffusion chamber, *Journal of the Atmospheric Sciences*, *36*, 1788–1802.
- Schmidt, J. (2009), Aufbau und Test von Mehrfachstredetektionskanälen zur Messung der Wolkentröpfchengröße mit einem Ramanlidar, Diploma thesis, University of Leipzig. 69 pp.
- Schotland, R. M., K. Sassen, and R. Stone (1971), Observations by lidar of linear depolarization ratios for hydrometeors., *Journal of Applied Meteorology*, *10*, 1011–1017.
- Seifert, P., A. Ansmann, D. Müller, U. Wandinger, D. Althausen, A. J. Heymsfield, S. T. Massie, and C. Schmitt (2007), Cirrus optical properties observed with lidar, radiosonde, and satellite over the tropical indian ocean during the aerosol-polluted northeast and clean maritime southwest monsoon, *Journal of Geophysical Research*, *112*, D17205, doi: 10.1029/2006JD008352.
- Seifert, P., A. Ansmann, I. Mattis, U. Wandinger, M. Tesche, R. Engelmann, D. Müller, C. Pérez, and K. Haustein (2010), Saharan dust and heterogeneous ice formation: Eleven years of cloud observations at a central–European EARLINET site, *Journal of Geophysical Research*, – , in press.
- Stith, J. L., V. Ramanathan, W. A. Cooper, G. C. Roberts, P. J. DeMott, G. Carmichael, C. D. Hatch, B. Adhikary, C. H. Twohy, D. C. Rogers, D. Baumgardner, A. J. Prenni, T. Campos, R. Gao, J. Anderson, and Y. Feng (2009), An overview of aircraft observations from the Pacific Dust Experiment campaign, *Journal of Geophysical Research*, *114*, D05207, doi:10.1029/2008JD010924.
-

- Szyrmer, W., and I. Zawadzki (1997), Biogenic and anthropogenic sources of ice-forming nuclei: A review, *Bulletin of the American Meteorological Society*, *78*, 209–228.
- Tegen, I., and I. Fung (1994), Modeling of mineral dust in the atmosphere: Sources, transport, and optical thickness, *Journal of Geophysical Research*, *99*, 22,897–22,914, doi:10.1029/94JD01928.
- Tegen, I., and A. A. Lacis (1996), Modeling of particle size distribution and its influence on the radiative properties of mineral dust aerosol, *Journal of Geophysical Research*, *101*, 19,237–19,244, doi:10.1029/95JD03610.
- Tegen, I., and K. Schepanski (2009), The global distribution of mineral dust, *IOP Conference Series: Earth and Environmental Science*, *7*, 012001.
- Tesche, M., D. Althausen, D. Müller, and A. Ansmann (2008), Lidar observations of pure and aged saharan dust during the Saharan Mineral Dust Experiments 1 and 2, in *Proceedings of the 24th ILRC, Boulder, CO, USA*.
- Tesche, M., A. Ansmann, D. Müller, D. Althausen, R. Engelmann, V. Freudenthaler, and S. Groß (2009a), Vertically resolved separation of dust and smoke over Cape Verde using multiwavelength Raman and polarization lidars during Saharan Mineral Dust Experiment 2008, *Journal of Geophysical Research*, *114*, D13202, doi:10.1029/2009JD011862.
- Tesche, M., A. Ansmann, D. Müller, D. Althausen, I. Mattis, B. Heese, V. Freudenthaler, M. Wiegner, M. Esselborn, G. Pisani, and P. Knippertz (2009b), Vertical profiling of Saharan dust with Raman lidars and airborne HSRL in southern Morocco during SAMUM, *Tellus Series B*, *61*, 144–164.
- Thomas, L., J. C. Cartwright, and D. P. Wareing (1990), Lidar observations of the horizontal orientation of ice crystals in cirrus clouds, *Tellus Series B*, *42*, 211–216.
- Twomey, S. (2007), Pollution and the planetary albedo, *Atmospheric Environment*, *41* (Supplement 1), 120–125.
- Vali, G. (2008), Repeatability and randomness in heterogeneous freezing nucleation, *Atmospheric Chemistry and Physics*, *8*, 5017–5031.
- Vardiman, L. (1978), The generation of secondary ice particles in clouds by crystal–crystal collision, *Journal of the Atmospheric Sciences*, *35*, 2168–2180.
- Vömel, H., H. Selkirk, L. Miloshevich, J. Valverde-Canossa, J. Valdés, E. Kyrö, R. Kivi, W. Stolz, G. Peng, and J. A. Diaz (2007), Radiation dry bias of the Vaisala RS92 humidity sensor, *Journal of Atmospheric and Oceanic Technology*, *24*, 953–963.
- von Blohn, N., S. K. Mitra, K. Diehl, and S. Borrmann (2005), The ice nucleating ability of pollen: Part III: New laboratory studies in immersion and contact freezing modes including more pollen types, *Atmospheric Research*, *78*, 182–189.
-

- Wandinger, U. (1994), Theoretische und experimentelle Studien zur Messung stratosphärischen Aerosols sowie zum Einfluss der Mehrfachstreuung auf Wolkenmessungen mit einem Polarisations-Raman-Lidar, Ph.D. thesis, University of Hamburg. 125 pp.
- Wandinger, U. (1998), Multiple-scattering influence on extinction- and backscatter-coefficient measurements with Raman and high-spectral-resolution lidars, *Applied Optics*, *37*, 417–427.
- Wandinger, U. (2005), Introduction to lidar, in *Lidar: Range-Resolved Optical Remote Sensing of the Atmosphere*, edited by C. Weitkamp, pp. 1–18, Springer.
- Wandinger, U., I. Mattis, M. Tesche, A. Ansmann, J. Bösenberg, A. Chaikovski, V. Freudenthaler, L. Komguem, H. Linné, V. Matthias, J. Pelon, L. Sauvage, P. Sobolewski, G. Vaughan, and M. Wiegner (2004), Air mass modification over Europe: EARLINET aerosol observations from Wales to Belarus, *Journal of Geophysical Research*, *109*, 24205, doi:10.1029/2004JD005142.
- Welti, A., F. Lüönd, O. Stetzer, and U. Lohmann (2009), Influence of particle size on the ice nucleating ability of mineral dusts, *Atmospheric Chemistry and Physics*, *9*, 6705–6715.
- Westbrook, C. D., A. J. Illingworth, E. J. O'Connor, and R. J. Hogan (2009), Doppler lidar measurements of oriented planar ice crystals falling from supercooled and glaciated layer clouds, *Quarterly Journal of the Royal Meteorological Society*, *136*, 260–276.
- Wiacek, A., and T. Peter (2009), On the availability of uncoated mineral dust ice nuclei in cold cloud regions, *Geophysical Research Letters*, *36*, L17801, doi:10.1029/2009GL039429.
- Winker, D. M., W. H. Hunt, and M. J. McGill (2007), Initial performance assessment of CALIOP, *Geophysical Research Letters*, *34*, L19803, doi:10.1029/2007GL030135.
- Wulfmeyer, V., A. Behrendt, H.-S. Bauer, C. Kottmeier, U. Corsmeier, A. Blyth, G. Craig, U. Schumann, M. Hagen, S. Crewell, P. di Girolamo, C. Flamant, M. Miller, A. Montani, S. Mobbs, E. Richard, M. W. Rotach, M. Arpagaus, H. Russchenberg, P. Schlüssel, M. König, V. Gärtner, R. Steinacker, M. Dorninger, D. D. Turner, T. Weckwerth, A. Hense, and C. Simmer (2008), The convective and orographically induced precipitation study, *Bulletin of the American Meteorological Society*, *89*, 1477–1486.
- Wurzler, S., T. G. Reisin, and Z. Levin (2000), Modification of mineral dust particles by cloud processing and subsequent effects on drop size distributions, *Journal of Geophysical Research*, *105*, 4501–4512, doi:10.1029/1999JD900980.
- Yoshida, J., and S. Asano (2005), Effects of the vertical profiles of cloud droplets and ice particles on the visible and near-infrared radiative properties of mixed-phase stratocumulus clouds, *Journal of the Meteorological Society of Japan*, *83*, 471–480.
-

- 
- Zimmermann, F., S. Weinbruch, L. Schütz, H. Hofmann, M. Ebert, K. Kandler, and A. Worringen (2008), Ice nucleation properties of the most abundant mineral dust phases, *Journal of Geophysical Research*, *113*, D23204, doi:10.1029/2008JD010655.
- Zipser, E. J., C. H. Twohy, S.-C. Tsay, K. L. Thornhill, S. Tanelli, R. Ross, T. N. Krishnamurti, Q. Ji, G. Jenkins, S. Ismail, N. C. Hsu, R. Hood, G. M. Heymsfield, A. Heymsfield, J. Halverson, H. M. Goodman, R. Ferrare, J. P. Dunion, M. Douglas, R. Cifelli, G. Chen, E. V. Browell, and B. Anderson (2009), The Saharan air layer and the fate of African easterly waves — NASA’s AMMA field study of tropical cyclogenesis, *Bulletin of the American Meteorological Society*, *90*, 1137–1156.
- Zobrist, B., C. Marcolli, D. A. Pedernera, and T. Koop (2008), Do atmospheric aerosols form glasses?, *Atmospheric Chemistry and Physics*, *8*, 5221–5244.
-



---

## List of abbreviations

APC	Aerosol particle number concentration
asl	Above sea level
CALIOP	Cloud–Aerosol Lidar with Orthogonal Polarization
CALIPSO	Cloud–Aerosol Lidar and Infrared Pathfinder Satellite Observations
CCN	Cloud condensation nucleus (plural: nuclei)
DREAM	Dust Regional Atmospheric Model
DRIFT	Dust–related Ice Formation in the Troposphere
DWD	<i>Deutscher Wetterdienst</i> (German for ‘German Weather Service’)
ECMWF	European Centre for Medium–range Weather Forecasts
Earlinet	European Aerosol Research Lidar Network
FNL	Final, by means of the archived GDAS data set
FPI	Fabry–Pérot interferometer
GDAS	Global Data Assimilation System
HYSPLIT	Hybrid Single–Particle Lagrangian Integrated Trajectory model
Ift	<i>Leibniz–Institut für Troposphärenforschung</i> (German for ‘Leibniz Institute for Tropospheric Research’)
INSPECT	Ice Nuclei Spectroscopy (Experiment)
IN	Ice nucleus (plural: nuclei)
INC	Ice nuclei concentration
IPCC	International Panel on Climate Change
Laser	Light amplification by stimulated emission of radiation
Lidar	Light detection and ranging
LOS	Line of sight
MARTHA	Multiwavelength Atmospheric Raman lidar for Temperature, Humidity, and Aerosol profiling
NCAR	National Center for Atmospheric Research
NCEP	National Center for Environmental Prediction
ND–YAG	Neodymium–doped yttrium aluminum garnet
Radar	Radio detection and ranging
RFOV	Receiver field of view
SAMUM	Saharan Mineral Dust Experiment
SPVAR	Spatial variance
TSV	Total spatial variance
UTC	Universal Time Coordinated

---



## Acknowledgements

Now, that this work is done, it does not take a noteworthy amount of time to realize that this achievement would have taken considerably longer without the help, the support, and the good nature of a lot of people who surrounded me during the last years.

First and most of all I would like to thank my supervisor Albert Ansmann. He had the initial idea to use the IfT lidar data for a statistical analysis of the ice formation in free-tropospheric clouds. The resulting proposal successfully passed the selection process of the German Science Foundation, and I was given the opportunity to work on this topic. During all the time of this Ph.D. work Alberts ideas, his boundless energy, and his knowledge in diverse fields of research were a source of motivation and of inspiration for me. I also thank him for his support in the preparation of this thesis and of other papers.

I thank the former director of IfT Prof. Jost Heintzenberg for giving me the opportunity to work at this institute with its enjoyable working atmosphere. I also thank him for reviewing this thesis even though he is meanwhile retired.

Ulla Wandinger, Ina Mattis, and Dietrich Althausen were the colleagues around me who took care that I did not lose the focus of my work. Their descriptions and explanations often helped me to understand the one or the other complicated problem. Ulla especially helped me a lot in understanding scattering theory. She also had a careful eye on the writing style and the grammar of my thesis.

I am very grateful to Karsten Haustein and Carlos Pérez from the Barcelona Supercomputing Center. They provided me access to the data of the dust model DREAM. As can be seen in the results section of this thesis, this contribution had a considerable impact on the course of my work.

I had great times in working together with Ronny Engelmann and Matthias Tesche. Ronny is a great physicist, I cannot think of any problem which he would not be able to solve. He introduced me into the basics of IDL GUI programming which finally built the working basis of my Ph.D. thesis. Matthias' extraordinary placidity in virtually every situation and his skills in analyzing and visualizing data not only helped me under several circumstances, it also has always been an inspiration for me. Matthias also put considerable effort in the proof-reading of this thesis, as did the *seaman* of the lidar group, Thomas Kanitz, in the very last turn.

Thanks goes also to all the other colleagues and friends who made my life (even) more enjoyable during the time of my Ph.D. work at IfT — be it during sports, during cozy coffee breaks, or by their assistance during measurements and all-day workflow.

Last but not least I would like to thank my family and especially my girlfriend Rita. All of them proved to be extraordinary patient and kind in all the different situations that came across me during the last years. But they understood it to keep me thrilled by posting little, teasing overtones about the progress of my work into the one or the other conversation.



# Curriculum Vitae

## Patric Seifert

Born on 20 January 1981  
in Riesa, Germany

### Contact:

Leibniz Institute for Tropospheric Research  
Permoserstr. 15  
04318 Leipzig  
Germany  
Phone: +49 341 235-2918  
E-mail: seifert@tropos.de

### Academic Education:

---

- |                   |  |
|-------------------|--|
| Since 02/2006     | Ph.D. thesis at the Leibniz Institute for Tropospheric Research:<br><i>“Dust-related ice formation in the troposphere: A statistical analysis based on 11 years of lidar observations of aerosols and clouds over Leipzig”</i>   |
| 02/2005 – 01/2006 | Diploma thesis at the Leibniz Institute for Tropospheric Research (IfT):<br><i>“Seasonal dependence of geometrical and optical properties of tropical cirrus determined from lidar, radiosonde, and satellite observations over the polluted tropical Indian Ocean (Maldives)”</i> |
| 10/2000 – 01/2006 | Studies of meteorology at the Faculty of Physics and Earth Sciences of the University of Leipzig, Germany  |

### Internships:

---

- |                   |   |
|-------------------|---|
| 06/2005 – 07/2005 | Internship at the National Center for Atmospheric Research (NCAR), Boulder, Co (USA):<br>Working with Dr. Andrew J. Heymsfield and Dr. Steven T. Massie on the project <i>“Investigation of the impact of anthropogenic South Asian aerosol particles on the optical properties of tropical cirrus”</i> |
|-------------------|---|

## Field Campaigns:

---

02/2008	Saharan mineral dust experiment (SAMUM-2), Praia, Cape Verde
06/2008 – 08/2008	Convective and orographically-induced precipitation study (COPS), Black Forest, Germany
09/2005 – 10/2005	International Lindenberg campaign for assessment of humidity and cloud profiling systems and its impact on high-resolution modeling (LAUNCH-2005)

## Publications:

---

- Ansmann, A., M. Tesche, S. Groß, V. Freudenthaler, P. Seifert, A. Hiebsch, J. Schmidt, U. Wandinger, I. Mattis, D. Müller, and M. Wiegner (2010), The 16 April 2010 major volcanic ash plume over central Europe: EARLINET lidar and AERONET photometer observations at Leipzig and Munich, Germany, *Geophysical Research Letters*, L13810, doi:10.1029/2010GL043809.
- Mattis, I., P. Seifert, D. Müller, M. Tesche, A. Hiebsch, T. Kanitz, J. Schmidt, F. Finger, U. Wandinger, and A. Ansmann (2010), Volcanic aerosol layers observed with multiwavelength Raman lidar over central Europe in 2008–2009, *Journal of Geophysical Research*, D00L04, doi:10.1029/2009JD013472.
- Pappalardo, G., U. Wandinger, L. Mona, A. Hiebsch, I. Mattis, A. Amodeo, A. Ansmann, P. Seifert, H. Linné, A. Apituley, L. Alados Arboledas, D. Balis, A. Chaikovskiy, G. D'Amico, F. De Tomasi, V. Freudenthaler, E. Giannakaki, A. Giunta, I. Grigorov, M. Iarlori, F. Madonna, R. Mamouri, L. Nasti, A. Papayannis, A. Pietruczuk, M. Pujadas, V. Rizi, F. Rocadenbosch, F. Russo, F. Schnell, N. Spinelli, X. Wang, and M. Wiegner (2010), EARLINET correlative measurements for CALIPSO: First intercomparison results, *Journal of Geophysical Research*, D00H19, doi:10.1029/2009JD012147.
- Seifert, P., A. Ansmann, I. Mattis, U. Wandinger, M. Tesche, R. Engelmann, D. Müller, C. Pérez, and K. Hausteiner (2010), Saharan dust and heterogeneous ice formation: Eleven years of cloud observations at a central-European EARLINET site, *Journal of Geophysical Research*, – , in press.
- Wandinger, U., M. Tesche, P. Seifert, A. Ansmann, D. Müller, and D. Althausen (2010), Size matters: Influence of multiple scattering on CALIPSO light-extinction profiling in desert dust, *Geophysical Research Letters*, L10801, doi:10.1029/2010GL042815.
- Wehner, B., H. Siebert, A. Ansmann, F. Ditas, P. Seifert, F. Stratmann, A. Wiedensohler, A. Apituley, R. A. Shaw, H. E. Manninen, and M. Kulmala (2010), Observations of turbulence-induced new particle formation in the residual layer, *Atmospheric Chemistry and Physics*, 10, 4319–4330.

- Ansmann, A., M. Tesche, P. Seifert, D. Althausen, R. Engelmann, J. Fruntke, U. Wandinger, I. Mattis, and D. Müller (2009), Evolution of the ice phase in tropical altocumulus: SAMUM lidar observations over Cape Verde, *Journal of Geophysical Research*, *114*, D17208, doi:10.1029/2008JD011659.
- Jumelet, J., S. Bekki, P. Seifert, N. Montoux, J. P. Vernier, and J. Pelon (2009), Microphysical modelling of a mid-latitude “polar stratospheric cloud” event: Comparisons against multiwavelength ground-based and spaceborne lidar data, *Journal of Geophysical Research*, *114*, D00H03, doi:10.1029/2009JD011776.
- Ansmann, A., M. Tesche, D. Althausen, D. Müller, P. Seifert, V. Freudenthaler, B. Heese, M. Wiegner, G. Pisani, P. Knippertz, and O. Dubovik (2008), Influence of Saharan dust on cloud glaciation in southern Morocco during the Saharan Mineral Dust Experiment, *Journal of Geophysical Research*, *113*, D04210, doi:10.1029/2007JD008785.
- Mattis, I., D. Müller, A. Ansmann, U. Wandinger, J. Preißler, P. Seifert, and M. Tesche (2008), Ten years of multiwavelength Raman lidar observations of free-tropospheric aerosol layers over central Europe: Geometrical properties and annual cycle, *Journal of Geophysical Research*, *113*, D20202, doi:10.1029/2007JD009636.
- Massie, S. T., A. Heymsfield, C. Schmitt, D. Müller, and P. Seifert (2007), Aerosol indirect effects as a function of cloud top pressure, *Journal of Geophysical Research*, *112*, D06202, doi:10.1029/2006JD007383.
- Seifert, P., A. Ansmann, D. Müller, U. Wandinger, D. Althausen, A. J. Heymsfield, S. T. Massie, and C. Schmitt (2007), Cirrus optical properties observed with lidar, radiosonde, and satellite over the tropical Indian Ocean during the aerosol-polluted northeast and clean maritime southwest monsoon, *Journal of Geophysical Research*, *112*, D17205, doi:10.1029/2006JD008352.

### Conference Contributions:

---

- Seifert, P., A. Ansmann, I. Mattis, D. Müller, D. Althausen, U. Wandinger, M. Tesche, and C. Pérez (2010), The effect of Saharan dust and the seeder-feeder mechanism on the relationship between temperature and ice formation in clouds observed with lidar, presented at *AMS 13th Conference on Cloud Physics and Atmospheric Radiation, Portland, Oregon, USA, 28 June–2 July*. Poster presentation.
- Seifert, P., S. Groß, A. Ansmann, V. Freudenthaler, A. Hiebsch, J. Schmidt, F. Schnell, M. Tesche, and M. Wiegner (2010), Heterogeneous ice nucleation in the ash plume of Eyjafjöll observed at two central-European EARLINET lidar sites, presented at *AMS 13th Conference on Cloud Physics and Atmospheric Radiation, Portland, Oregon, USA, 28 June–2 July*. Oral presentation.

- Seifert, P., A. Ansmann, I. Mattis, D. Müller, D. Althausen, U. Wandinger, and C. Pérez (2009), Lidar-based profiling of the tropospheric cloud-ice distribution to study the seeder-feeder mechanism and the role of Saharan dust as ice nuclei, presented at *8th International Symposium on Tropospheric Profiling (ISTP 2009)*, Delft, The Netherlands, 19–23 October. Oral presentation.
- Seifert, P., A. Ansmann, I. Mattis, U. Wandinger, and D. Müller (2008), 10 years of lidar observations of mixed phase clouds with focus on temperature and aerosol properties, presented at *15th International Conference on Clouds and Precipitation (ICCP 2008)*, Cancun, Mexico, 7–11 July. Poster presentation.
- Seifert, P., R. Engelmann, A. Ansmann, U. Wandinger, I. Mattis, D. Althausen, and J. Fruntke (2008), Characterization of specular reflections in mixed-phase and ice clouds based on scanning, polarization, and Raman lidar, presented at *24th International Laser Radar Conference (ILRC 2008)*, Boulder, Colorado, USA, 23–28 June. Oral presentation.
- Seifert, P., A. Ansmann, D. Müller, D. Althausen, A. J. Heymsfield, S. T. Massie, and C. Schmitt (2006), Seasonal dependence of geometrical and optical properties of tropical cirrus determined from lidar, radiosonde, and satellite observations over the polluted tropical Indian Ocean (Maldives), presented at *23rd International Laser Radar Conference (ILRC 2006)*, Nara, Japan, 24–28 July. Poster presentation.